

Imaging the microscopic structure of ultracold quantum gases

Peter Würtz

Dem Fachbereich Physik der Technischen Universität Kaiserslautern zur
Erlangung des akademischen Grades „Doktor der Naturwissenschaften“
eingereichte Dissertation

Betreuer:
Prof. Dr. Herwig Ott

Datum des Antrages auf Eröffnung des Promotionsverfahrens:
03.07.2012

Zusammenfassung

Diese Arbeit befasst sich mit der Untersuchung ultrakalter Quantensysteme mithilfe einer neuartigen Nachweis- und Abbildungsmethode. Inspiriert durch die Funktionsweise eines Rasterelektronenmikroskops wird ein fokussierter Elektronenstrahl eingesetzt um eine hochaufgelöste Detektion einzelner Atome zu erreichen.

In den hier vorgestellten Experimenten wurden Dichteverteilungen kalter Gase in sowohl Dipolfallen als auch optischen Gittern mittels Rasterelektronenmikroskopie abgebildet und dadurch die hohe räumliche Auflösung dieses Systems unter Beweis gestellt. Im gleichen Zug war es möglich das gezielte Entfernen von Atomen aus einzelnen Plätzen in optischen Gittern zu demonstrieren.

Die prinzipbedingte Eigenschaft einzelne Atome detektieren zu können ermöglicht den Zugriff auf eine weitere Klasse von Experimenten. Durch Analyse der zeitlichen Abstände von Detektionsereignissen während einer kontinuierlichen Messung ließen sich zeitliche Korrelationen von Teilchen in thermischen Gasen messen. Hierdurch konnte erstmals die zeitliche Korrelationsfunktion zweiter Ordnung direkt am Ort der Atome gemessen werden.

Abstract

This work is concerned with analyzing microscopic structures in ultracold quantum systems by using a novel imaging and detection method. Inspired by the working principles of scanning electron microscopy an imaging scheme has been engineered which involves a tightly focused electron beam for detecting single atoms with high spatial resolution.

In the experiments related to this work the density distributions of ultracold gases have been imaged in optical dipole traps and optical lattices. The small features found in these systems were well reproduced by the imaging system. This demonstrates the high spatial resolution of the scanning electron microscopy method. It has also been shown that the same technique can be used to selectively remove atoms from the single sites of optical lattices.

Furthermore, the single atom sensitivity of the detection scheme allows for a second class of experiments. By analyzing the temporal distribution of detection events taken from a continuous measurement it was possible to observe the bunching effect of bosonic particles. These experiments represent the first *in-situ* measurement of the second order correlation function in temporal dependence for thermal gases.

Contents

Contents	4
1 Introduction	7
Publications	10
2 Theory of Ultracold Bosons	11
2.1 Non Interacting Ideal Bose Gas	12
2.2 Scattering Theory	14
2.3 Weakly Interacting Bose Gas	18
2.4 Numerical Solution	20
2.5 Semi-Ideal Model	22
3 A Scanning Electron Microscope for Ultracold Atoms	25
3.1 Vacuum System	27
3.2 Magneto Optical Traps	27
3.3 Optical Dipole Trap	29
3.4 Optical Lattices	32
3.5 Light-sheet Trap	34
3.6 Electron Microscope	35
4 Imaging Ultracold Quantum Gases	41
4.1 Time of Flight Unfolding	42
4.2 BEC Density Profile	45
4.3 Imaging Optical Lattices	49
4.4 Addressing of Optical Lattices	57
5 Theory of Coherence and Correlation	61

5.1	First Order Correlations	62
5.2	Second Order Correlations	64
5.3	Second Quantization	65
5.4	Thermal First Order Correlation Function	67
5.5	Higher Order Correlation Functions	69
5.6	Spatial Average of Correlations	71
5.7	Statistical Interpretation of a Measurement Process	74
5.8	Influence of Measurement Noise	77
5.9	Influence of Detection Efficiency	78
6	Temporal Correlations in Cold Bose Gases	81
6.1	Measurement Setup	81
6.2	Evaluation of Temporal Correlations	84
6.3	Density Correlation of Time Differences	86
6.4	Thermal Bunching of Bosons	88
6.5	Third Order Correlations	91
6.6	Uncorrelated Control Measurement	93
6.7	Noise Contribution from Total Atom Number Fluctuations	95
6.8	Counting Artifacts	98
6.9	Noise Contribution in $g^{(2)}(0)$	102
6.10	Density Correlations in a BEC	104
7	Conclusion and Outlook	109
A	Supplementary Information	111
A.1	Poisson and Binomial Deletion	111
A.2	Generalized Wick Theorem	112
A.3	Lattice Site Width Simulations	113
A.4	Electron Column	114
A.5	Spatial Average Integrands	115
	List of Figures	117
	List of Tables	118
	Bibliography	119
	Curriculum Vitae	129

Introduction

Technological progress has always paved the way for novel developments in science. Often the advent of more sophisticated measurement techniques enabled the research of new and fascinating phenomena. Especially the exploration of microscopic structures greatly benefits from the ever growing capabilities in imaging objects of interest. When reaching a small-scale regime, where the behavior of matter is dominated by counter-intuitive effects like the particle-wave dualism [1] or the tunneling through classically impenetrable barriers [2], we rely on the theory of quantum mechanics for a description of our observations.

With the advance of methods for cooling and trapping neutral atoms, the possibilities for the preparation of such quantum systems and the study of the very basic principles of physics grew. This ultimately lead to the experimental realization of Bose-Einstein condensation [3-7], which was theoretically described by Einstein and Bose [8, 9] in 1924. These ultracold atomic gases provide a versatile experimental platform to address fundamental quantum mechanical phenomena. Besides being a subject of research on their own [10-12], ultracold atoms are seen as a resource for applications in quantum optics [13], quantum simulation [14], or quantum information processing [15, 16].

Another field of interest is the observation of particle correlations within the atomic samples. Correlation measurements provide a powerful method for deriving fundamental characteristics of an atomic system merely from the statistical analysis of noise fluctuations. In experiments performed within the last decade the thermal bunching effect of Bosons [17] and the anti-bunching nature of Fermions [18] were observed after time of flight.

Also, information about the spatial order of atoms released from optical lattices was obtained by examining density correlations in absorption images [19].

Naturally, the desire for an in-depth understanding of the numerous phenomena encountered within the small structured atomic systems drives the investigation of novel ways for the measurement and imaging of ultracold gases. Inspired by the idea of utilizing scanning electron microscopy, a technique which is unrivaled in its spatial resolution compared to the primarily employed optical methods, an apparatus for probing ultracold atomic gases by means of electron-atom interactions has been designed [20-22]. The potential of the imaging system developed in this context was demonstrated by the first measurement of atomic distributions within sub-micrometer optical lattices. Moreover, it was shown that this technique is not only suited for the imaging, but also for the selective removal of atoms from single lattice sites.

The aim of this thesis is to further explore the capabilities in applying scanning electron microscopy to the field of ultracold quantum gases. In the first part, the analysis of well understood atomic distributions, like Bose-Einstein condensates in harmonic traps and two dimensional optical lattices, plays a key role in the characterization of the system's imaging performance. The procedures developed for optimizing the electron beam parameters are the basis for the density correlation measurements that make up the second part of this work. By using scanning electron microscopy it was first possible to locally measure temporal correlations in thermal Bose gases and to observe the thermal bunching effect within a trapped sample.

Overview

This thesis is organized as follows. Since the experiments in the context of this work are exclusively based on cold Bose gases or Bose-Einstein condensates, Chapter 2 starts with a review of the theoretical background for trapped, interacting Bose gases. After beginning with a description of ideal Bose gases in harmonic traps, the theory is extended by taking scattering effects between the particles into account. Finally, approximations and numerical solutions for determining the density distribution of the atomic systems will be discussed. Chapter 3 provides an overview over the components of the experimental apparatus and the scanning electron microscope that is the basis for all measurements presented in this work.

It covers the implementation of trapping techniques for the preparation of atomic samples and explains the fundamental working principles of scanning electron microscopy for ultracold quantum gases. An in-depth explanation of the image formation processes is subsequently given in Chapter 4. Therein we investigate the performance and optimization of the scanning electron microscope based on the analysis of imaged density distributions. The chapter concludes with a demonstration of the achieved spatial resolution by performing dissipative manipulations in optical lattices with single site addressability. The high spatial resolution and single atom sensitivity of the imaging system enable the measurement of particle correlations, for which a theoretical introduction is given in Chapter 5. It discusses the role of correlation and coherence in classical wave mechanics and their quantum mechanical analogy. A statistical interpretation of the correlation measurement process follows. The measurements carried out using scanning electron microscopy are then presented in Chapter 6. It first covers the observation of temporal correlations in thermal Bose gases and proceeds with the analysis of noise influences. The last topic in this thesis is the investigation of thermal bunching effects in a BEC.

Publications in context of this work

- **Observation of local temporal correlations in trapped quantum gases**
V. Guarrera, P. Würtz, A. Ewerbeck, A. Vogler, G. Barontini and H. Ott
Phys. Rev. Lett. 107 (2011)
- **Ultracold atoms as a target: absolute scattering cross-section measurement**
P. Würtz, T. Gericke, A. Vogler and H. Ott
New J. Phys. 12, 065033 (2010)
- **Image formation in scanning electron microscopy of ultracold atoms**
P. Würtz, T. Gericke, A. Vogler, F. Etzold and H. Ott
Appl. Phys. B 98, 641 (2010)
- **Experimental Demonstration of Single-Site Addressability in a Two-Dimensional Optical Lattice**
P. Würtz, T. Langen, T. Gericke, A. Koglbauer and H. Ott
Phys. Rev. Lett. 103 (2009)
- **High Resolution Scanning Electron Microscopy of an Ultracold Quantum Gas**
T. Gericke, P. Würtz, D. Reitz, T. Langen, H. Ott
Nature Physics 4, 949 - 953 (2008)
- **Probing Bose-Einstein Condensates by Electron Impact Ionization**
P. Würtz, T. Gericke, T. Langen, A. Koglbauer, H. Ott
J. Phys.: Conf. Ser. 141 012020 (2008)
- **All-optical formation of a Bose-Einstein condensate for applications in scanning electron microscopy**
T. Gericke, P. Würtz, D. Reitz, C. Utfeld, H. Ott
Appl. Phys. B 89, 447-451 (2007)

Theory of Ultracold Bosons

In a classic world, the Maxwell–Boltzmann statistics is all that is needed for describing the dynamics of atomic gases in thermal equilibrium. In a regime where the quantum mechanical effects are imperceptible, the thermal de Broglie wavelength λ_{dB} which defines a coherence length for massive particles can be neglected. As seen in the definition of λ_{dB} , the thermal wavelength grows if the temperature of the atoms is reduced

$$\lambda_{\text{dB}} = \frac{2\pi\hbar}{\sqrt{2mk_B T}}. \quad (2.1)$$

Here, \hbar is the reduced Planck constant, m is the mass of the atoms and T the temperature of the thermal equilibrium. For small temperatures, when the coherence length approaches the inter-particle distance, the quantum mechanical aspects become more important.

We discriminate between two types of particles, bosons with integer spin, and fermions with half integer spin. The fundamental difference is their behavior in occupying quantum states. Empirically, identical fermions have never been found to occupy the same state, which is also known as the Pauli exclusion principle. Their statistical behavior is given by the Fermi-Dirac distribution [23]. On the other hand, any number of bosons may occupy a single quantum state, which is expressed by the Bose-Einstein statistics [8, 9].

A special case arises for a combination of low temperature and high density, where more than one boson is expected within a volume of λ_{dB}^3

$$\rho \lambda_{\text{dB}}^3 \gtrsim 1. \quad (2.2)$$

A vivid picture is the overlapping of multiple matter wave functions, forming a single coherent wave. This phenomenon is known as Bose-Einstein condensation and was experimentally realized in 1995 [3-5], 70 years after its theoretical postulation [8, 9].

The experiments in the context of this work are exclusively based on cold Bose gases or Bose-Einstein condensates. It is therefore useful to review the theoretical background of trapped, interacting Bose gases [10]. In the following, an introduction to the ideal Bose gas is given. This theory is extended by taking scattering effects between particles into account. Finally, the distribution of atoms as predicted by theory is determined.

2.1 Non Interacting Ideal Bose Gas

In the experimental setup used for all measurements presented in this work, bosonic Rb⁸⁷ atoms are being held in optical dipole traps. The trapping potentials are well approximated as harmonic confinements for which the theory of the ideal Bose gas and its condensation shall be discussed. A harmonic potential may be written in the form

$$V(x, y, z) = \frac{1}{2}m[\omega_x^2 x^2 + \omega_y^2 y^2 + \omega_z^2 z^2], \quad (2.3)$$

where m is the atomic mass and ω_x , ω_y and ω_z are the trap-frequencies in the x , y and z direction. In such a potential a single atom occupies discrete energy levels

$$\epsilon_{n_x, n_y, n_z} = \hbar\omega_x n_x + \hbar\omega_y n_y + \hbar\omega_z n_z, \quad (2.4)$$

introducing the integer quantum numbers n_x , n_y , n_z . The energies in equation (2.4) do not include the energy for the lowest state which merely shifts the levels but does not change the physics of the system in any way.

In an ideal Bose gas in thermal equilibrium without interactions, the atoms independently occupy the single atom states. The average number of bosons found in a specific state \bar{n}_{n_x, n_y, n_z} with its energy ϵ_{n_x, n_y, n_z} is given by the Bose-Einstein distribution

$$\bar{n}_{n_x, n_y, n_z} = \frac{1}{e^{\beta(\epsilon_{n_x, n_y, n_z} - \mu)} - 1} = \frac{1}{\zeta^{-1} e^{\beta\epsilon_{n_x, n_y, n_z}} - 1}, \quad (2.5)$$

introducing the fugacity $\zeta = e^{\beta\mu}$ and the inverse of the thermal energy $\beta = 1/k_B T$ with equilibrium temperature T and Boltzmann constant k_B . The

parameter μ denotes the chemical potential, which is the energy required for adding a new particle to the system without changing its entropy.

As the mean number of particles in a state cannot be negative, μ is restricted to $\mu < \epsilon_{n_x, n_y, n_z}$ and the fugacity is therefore limited to

$$0 < \zeta < 1. \quad (2.6)$$

In the special case where the fugacity ζ approaches zero, e.g. for increasing temperature, the classical Boltzmann distribution $\bar{n} \propto e^{-\beta\epsilon}$ is a good approximation to the Bose-Einstein statistics given in equation (2.5). In the limit of $\zeta \rightarrow 1$, the mean number of particles in the ground state diverges

$$\bar{n}_{0,0,0} = \frac{1}{\zeta^{-1} - 1} = \frac{\zeta}{1 - \zeta}. \quad (2.7)$$

This effect is known as Bose-Einstein condensation, the macroscopic filling of the ground state for temperatures close to zero [8].

For a quantitative description of Bose-Einstein condensation, the total number of atoms N

$$N = \sum_{n_x, n_y, n_z} \frac{1}{\zeta^{-1} e^{\beta\epsilon_{n_x, n_y, n_z}} - 1} \quad (2.8)$$

is split into the contribution from the number of atoms N_0 in the ground state and the number of thermal atoms N_T occupying all higher states

$$N = N_0 + N_T = \frac{\zeta}{1 - \zeta} + \sum_{n_x \neq 0} \sum_{n_y \neq 0} \sum_{n_z \neq 0} \frac{1}{\zeta^{-1} e^{\beta\epsilon_{n_x, n_y, n_z}} - 1}. \quad (2.9)$$

If the number of particles N is large and the geometrically averaged trap frequency $\bar{\omega} = (\omega_x \omega_y \omega_z)^{1/3}$ is small compared to the thermal energy $k_B T \gg \hbar \bar{\omega}$, the sum over all thermal atoms may be approximated by an integral [10]

$$N_T = \int dn_x dn_y dn_z \frac{1}{\zeta^{-1} e^{\beta\epsilon_{n_x, n_y, n_z}} - 1} = g_3(\zeta) \left(\frac{k_B T}{\hbar \bar{\omega}} \right)^3. \quad (2.10)$$

For $\zeta \rightarrow 1$, the Bose function $g_3(\zeta) = \sum_{n=1}^{\infty} \zeta^n / n^3$ converges to a finite number. The implication of this behavior is that the number of thermal atoms is always limited and constant for a fixed temperature of T . Any particle that is added to the system will occupy the ground state, thus leading to an ever increasing number of condensed atoms N_0 .

A critical temperature T_c may be defined at which the number of condensed atoms N_0 starts to exceed the number of thermal atoms as T decreases further. In dependence of the average trap frequency $\bar{\omega}$ and total atom number N , the critical temperature is given by

$$k_B T_c = \hbar \bar{\omega} \left(\frac{N}{g_3(1)} \right)^{1/3}. \quad (2.11)$$

As illustrated by this equation, the task for producing a Bose-Einstein condensate is not only to decrease the temperature of an atomic system. At the same time the number of atoms must be kept high to ensure a critical temperature that can be reached by the cooling process.

2.2 Scattering Theory

The theory so far is only valid for non interacting bosons and fails in describing the physics of typical Bose-Einstein condensates. To this end, a general quantum mechanical scattering theory is derived and applied to the previously described system of cold bosonic atoms, extending it to include interaction effects between the single particles.

Scattering formalism

The scattering theory formalism is based on the Lippmann-Schwinger equation, which is derived from the Schrödinger equation [24]. If the Hamiltonian H is separated into a free Hamiltonian H_0 and a scattering potential V

$$H = H_0 + V, \quad (2.12)$$

the Lippmann-Schwinger equation is defined as follows

$$|\psi^{(\pm)}\rangle = |\phi\rangle + \frac{1}{E - H_0 \pm i\epsilon} V |\psi^{(\pm)}\rangle. \quad (2.13)$$

In absence of the scattering potential V , the free-particle Schrödinger equation is solved by $|\phi\rangle$, which can be a plain- or spherical wave. The eigenvalue of the solution shall be denoted as E . In presence of the scattering potential V , the solution of the Schrödinger equation with the same eigenvalue is given by $|\psi^{(\pm)}\rangle$. The solution $|\psi^{(\pm)}\rangle$ must reduce to $|\phi\rangle$ as V vanishes. The Lippmann-Schwinger equation is an integral equation for the unknown function $|\psi^{(\pm)}\rangle$, as seen in the position basis

$$\psi^{(\pm)}(\mathbf{x}) = \langle \mathbf{x} | \psi^{(\pm)} \rangle = \phi(\mathbf{x}) + \int d^3x' \langle \mathbf{x} | \frac{1}{E - H_0 \pm i\epsilon} | \mathbf{x}' \rangle \langle \mathbf{x}' | V | \psi^{(\pm)} \rangle. \quad (2.14)$$

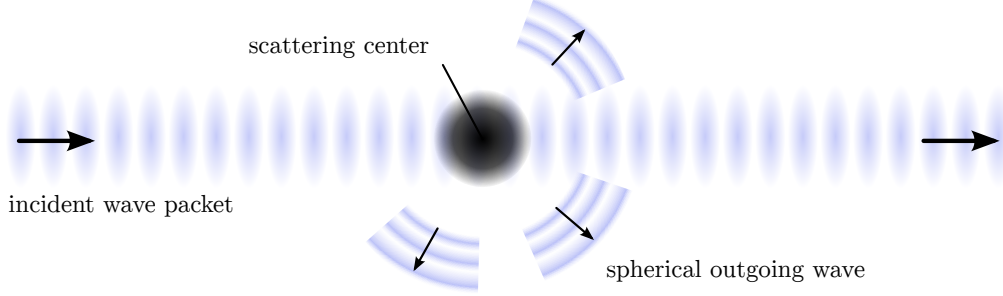


Figure 2.1: Illustration of the plane wave scattering mechanism. The incident plane wave continues moving in the original direction while the scattering potential causes a spherical outgoing wave front, scaled by a form factor.

Observation is always made by a detector placed very far away from the scatterer, greatly larger than the range of the potential, in which case it is safe to assume¹ that $|\mathbf{x}| \gg |\mathbf{x}'|$. Under these circumstances, equation 2.14 can be written as

$$\langle \mathbf{x} | \psi^{(+)} \rangle = \frac{1}{(2\pi)^{3/2}} \left[e^{i\mathbf{k} \cdot \mathbf{x}} + \frac{e^{ikr}}{r} f(\mathbf{k}', \mathbf{k}) \right]. \quad (2.15)$$

In this form, the solution $\psi^{(+)}$ consists of the incident plane wave in propagation direction \mathbf{k} and an outgoing spherical wave with amplitude

$$f(\mathbf{k}', \mathbf{k}) = -\frac{1}{4\pi} (2\pi)^3 \frac{2m}{\hbar^2} \langle \mathbf{k}' | V | \psi^{(+)} \rangle, \quad (2.16)$$

as illustrated in figure 2.1.

An important quantity that characterizes a scattering process is the differential cross section $\frac{d\sigma}{d\Omega}$. The cross section is defined as the number of particles scattered into a differential solid-angle element $d\Omega$ per unit time, normalized by the number of incident particles. This rate is given by the particle flux densities $\mathbf{j}_{\text{scatt}}$ and $\mathbf{j}_{\text{incid}}$ obtained from equation (2.15) [25]. The first term of the equation represents a large number of identically prepared particles which can be approximated as plane wave. With the second term defining the flux of scattered particles $\mathbf{j}_{\text{scatt}}$, the total cross section can be written as

$$\frac{d\sigma}{d\Omega} = \frac{r^2 |\mathbf{j}_{\text{scatt}}| d\Omega}{|\mathbf{j}_{\text{incid}}|} = |f(\mathbf{k}', \mathbf{k})|^2 d\Omega, \quad (2.17)$$

¹This approximation is not valid for a coulomb potential due to long range effects. However, for a shielded effective potential, the approximation is appropriate [25].

with a differential cross section of

$$\frac{d\sigma}{d\Omega} = |f(\mathbf{k}', \mathbf{k})|^2. \quad (2.18)$$

As the function $|\psi^{(+)}\rangle$ is still unknown, a solution of the differential cross section is not yet possible. If the effect of the scatterer is not very strong, the function $|\psi^{(+)}\rangle$ in equation (2.15) can be replaced by the incident plane wave $|\phi\rangle$. This approximate expression of $f(\mathbf{k}', \mathbf{k})$ is also known as first-order Born amplitude, which then reads

$$f^{(1)}(\mathbf{k}', \mathbf{k}) = -\frac{1}{4\pi} \frac{2m}{\hbar^2} \int d^3x' e^{i(\mathbf{k}-\mathbf{k}')\cdot\mathbf{x}'} V(\mathbf{x}'). \quad (2.19)$$

The first-order amplitude is the three-dimensional Fourier transform of the potential V with respect to $\mathbf{q} \equiv \mathbf{k} - \mathbf{k}'$, commonly named as form factor.

Partial wave expansion

For being able to determine the scattering amplitudes in equation (2.16) the first-order Born approximation was applied, replacing the unknown function $|\psi^+\rangle$ by a plane wave $|\mathbf{k}\rangle$. If the scattering potential V is known to be radially symmetric, it is reasonable to use a function $|\tilde{\psi}_k\rangle$ composed of a series of radial waves for a scalar momentum k instead [26]

$$\tilde{\psi}_k(\mathbf{r}) = \sum_{\ell=0}^{\infty} c_{2\ell} R_{k,2\ell}(r) P_{2\ell}(\cos(\theta)), \quad (2.20)$$

with coefficients c_ℓ and the Legendre polynomials $P_\ell(x)$ of degree ℓ . Only even values of ℓ contribute to the sum as the wave function must be symmetric for bosons. The radial functions $R_{k,\ell}(r)$ are solutions to the radial Schrödinger equation

$$\left(\frac{1}{r} \frac{d^2}{dr^2} r - \frac{\ell(\ell+1)}{r^2} + k^2 - \frac{2MV(r)}{\hbar^2} \right) R_{k,\ell}(r) = 0, \quad (2.21)$$

with a reduced mass of $M = \frac{m_1 m_2}{m_1 + m_2} = m/2$ for identical particles. If the scattering potential $V(r)$ drops faster than $\frac{1}{r}$ for $r \rightarrow \infty$, the radial functions can be approximated as

$$R_{k,\ell}(r) = \frac{1}{kr} \sin \left(kr - \frac{\ell\pi}{2} + \delta_{k\ell} \right), \quad (2.22)$$

where $\delta_{k\ell}$ are the scattering phases.

From equation (2.21) it becomes evident that an additional centrifugal potential $\frac{\ell(\ell+1)}{r^2}$ arises for scattering processes with angular momentum $\ell \neq 0$. This effectively limits the number of partial waves with high angular momentum ℓ that contribute to the scattering process for a given incident kinetic energy of $\frac{\hbar^2 k^2}{2m}$. For Bosons an additional limitation is the symmetry condition of the wave function which forbids processes with odd angular momentum numbers ℓ . If the kinetic energy is too low, the contributions from partial waves with $\ell \geq 2$ become negligible and thus all but the partial s-wave with $\ell = 0$ can be discarded. In such cases the incident particle cannot overcome the centrifugal barrier at all. This condition is well met in typical cold atom experiments with bosonic particles at temperatures of $T = 100 \mu\text{K}$ or below [27].

S-Wave scattering

In the s-wave regime, all angular dependencies of incident and scattered particles vanish and the scattering amplitude $f(\mathbf{k}', \mathbf{k})$ given by equation (2.16) only depends on the scalar momentum k . For very low kinetic energies, the scattering process is then completely characterized by the amplitude

$$a_s = -\lim_{k \rightarrow 0} f(k) = -\lim_{k \rightarrow 0} \frac{\exp(i\delta_{k0}) \sin(\delta_{k0})}{k}, \quad (2.23)$$

where a_s is called the s-wave scattering length. This parameter is negative for attractive interactions and positive for repulsive interactions. A repulsive s-wave interaction can be interpreted as scattering of hard spheres with a radius of a_s . For the Rb^{87} atoms used in the experiments discussed in this work the s-wave scattering length is $99 a_0$, with a_0 being the Bohr radius.

It is appropriate to approximate such a system by a Fermi-contact potential

$$V(r) = g \delta(r), \quad (2.24)$$

where g is the coupling constant of the interaction given by

$$g = \frac{4\pi\hbar^2}{m} a_s. \quad (2.25)$$

2.3 Weakly Interacting Bose Gas

The potential derived from the scattering formalism allows to include interaction effects in the description of Bose gases. The Hamiltonian of such an interacting gas in an external potential $V(\mathbf{r})$ then depends on an additional two-particle potential $U(\mathbf{r} - \mathbf{r}')$. In second quantization this Hamiltonian reads [28]

$$\hat{H} = \int d\mathbf{r} \hat{\psi}^\dagger(\mathbf{r}) \left[-\frac{\hbar^2}{2m} \nabla^2 + V(\mathbf{r}) \right] \hat{\psi}(\mathbf{r}) \quad (2.26)$$

$$+ \frac{1}{2} \int d\mathbf{r} d\mathbf{r}' \hat{\psi}^\dagger(\mathbf{r}) \hat{\psi}(\mathbf{r}') U(\mathbf{r} - \mathbf{r}') \hat{\psi}(\mathbf{r}) \hat{\psi}^\dagger(\mathbf{r}'). \quad (2.27)$$

The operators $\hat{\psi}^\dagger(\mathbf{r})$ and $\hat{\psi}(\mathbf{r})$ are the Boson creation and annihilation operators at position \mathbf{r} . The integral over the two-particle scattering potential expresses the interactions. As derived in the previous section, the scattering potential for ultracold atoms may be approximated in the s-wave regime by a Fermi-contact potential

$$U(\mathbf{r} - \mathbf{r}') = g \delta^3(\mathbf{r} - \mathbf{r}'), \quad (2.28)$$

with the coupling constant g as defined in equation (2.25). When the interaction potential $U(\mathbf{r} - \mathbf{r}')$ is replaced by the contact potential, the time dependent Schrödinger equation derived from equation (2.27) reads

$$i\hbar \frac{\partial}{\partial t} \Psi(\mathbf{r}, t) = \left[-\frac{\hbar^2 \nabla^2}{2m} + V(\mathbf{r}) + g |\Psi(\mathbf{r}, t)|^2 \right] \Psi(\mathbf{r}, t). \quad (2.29)$$

It was first derived by E. P. Gross [29] and L. P. Pitaevskii [30] and is therefore known as the Gross-Pitaevskii equation. The operators $\hat{\psi}(\mathbf{r})$ were replaced by the time dependent complex fields $\Psi(\mathbf{r}, t)$, neglecting the effects being addressed by the Bogoliubov theory of elementary excitations. This is a valid simplification for sufficiently low temperatures.

If the wave function is expressed as a real part $\phi(\mathbf{r})$ and a complex phase

$$\Psi(\mathbf{r}, t) = \phi(\mathbf{r}) e^{-i\frac{\mu}{\hbar}t}, \quad (2.30)$$

the temporal and spatial dependencies can be separated. This is commonly interpreted as a distribution of atoms in the ground state, which oscillates like a coherent single wave. After the separation, the stationary Gross-Pitaevskii equation for $\phi(\mathbf{r})$ is found

$$\left[-\frac{\hbar^2}{2m} \nabla^2 + V(\mathbf{r}) + g |\phi(\mathbf{r})|^2 \right] \phi(\mathbf{r}) = \mu \phi(\mathbf{r}), \quad (2.31)$$

with an energy eigenvalue of μ , the chemical potential. The Gross-Pitaevskii equation is a non-linear Schrödinger equation due to the interaction term.

Thomas-Fermi approximation

The Gross-Pitaevskii equation given in (2.31) is a partial, non-linear second order differential equation. As it cannot be solved analytically it is common to use the Thomas-Fermi (TF) approximation in order to derive the ground state wave function.

When comparing the kinetic energy and the interaction term in equation (2.31), the interaction energy greatly exceeds the kinetic energy for high densities $|\phi(\mathbf{r})|^2$ and low curvature of the wave function

$$\left| \frac{\hbar^2}{2m} \nabla^2 \phi(\mathbf{r}) \right| \ll g |\phi(\mathbf{r})|^2. \quad (2.32)$$

This is especially true for the center of the trap, but the assumption does not hold for the edges of the atomic distribution where the densities are low. If the kinetic energy term is neglected, the Gross-Pitaevskii equation is simplified to

$$\left[V(\mathbf{r}) + g |\phi_{\text{TF}}(\mathbf{r})|^2 \right] \phi_{\text{TF}}(\mathbf{r}) = \mu_{\text{TF}} \phi_{\text{TF}}(\mathbf{r}), \quad (2.33)$$

and the atomic density is directly given by

$$n_{\text{TF}}(\mathbf{r}) = |\phi_{\text{TF}}(\mathbf{r})|^2 = \frac{1}{g} \max \left(\mu_{\text{TF}} - V(\mathbf{r}), 0 \right). \quad (2.34)$$

Since the integral over the density $n_{\text{TF}}(\mathbf{r})$ yields the number of atoms N , a normalization condition is found for the chemical potential in TF approximation

$$\mu_{\text{TF}} = \frac{\hbar \bar{\omega}}{2} \left(\frac{15 N a_s}{\bar{a}} \right)^{2/5}, \quad (2.35)$$

where $\bar{\omega}$ is the average trap frequency and $\bar{a} = \sqrt{\hbar/m\bar{\omega}}$ the average oscillator length of the harmonic potential.

The shape of $n_{\text{TF}}(\mathbf{r})$ exactly follows the trapping potential, thus being an inverted parabola which ends at $V(\mathbf{r}) = \mu_{\text{TF}}$. This equation defines the Thomas-Fermi radii R_i for each axis

$$\frac{1}{2} m \omega_i^2 R_i^2 = \mu_{\text{TF}}, \quad \text{with} \quad R_i = \bar{a} \frac{\bar{\omega}}{\omega_i} \left(\frac{15 N a_s}{\bar{a}} \right)^{1/5}. \quad (2.36)$$

The density distribution can be simply expressed by the Thomas-Fermi radii, so it reads

$$n_{\text{TF}}(\mathbf{r}) = \frac{\mu_{\text{TF}}}{g} \max \left(1 - \frac{x^2}{R_x^2} - \frac{y^2}{R_y^2} - \frac{z^2}{R_z^2}, 0 \right). \quad (2.37)$$

2.4 Numerical Solution

In many situations, the analytical solution of the Gross-Pitaevskii equation after applying the Thomas-Fermi approximation is sufficient. For high atom numbers, the result reliably models the density distributions as obtained from absorption images of pure Bose-Einstein condensates.

However, when utilizing high spatial resolution methods for measuring the distribution, the desire to model the structure in low-density regions, specifically the edge of a condensate, arises. A more precise, numerical method is required, as there is no known analytical solution to the Gross-Pitaevskii equation. The imaginary time propagation scheme has proven to be a robust tool for finding ground state wave functions of quantum mechanical systems [31].

Starting from the stationary Schrödinger equation $\hat{H}\Psi(\mathbf{r}) = E\Psi(\mathbf{r})$, we decompose the wave function $\Psi(\mathbf{r})$ into a series of eigenstates $\phi_i(\mathbf{r})$, coefficients c_i and eigenvalues E_i

$$\hat{H}\Psi(\mathbf{r}) = \sum_{i=0}^{\infty} c_i \hat{H}\phi_i(\mathbf{r}) = \sum_{i=0}^{\infty} E_i c_i \phi_i(\mathbf{r}). \quad (2.38)$$

We further introduce the time evolution operator $\hat{U}(t) = e^{-i\hat{H}t/\hbar}$, which we can use to propagate an arbitrary initial field $\Psi(\mathbf{r}, t=0)$ in time

$$\Psi(\mathbf{r}, t) = \hat{U}(t)\Psi(\mathbf{r}, 0) = e^{-i\hat{H}t/\hbar} \Psi(\mathbf{r}, 0) \quad (2.39)$$

$$= \sum_{i=0}^{\infty} e^{-iE_i t/\hbar} c_i \phi_i(\mathbf{r}). \quad (2.40)$$

The result is a superposition of states oscillating with energies E_i . The time t is now mapped to imaginary time $t \rightarrow -i\tau$, and the time evolved state becomes

$$\Psi(\mathbf{r}, \tau) = \sum_{i=0}^{\infty} e^{-E_i \tau/\hbar} c_i \phi_i(\mathbf{r}). \quad (2.41)$$

This way, the previously oscillating states are now in a decay, with decreasing decay time for higher energies. Formally, the ground state is preserved when shifting all energy levels by the yet unknown ground state energy E_0 . Thus, for sufficiently large times τ any initial guess will converge to the ground state ϕ_0 , as all higher states will vanish in time

$$\tilde{\Psi}(\mathbf{r}, \tau) = \sum_{i=0}^{\infty} e^{(E_0 - E_i)\tau/\hbar} c_i \phi_i(\mathbf{r}) \underset{\tau \rightarrow \infty}{=} c_0 \phi_0(\mathbf{r}). \quad (2.42)$$

As seen in equation (2.42), all we need to do is to find an initial guess, preferably close to the solution, and evolve that state in time. To this end, time is split into small steps $\tau = n \cdot \Delta\tau$, allowing $\hat{U}(\Delta\tau)$ to be approximated for small $\Delta\tau$. In the most simplest form orders of τ^2 are neglected

$$\Psi(\mathbf{r}, \Delta\tau) = \left(1 - \frac{\Delta\tau}{\hbar} \hat{H}\right) \Psi(\mathbf{r}, 0) + \mathcal{O}(\Delta\tau^2), \quad (2.43)$$

and the equation can be repeatedly applied to the initial guess until it converges to the ground state. Since the ground state energy is yet unknown, the ground state will not be inherently stable as suggested in equation (2.42). Instead, the wave function must be re-normalized after each step in order to preserve it.

In more sophisticated approximations for the single time steps, like the Crank-Nicolson split-step propagation method, higher orders of $\Delta\tau$ are taken into account. Also, an implementation of this algorithm may be optimized for specific trap symmetries [32, 33] which reduces the computational effort and allows for faster convergence of the iterative procedure.

When comparing the imaginary time propagation solution with the Thomas Fermi profile, the limitation of the TF approximation becomes evident. Figure 2.2 shows the numerical solution of the Gross-Pitaevskii equation for a cylindrical trapping potential. The axial and radial trapping frequencies are $\omega_a = 2\pi \times 12$ Hz and $\omega_r = 2\pi \times 170$ Hz, matching the parameters of the experimental setup. In this simulation, the condensate contains a number of 80,000 atoms. As seen in the radial and axial slices of the density distribution, the TF approximation matches the exact solution at the center of the trap, but does not describe the low density regions of the condensate correctly. Also, the chemical potential μ is found to be 10% lower than the estimation μ_{TF} .

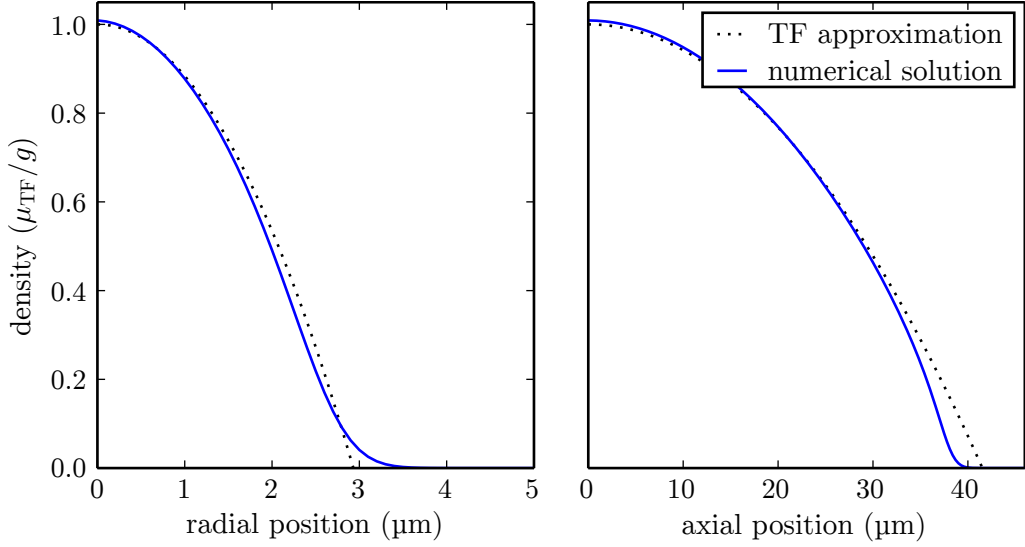


Figure 2.2: Numerical solution of the Gross-Pitaevskii equation in comparison with the Thomas Fermi approximation for a cylindrical trapping potential. The simulated condensate contains 80,000 atoms and slices in radial and axial direction of its extent are shown. As expected, the TF approximation matches the exact solution at the center of the condensate, but does not describe the regions of low density correctly.

2.5 Semi-Ideal Model

The numerical solution of the Gross-Pitaevskii equation took us one step closer to a more accurate description of the density distributions measured in high resolution images. However, the Gross-Pitaevskii equation is only valid for an ideally prepared system with zero temperature. In real world experiments the atomic gases are cooled down to finite temperatures where a fraction of atoms still resides in a thermal state.

The result from the numerical Gross-Pitaevskii solution can be refined by adding a fraction of non-interacting thermal atoms whose distribution is given by the semi-ideal Bose gas model [34]. In the semi-ideal model the thermal atoms are treated as an ideal Bose gas that is confined by an effective potential $V_{\text{eff}}(\mathbf{r})$, while initially the condensate wave function $\Psi(\mathbf{r})$ remains unaffected. The effective potential combines the external potential $V(\mathbf{r})$ and a repulsion by the condensate

$$V_{\text{eff}}(\mathbf{r}) = V(\mathbf{r}) + 2g |\Psi(\mathbf{r})|^2. \quad (2.44)$$

It accounts for exchange collisions between atoms in different quantum

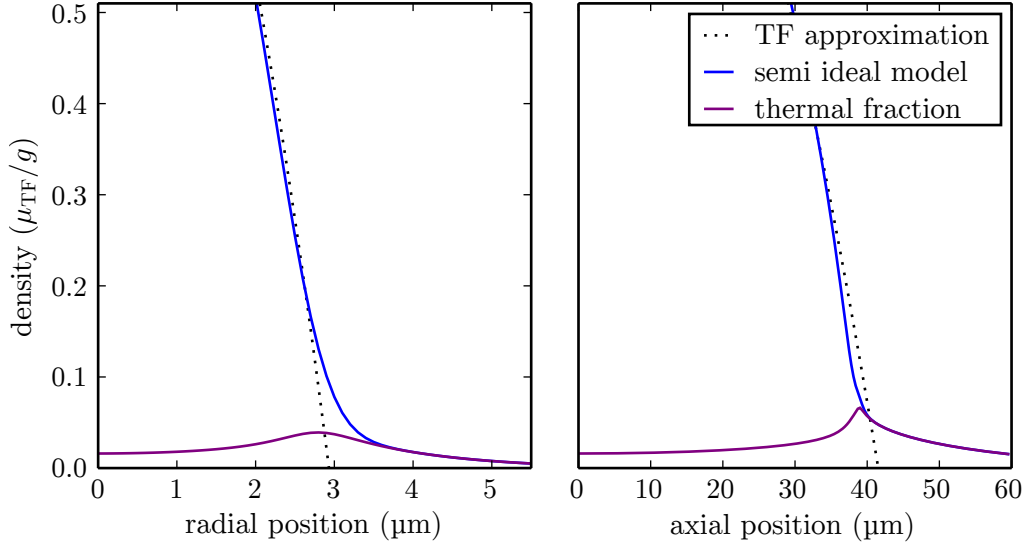


Figure 2.3: Wings of a semi-ideal Bose gas in a cylindrical trap. The parameters for the simulation are the same as in Figure 2.2. As seen in the radial and axial slices of the distribution, the separately shown thermal fraction with $T = 80 \text{ nK}$ is repelled by the large condensate fraction in the center. The Thomas Fermi approximation is shown again for comparison.

states [35]. The density distribution for the thermal fraction is then given by

$$n_{\text{th}}(\mathbf{r}) = \frac{g_{3/2}(z(\mathbf{r}))}{\lambda_{\text{th}}^3}, \quad (2.45)$$

with the modified fugacity

$$z(\mathbf{r}) = \exp\left(-\frac{V_{\text{eff}}(\mathbf{r}) - \mu}{k_B T}\right), \quad (2.46)$$

the thermal de Broglie wavelength $\lambda_{\text{th}} = \sqrt{2\pi\hbar^2/mk_B T}$, and the Einstein function $g_{3/2}(z)$. Thus, the full bimodal density distribution becomes

$$n(\mathbf{r}) = |\Psi(\mathbf{r})|^2 + n_{\text{th}}(\mathbf{r}). \quad (2.47)$$

This model is not yet self-consistent as the repulsion has only been treated one way. For a consistent description the condensate wave function must be re-evaluated using again an effective potential, modified by the repulsion between both atom fractions. This is an iterative process, continued until the density distributions converge to a stationary, self-consistent

model. We will pass on the search for a self-consistent solution, as it is expected to be a minor but very costly improvement.

In Figure 2.3, a semi-ideal Bose gas model based on the numerical solution of the Gross-Pitaevskii equation is shown for the same experimental parameters as used in the simulation of a BEC at zero temperature. It depicts the wings of the atom distribution in radial and axial direction. The effect of the thermal fraction being repelled by the large condensate fraction in the center of the trap is clearly visible. The calculation was done for a temperature of $T = 80$ nK, which adds a number of 25,000 thermal atoms to the system with 80,000 atoms in the BEC.

A Scanning Electron Microscope for Ultracold Atoms

The most distinguishing feature of the electron microscope for ultracold quantum gases is the detection of individual atoms with high spatial resolution. Combining electron microscopy with an apparatus for making and probing cold atomic gases requires for an unique design that meets several demands. For cooling atoms down to critical temperatures where quantum degeneracy is reached, an ultra-high vacuum system along with optical cooling and magnetic trapping methods is required. The system must be able to hold the atoms long enough to perform any desired experiment. Ideally, the experimental setup should provide as much flexibility as possible when preparing the atomic samples. Parameters like the desired number atoms and their temperature as well as the trapping geometry may be subject of change. Various laser systems are employed to tackle the different demands for specific situations. Also, key characteristics of the electron scanning microscope like the beam current and diameter must be adjustable for a given measurement scenario. The electron column itself is therefore specifically tailored to this environment and unique in its adaptability.

An overview over the components of the apparatus involved in typical experiments is shown in Figure 3.1. The general experimental sequence begins with collecting and cooling ^{87}Rb atoms using magneto optical traps (MOT). Critically low temperatures are reached after transferring the atoms to an optical CO_2 dipole trap for evaporative cooling. At this point, the atomic cloud can be shaped by applying additional optical confinements. After the completion of the preparations the sample is first

3. A SCANNING ELECTRON MICROSCOPE FOR ULTRACOLD ATOMS

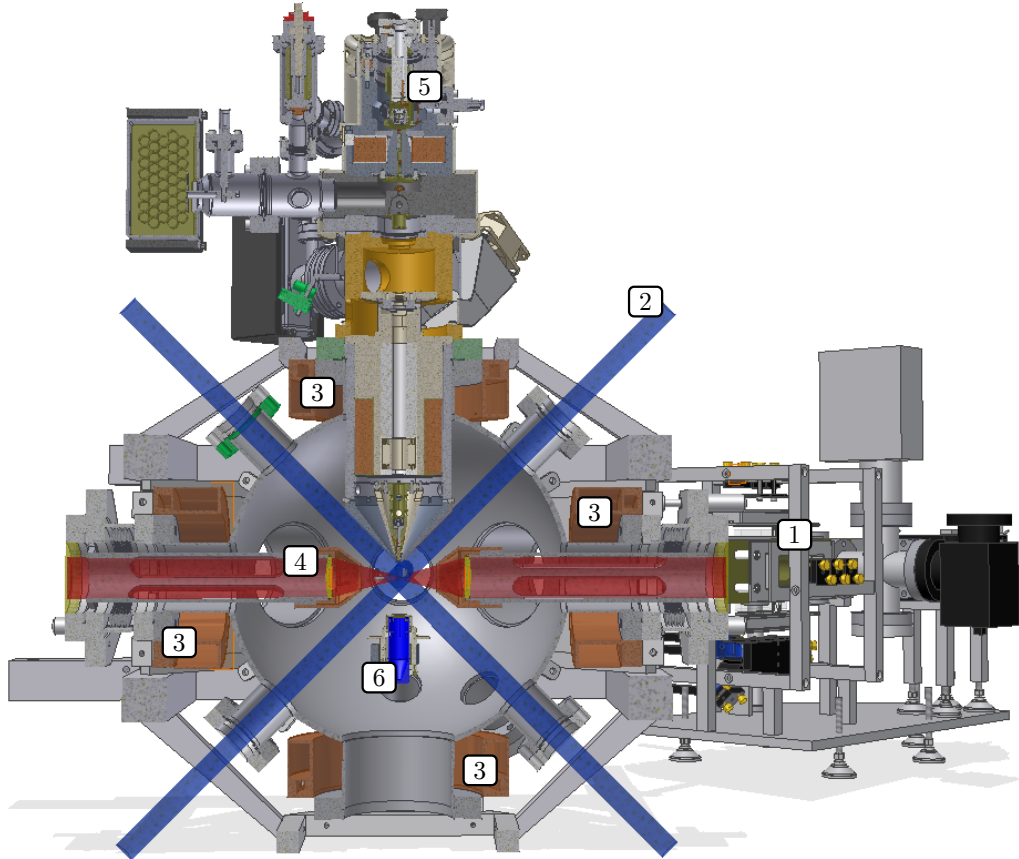


Figure 3.1: Experimental realization of the scanning electron microscope for ultracold atoms. The 2D-MOT formed within the small chamber on the right (1) serves as an atom source for the 3D-MOT in the main experimental chamber. The 3D-MOT is created by six counter propagating cooling beams (2) and magnetic coils (3) for confinement. Evaporative cooling takes place in the CO_2 optical dipole trap depicted by the red beam (4) that is focused at the center of the chamber. The atoms that are held in the focus are directly below the electron column (5) that is mounted on top. A Faraday cup (6) dumps the electron beam that passes almost seamlessly through the atomic cloud.

scanned by the electron microscope and finally released for a supplementary time of flight absorption image before restarting the experimental cycle. In the following, the realization of the scanning electron microscope for cold atoms shall be described briefly. A more detailed description of the apparatus is found in previous works related to this experiment [20,36-38].

3.1 Vacuum System

The cooling of atoms requires an ultra high vacuum environment where the collisions with residual gas molecules are drastically reduced. Loading atoms from the background gas however becomes less efficient as their number per volume decreases. A two chamber vacuum system has been chosen so that the environment of each chamber can be adapted to its purpose. The main vacuum chamber in where all experiments are performed sustains an ultra high vacuum with a pressure of 2×10^{-10} mbar. It integrates and supports the components of the 3D-magneto-optical-trap (3D-MOT), optical dipole traps, optical lattices and the scanning electron microscope. In the smaller chamber, called the 2D-MOT chamber, the atoms are loaded from background gas. It is connected using a flexible bellow and a valve. The bellow allows the two chambers to be aligned in a way so that the atoms from the 2D-MOT can be directly transferred to the 3D-MOT in the main chamber. This junction also acts as a differential pumping section with a maximum capacity of 1×10^{-4} which allows a pressure of 4×10^{-7} mbar in the 2D-MOT chamber while maintaining the ultra high vacuum in the main chamber.

3.2 Magneto Optical Traps

The 2D-MOT chamber acts as an atom source for the system [39]. Its higher partial pressure allows for a reduction of the time required for loading a sufficient number of particles during the experimental preparation. The vacuum chamber for the 2D-MOT [20] is made out of a titanium cuboid with four orthogonal oval bores with a diameter of 25 mm and a length of 81 mm. This provides a cylindrical cooling volume with a large aspect ratio. The windows are glued to the chamber to ensure a compact design. An oven with a ^{87}Rb reservoir is used as atom source. Four rectangular coils generate a two dimensional magnetic quadrupole field. The cooling light drives the $|5S_{1/2}, F = 2\rangle \rightarrow |5P_{3/2}, F = 3\rangle$ transition of ^{87}Rb with a detuning of 16 MHz to the red. The $5S_{1/2} \rightarrow 5P_{3/2}$ transition is

3. A SCANNING ELECTRON MICROSCOPE FOR ULTRACOLD ATOMS

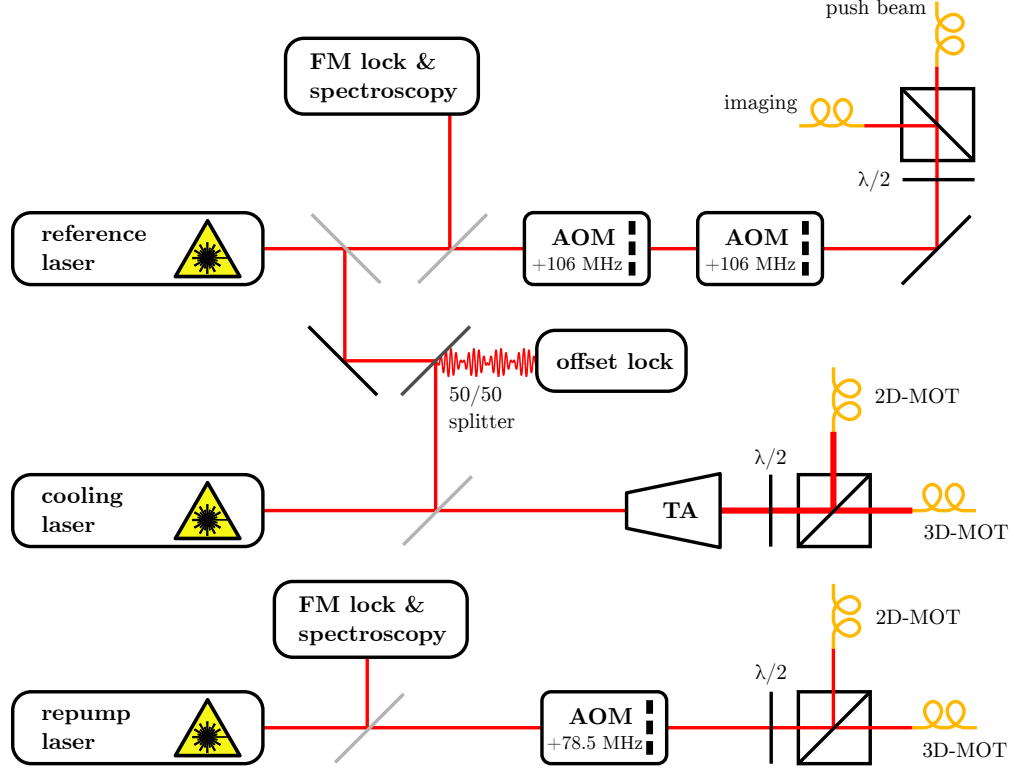


Figure 3.2: Illustration of the laser setup for cooling and imaging ^{87}Rb atoms. The reference laser is locked on a crossover peak below the cooling transition. The light is on resonance after passing two AOMs and can be used for imaging and pushing atoms into the 3D-MOT chamber. The seed laser for the cooling light is offset locked to the reference so that its detuning can be varied during the experimental sequence. A tapered amplifier (TA) then provides for the power that is required for a MOT. The repump laser also passes an AOM for controlling its intensity before being fiber-coupled.

commonly known as the alkali D_2 line [40]. Since off-resonance excitations to the $|5P_{3/2}, F = 2\rangle$ state are possible, a repump-laser is required for returning atoms decaying into $|5S_{1/2}, F = 1\rangle$ to the cooling cycle [41]. The $F = 1 \rightarrow F' = 2$ repumping light of the D_2 line is generated by a grating stabilized diode laser.

A polarizing beam splitter cube combines the cooling and the repumping laser light. The beam is split into three parallel, spherical beams that are guided through the 2D-MOT chamber. Each beam is then individually retro-reflected. To enhance the atom flux to the main chamber a resonant

push beam is superimposed in the longitudinal direction of the quadrupole field. With this configuration a flux of up to 4×10^8 atoms/s at a rubidium partial pressure of about 4×10^{-7} mbar is achieved.

For the 3D-MOT, a standard six beam configuration was chosen [42]. The strong axis of the magnetic quadrupole field lies in the horizontal plane perpendicular to the optical dipole trap. This configuration is favorable with regard to a maximum spatial overlap between the 3D-MOT and the optical dipole trap. Because the lower part of the electron column is made of an iron-nickel alloy with high magnetic susceptibility, any external magnetic quadrupole field is distorted. This problem is circumvented by using three pairs of coils, which are oriented perpendicular to each other around the chamber. The combined field of all six coils creates a spherical magnetic quadrupole field with a volume of about one cubic centimeter. The field minimum is located 13 mm below the tip of electron microscope and the field gradient is 10 G/cm along the strong axis. The laser light for the 3D-MOT is obtained from the same laser system as described before. The intensity of the repumping radiation can be regulated with an acousto-optic modulator (AOM).

3.3 Optical Dipole Trap

The lowest atomic ensemble temperature that can be achieved in a standard MOT is restricted by the Doppler limit. In case of ^{87}Rb , this temperature is 146 μK [40]. In order to reach quantum degeneracy and thus producing Bose-Einstein condensates an evaporative cooling method [43-45] is required. Most methods are based on magnetic traps that could affect the performance of the scanning electron microscope and thus cannot be used in this setup. To this end, an all optical approach for Bose-Einstein condensation was chosen [46-48].

An optical dipole trap is a potential for neutral atoms that originates from the electric dipole moment induced by the oscillating electric field of the light. The dipole moment \mathbf{d} caused by the electric field \mathbf{E} is given by [49]

$$\mathbf{d} = \alpha(\omega)\mathbf{E}, \quad (3.1)$$

with the complex polarizability α that depends on the oscillation frequency ω of the light field. Averaging the energy of the dipole $E_{\text{dip}} = -\mathbf{d} \cdot \mathbf{E}$ in

3. A SCANNING ELECTRON MICROSCOPE FOR ULTRACOLD ATOMS

the electric field over time yields the optical dipole potential

$$V_{\text{dip}}(\mathbf{r}) = -\frac{1}{2\epsilon_0 c} \text{Re}[\alpha(\omega)] I(\mathbf{r}), \quad (3.2)$$

where the strength of the light field can be expressed by the intensity I at position \mathbf{r} . Calculating the polarizability $\alpha(\omega)$ for a two level atom with an optical transition frequency of ω_0 leads to an expression of $V_{\text{dip}}(\mathbf{r})$ that depends on the detuning of the light $\Delta = \omega - \omega_0$ and the decay rate Γ of the excited level [49]

$$V_{\text{dip}}(\mathbf{r}) = \frac{3\pi c^2}{2\omega_0^3} \frac{\Gamma}{\Delta} I(\mathbf{r}). \quad (3.3)$$

Equation (3.3) is a simplified expression that is only valid if the detuning is small compared to the transition frequency, thus fulfilling $|\Delta| \ll \omega_0$. This is commonly known as the rotating wave approximation (RWA) and is applies to most experimental realizations of optical traps. For alkali atoms with the two dominant optical transitions $S_{1/2} \rightarrow P_{3/2}$ and $S_{1/2} \rightarrow P_{1/2}$ the following expression can be derived [49, 50]

$$V_{\text{dip}}(\mathbf{r}) = \frac{\pi c^2 \Gamma}{2\omega_0^3} \left(\frac{2}{\Delta_{3/2}} + \frac{1}{\Delta_{1/2}} \right) I(\mathbf{r}), \quad (3.4)$$

where $\Delta_{3/2}$ and $\Delta_{1/2}$ now denote the detuning from the respective transition frequency. For red detuned light where the frequency ω is smaller than the transition frequencies ω_0 the atoms are attracted towards regions of high light intensities. Therefore, an optical dipole trap can be realized by the focus of a single red detuned laser. The benefit of such a trap is that the depth of the potential can be easily controlled by the laser intensity. This also allows for evaporative cooling by simply lowering the trap's depth and loosing atoms with high kinetic energies in the process. Eventually this leads to temperatures where the atoms condense to a BEC.

In our experimental setup this trap is realized by a focused CO₂ laser with a wavelength of 10.6 μm . Since the oscillation frequency of the CO₂ light is much smaller than the transition frequency of the rubidium atoms, the assumption $|\Delta| \ll \omega_0$ does not hold and the rotating wave approximation and thus equation (3.4) are not applicable. It is however possible to treat the trapping light field as a quasi static electric field that polarizes the atoms and to derive a quasi-electrostatic approximation for $\omega \ll \omega_0$ [38, 49]

$$V_{\text{CO}_2}(\mathbf{r}) = -\frac{3\pi c^2}{\omega_0^3} \frac{\Gamma}{\omega_0} I(\mathbf{r}). \quad (3.5)$$

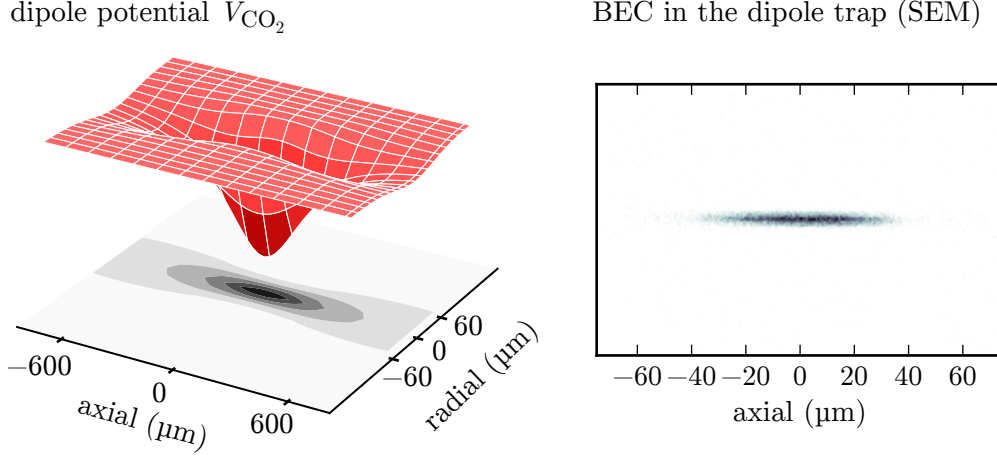


Figure 3.3: Shape of the optical dipole trap created by the focused CO_2 laser. The left part of the figure shows a horizontal slice of the dipole potential and illustrates the increasing trap depth towards the center of the focus. On the right a scanning electron microscopy (SEM) image of a BEC being held in the dipole trap is shown.

Also in the electrostatic case the potential is proportional to $I(\mathbf{r})$ and thus traps the atoms in the beam's focus. For our CO_2 dipole trap this focus is formed by an aspherical ZnSe-lens that is mounted inside the main vacuum chamber. It has a focal length of $f = 63 \text{ mm}$ and provides a beam waist of $w_0 = 30 \mu\text{m}$ at the focal point. A second lens is used to collimate the beam and guide it outside the chamber safely.

The intensity of the CO_2 laser is controlled with an AOM driven with up to 30 W of radio frequency (rf) power at a frequency between 30 and 50 MHz. Because some part of the rf-power is absorbed inside the germanium crystal, strong thermal effects resulting in pointing instabilities can be observed. These instabilities are causing a drift of the focus and therefore of the atoms held in the trap. To reduce this thermal effect, two rf-frequencies (35 MHz and 45 MHz) are applied simultaneously to the AOM, whose combined power is constant [51]. However, only the frequency at 45 MHz fulfills the Bragg condition for efficient diffraction. The ratio of the power between these two frequencies thus determines the laser intensity for the dipole trap. With this method a pointing stability of better than two millimeters at a distance of two meters behind the AOM is achieved. At the maximum available power of 30 W the depth of the dipole trap is 1.6 mK.

The left part of Figure 3.3 shows a horizontal slice of the dipole potential created by the CO₂ laser. The beam intersects the 3D-MOT so that the atoms collected at the beginning of an experimental sequence can be transferred to the CO₂ focus for evaporative cooling. The prepared atom sample can then be scanned by the electron microscope, producing an image as shown in the right part of Figure 3.3.

3.4 Optical Lattices

Since the geometry of an optical dipole trap only depends on the intensity distribution of the light that creates the potential, a variety of possible trapping geometries can be realized by shaping and/or combining multiple beams of light. A particularly interesting geometry can be created by superimposing two counter propagating laser beams. The standing wave that results from the interference pattern forms an optical lattice potential that became the basis of an interdisciplinary field of research [52]. Its small scale structure which is typically in the order of a few hundred nanometers also represents a convenient specimen for characterizing the performance of the scanning electron microscopy technique.

In the vicinity of its focus, the electric field $\mathbf{E}_{\mathbf{k}}(x, r, t)$ of a linearly polarized Gaussian beam that propagates in the x -direction can be written as

$$\mathbf{E}_{\mathbf{k}}(x, r, t) = \mathbf{E}_0 e^{-\frac{r^2}{w^2}} e^{ik_x x} \cdot e^{i\omega t}, \quad (3.6)$$

where r is the distance from the beam axis, $\mathbf{k} = k_x \hat{\mathbf{e}}_x$ is the wave vector and w denotes the beam waist at the focus. The intensity of two counter propagating beams with the same polarization is then given by

$$I(x, r) = |\mathbf{E}_{\mathbf{k}}(x, r, t) + \mathbf{E}_{-\mathbf{k}}(x, r, t)|^2 = 4 |\mathbf{E}_0|^2 \cos^2(k_x x) e^{-2\frac{r^2}{w^2}}. \quad (3.7)$$

Since the dipole potential $V(x, r)$ formed by the interfering light

$$V(x, r) = -V_0 \cos^2(k_x x) e^{-2\frac{r^2}{w^2}} \quad (3.8)$$

is proportional to the intensity $I(x, r)$, its periodicity is defined by the wavelength λ via $k_x = \frac{2\pi}{\lambda}$. Atoms that are trapped in a red detuned optical lattice will be pulled towards the standing wave's maxima, which are spaced by $\lambda/2$. The radial confinement of these maxima, commonly referred to as lattice sites, is given by the Gaussian envelope of the intensity distribution.

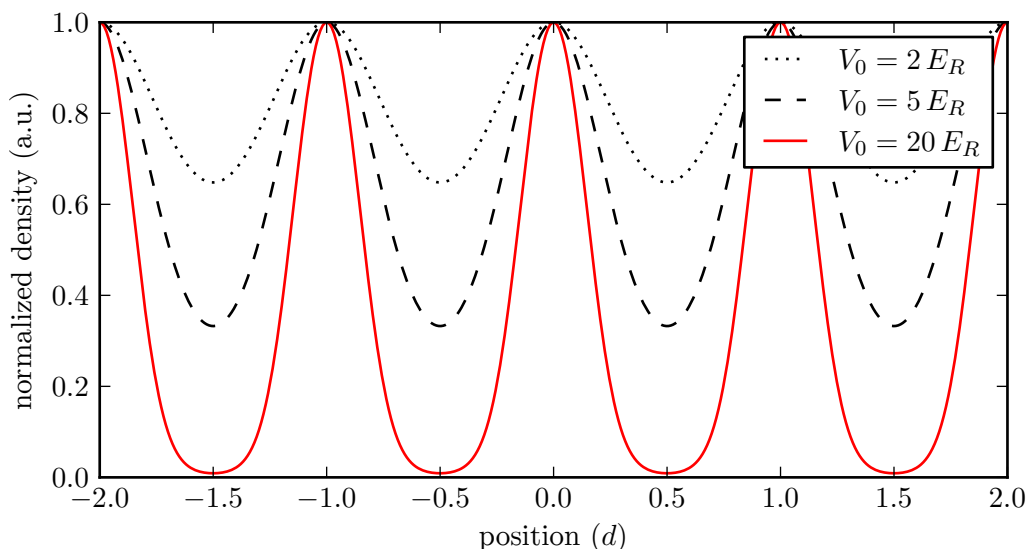


Figure 3.4: Expected density profile of optical lattices with lattice spacing d and varying potential depth V_0 . The profiles were numerically calculated using the imaginary time propagation method. For typical experimental parameters ($V_0 = 20 E_R$) the single lattice sites are well separated. An increasing overlap can be observed for lower potential depths V_0 which decreases the contrast of the lattice.

When superimposing this one-dimensional lattice on a trapped BEC, the atomic cloud is sliced into a series of pancake-like structures. The combination of multiple lattice beams also allows for structures of higher dimensionality like a 2D array of tube-like quantum gases. Due to the lack of optical access, the 2D lattice in this experimental setup is realized by four beams entering the main vacuum chamber at an angle of 45° instead of two horizontal retro-reflected lattice beams. For a wavelength of 852 nm the lattice spacing therefore amounts to $\frac{\lambda}{2 \cos(45^\circ)} \approx 600$ nm. Each beam is focused at the center with a waist of $500 \mu\text{m}$ and overlaps with the CO_2 dipole trap. An AOM controls the power of 300 mW per beam so that the lattice potential can be ramped up smoothly and without heating the atomic sample. The maximum potential depth V_0 is usually given in units of recoil energies

$$E_R = \frac{\hbar^2 k_{\text{eff}}^2}{2m}, \quad (3.9)$$

where k_{eff} denotes the wave number k reduced by $\cos(45^\circ)$ due to the geometry of the interference. With this setup a lattice depth of $V_0 = 20 E_R$ is

typically achieved¹. The distribution of atoms in an optical lattice strongly depends on the depth of the potential and is therefore of particular interest for the imaging procedures discussed in the next chapter.

For a BEC the density distribution can be numerically calculated using the imaginary time propagation method described in section 2.4. The computation is performed using the potential from equation (3.8) and enforcing the periodic boundary conditions of the lattice. The results shown in Figure 3.4 illustrate that the single sites are well separated for typical potential depths ($V_0 = 20 E_R$). For lower lattice depths the overlap of the sites increases and the contrast of the lattice vanishes.

Other characteristics like tunneling effects between neighboring lattice sites or particle counting statistics are usually described by the Bose-Hubbard model [55-58]. These aspects however do not affect the density distribution of a stationary system and are not considered in the context of scanning electron microscopy imaging.

3.5 Light-sheet Trap

Although the CO₂ dipole trap and the optical lattices enable a broad spectrum of possible experiments, the investigation of thermal correlations in cold quantum gases requires yet another trap geometry that must be realized by an additional laser setup. As explained in the theoretical introduction of correlations in a later chapter, a very thin trapping potential is required in order to measure the thermal bunching effect using scanning electron microscopy.

To this end, an optical setup has been designed that strongly focuses a red detuned laser in the vertical direction while providing a very balanced intensity distribution in the horizontal plane. Its detailed technical description is found in previous works [59]. The tight beam waist of 6.5 μm in the z direction of the focus allows for very high intensities with little demand in power. A standard grating stabilized laser diode emitting at $\lambda = 852 \text{ nm}$ is sufficient for achieving a vertical trapping frequency of $\omega_z = 2\pi \times 435 \text{ Hz}$ when using 3 mW of power. With a horizontal beam waist of 130 μm at the focus, the trapping frequencies in the x and y directions are $2\pi \times 8 \text{ Hz}$ and $2\pi \times 30 \text{ Hz}$. The depth of the potential can be controlled by an AOM that also stabilizes the available laser power.

¹An in-depth description of this setup is found in previous works [38, 53, 54].

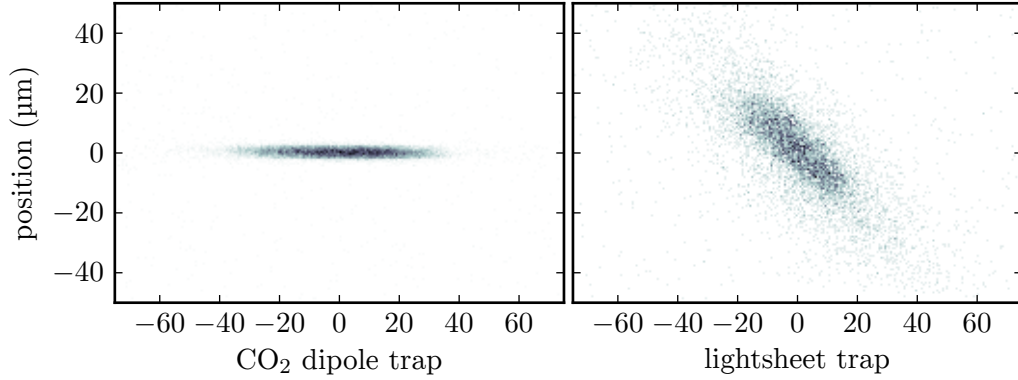


Figure 3.5: *Scanning electron microscopy images of a BEC before and after being transferred from the CO_2 dipole trap to the light sheet trap. The aspect ratio of the atomic cloud visibly shifts from 1 : 14 to 1 : 4, providing a more evenly shaped density distribution in the horizontal plane.*

If an ultracold sample of atoms is to be prepared in the optical light sheet, we first start with a regular experimental sequence loading atoms from the 3D-MOT into the CO_2 for evaporative cooling. After reaching the desired temperature and number of atoms in the first optical trap, the light sheet is superimposed and intersects the CO_2 trap at an angle of 45° . While it is ramped up using the AOM, the power of the CO_2 is reduced at the same time so that eventually the atomic cloud is transferred to the new trap. Figure 3.5 shows a scanning electron microscopy image of a BEC before and after the transfer process and illustrates the change in the horizontal trapping geometries.

3.6 Electron Microscope

The optical dipole traps which have been introduced in this chapter were designed to provide a versatile platform to prepare atomic samples for the scanning electron microscope. Imaging the atomic clouds by means of scanning electron microscopy differs from the standard imaging techniques.

The signal generation is based on electron impact ionization of the trapped atoms with subsequent ion detection. An overview over the operation of the electron microscope shall be provided in the following. In-depth descriptions of the technical details and the electron-atom interactions are found in previous works [38, 60, 61].

3. A SCANNING ELECTRON MICROSCOPE FOR ULTRACOLD ATOMS

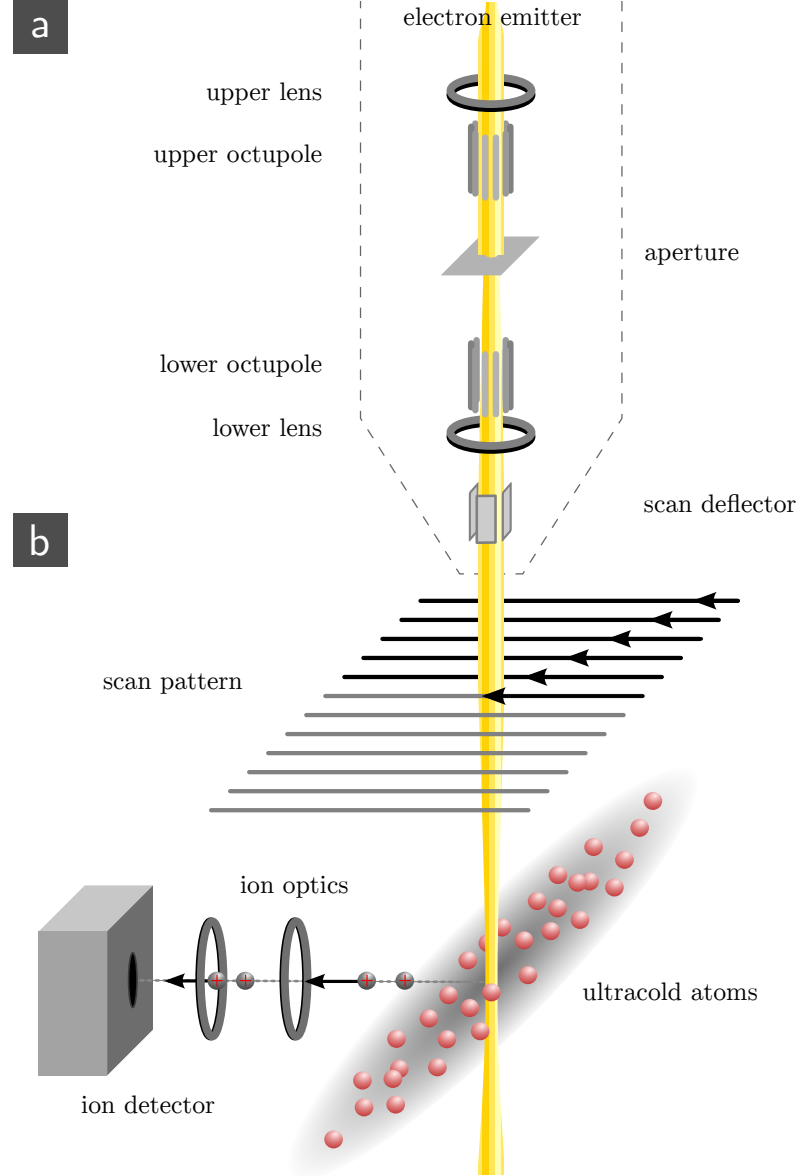


Figure 3.6: Working principle of the electron microscope. A schematic view of the electron column, represented by the dashed line, is shown in the upper half of the figure (a). A detailed description of the elements is given in this chapter. (b) The column provides a focused electron beam which intersects a cloud of ultracold atoms prepared in an optical dipole trap. Electron impact ionization produces ions which are guided by ion optics towards a detector.

A sketch of the working principle is shown in Figure 3.6. The upper half of the figure shows a schematic view of the electron column. It contains a thermal Schottky emitter and standard electron optics, consisting of two magnetic lenses, a variable aperture and a set of deflectors and stigmators. The emitter is designed to extract and accelerate electrons to an energy of 6 keV.

An initial collimation of the electron beam is achieved by the upper magnetic lens. Two deflector/stigmator units, each being realized as a single octupole element, are used to align the beam along the electron optical axis and to correct for astigmatism. A variable aperture is used to set the beam diameter inside column and the beam current. The second magnetic lens focuses the electron beam at a working distance of 13 mm below the tip of the electron column. Between both lenses, the electrons travel about 35 cm. The geometry of the lenses is such that the virtual electron source, which lies inside the emitter tip, is magnified at the position of the atoms by a factor of four. Assuming a virtual source size of 20 nm [62], the FWHM beam diameter of the electron beam is about 80 nm. The real probe size can be substantially larger due to spherical aberration errors. Their influence can be reduced by choosing a smaller aperture that decreases the beam's radial extension inside the column at the cost of beam current. The beam diameter may also be decreased by changing the excitation in both lenses to reduce the magnification. This leads to a more divergent beam between both lenses and an increase of spherical aberrations. Again, an aperture is required to compensate for this effect. The general trade-off between beam current and beam size is a common feature of all charged particle optics. For the experiments presented in this thesis a high spatial resolution was preferred over high beam currents. Typical operating parameters for the fully aligned electron microscope featured a FWHM of 100 nm with a beam current of 15 nA using the 50 μm aperture.

The lower part of Figure 3.6 depicts the scanning and detection procedure. A pair of electrostatic deflectors close to the tip of the column allows to move the electron beam within an area of 1 mm \times 1 mm in the focal plane. For applying arbitrary scan patterns, the deflection can be controlled externally with a bandwidth of 20 kHz. Usually a simple rectangular scanline pattern is chosen for creating scanning electron microscopy images. The electron beam intersects the prepared atomic sample and causes a local ionization of atoms from the cloud due to electron-atom scattering. Ion optics which consist of a set of electrostatic elements are guiding the ions to a channeltron detector. Knowing the electron beam's position, the ori-

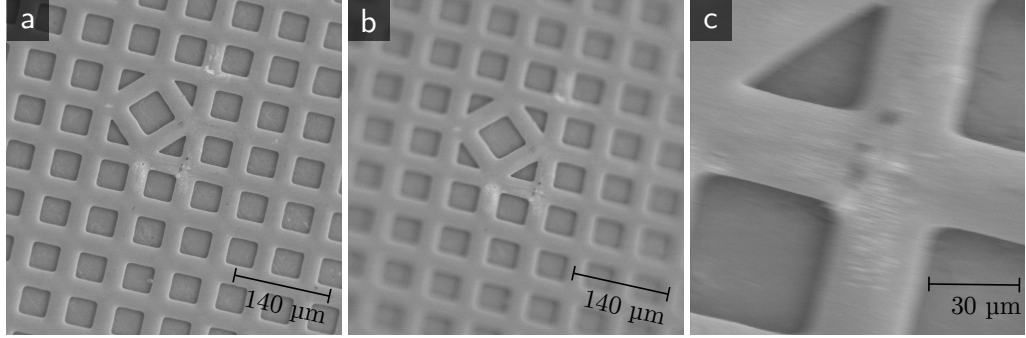


Figure 3.7: Scanning electron microscopy images of the grid test target during beam alignment. Figure (a) shows an undisturbed image after the completion of the alignment process. In the second image (b), the field of view suffers from spherical aberrations due to misaligned deflector elements. The quality of the beam degrades for increased distances from the center. In image (c) an astigmatic beam causes blurring in the horizontal axis over the whole field of view.

gin of an incoming ion can be determined by back-projecting the time resolved detection event to the scanning pattern.

Apart from the beam size and its shape, the quality of the field of view is of great importance. A first adjustment is achieved by imaging the surface of a grid test target. It is mounted on a manipulator arm that can be moved inside the electron beam. The grid structure of the target enables the optimization of the field of view and the correction for astigmatism. Figure 3.7 shows the progress and the result of such an adjustment. Scanning across the sharp edge of the hole target which is mounted next to the grid allows to determine the beam diameter. One important difference of an electron imaging system compared to an optical technique is its large depth of focus. This is verified by changing the vertical position of the hole target and evaluating the edge spread function. Figure 3.8 shows the result for an electron beam with a beam diameter of 120 nm (FWHM). At larger distances, the size starts to increase linearly. Translated into the language of optics, the geometry of the electron beam focus corresponds to a Rayleigh length of 35 μm at a beam waist of 130 nm. Consequently, the size of the beam may be regarded as constant throughout the extension of a typical atomic sample (6 μm).

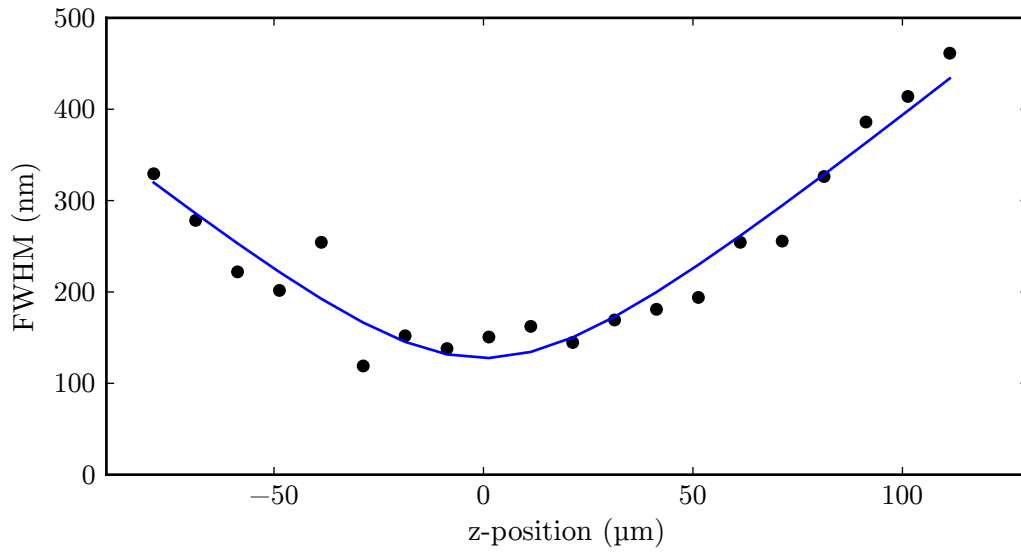


Figure 3.8: Depth of focus of the electron beam. Scanning across the edge of the hole test target allows to measure the diameter of the electron beam. This measurement has been repeated for different positions of the test target in the vertical direction without readjusting the electron optics in the process. In this exemplary measurement, the geometry of the electron beam focus corresponds to a Rayleigh length of $35\mu\text{m}$ at a beam waist of 130 nm .

Imaging Ultracold Quantum Gases

Imaging processes are of most importance to an experimentalist. Not only the capabilities for preparation and manipulation of a physical system, but also the development of new possibilities for extracting information is constantly progressing. Naturally, much effort is taken to enhance our ability to literally see the objects we are interested in. When imaging cold or ultracold quantum gases, many experiments rely on optical imaging methods for observations. By determining the light emitted or absorbed by atoms, it is possible to measure the density of atomic distributions or to detect single atoms. Imaging the density distributions of interacting gases is particularly interesting for extracting information about thermodynamic properties, like the temperature and the chemical potential of a system. Also, especially in low dimensional systems the measurement of quantities like phase-space density and pressure gained recent interest [63]. Usually a high spacial resolution is desired in order to obtain as much information as possible about an atomic ensemble.

A technique that inherently provides much higher spatial resolution than optical methods is scanning electron microscopy, which has proven to be a powerful way of imaging [62]. Initially, it allowed for scanning the surface of metallic objects by either measuring secondary or backscattered electrons from a focused electron beam. In this manner, rasterized images with a spatial resolution in the order of few nanometers and below were obtained. The method greatly outperforms any optical imaging method, which is possible due to the small de Broglie wavelength of the accelerated electrons.

This concept has been transferred to the field of cold atom systems by modifying the detection scheme. For scanning a gaseous target, the electron microscope relies on the effect of electron impact ionization and subsequent detection of produced ions. It therefore combines the high spatial resolution of a focused electron beam with the single particle sensitivity of ion detection. In its application, electron microscopy involves several aspects that are different from standard optical imaging techniques. The scanning probe principle involves a sequential image formation where the image reconstruction is performed by correctly assigning the detected ion events to the position of the electron beam.

This relatively simple methodology is complicated by several aspects that are discussed in this chapter. We first introduce a correction algorithm for falsely assigned ion detection events in the image formation procedure. The application of this post-process is demonstrated on a scanning electron microscopy image of a trapped BEC by comparison to theory. This topic is then followed by the imaging and dissipative manipulation of optical lattices. In this context, we will discuss methods for quantifying and optimizing the performance of the electron microscope.

4.1 Time of Flight Unfolding

When assigning ion detection events to coordinates of a scanning pattern, knowledge of the time of production of the ions as well as the position of the electron beam at this time is required. Apart from a negligible signal processing delay of about 160 ns, the time lag between ion production and detection is directly determined by the time of flight of the particles. It depends on the strength of the electrostatic field of the ion optics, the mass of the particles and their charge.

From an experiment measuring the time of flight spectrum for the produced ions, the time of flight for singly charged ^{87}Rb ions in the experimental setup is determined as $\Delta t_1 = 18 \mu\text{s}$. A detection event occurring at time t is therefore mapped to the electron beam's position at $t - \Delta t_1$. This simple model is correct for most of the detection events, but about 20 % of the ions produced are multiply charged. Their time of flight differs from the singly charged particles, as it is apparent from Figure 4.1. Since the detector cannot distinguish between multiply charged states, the time of production is estimated incorrectly for any but the singly charged ions. In consequence, multiply charged ions are attributed to preceding imaging coordinates. When producing an image using the rectangular

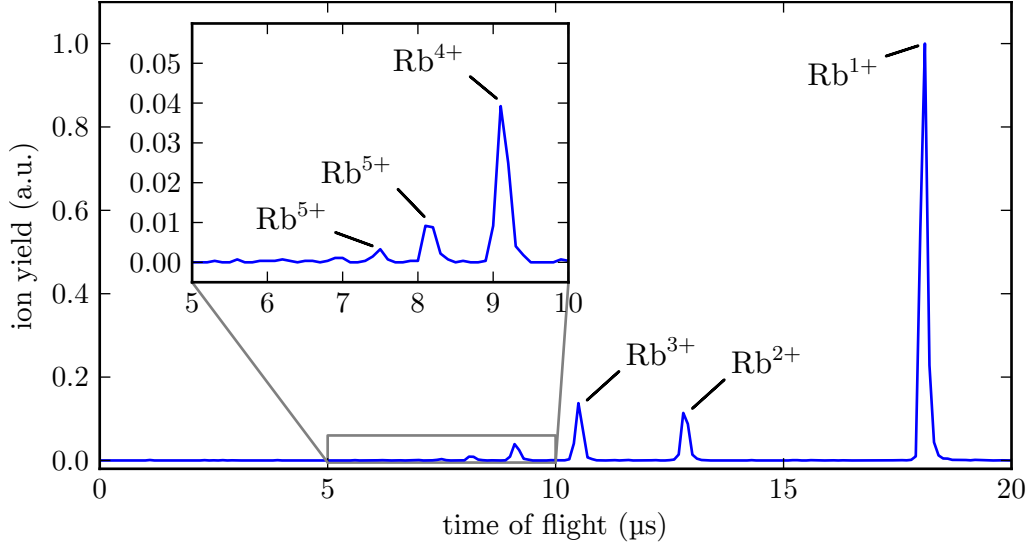


Figure 4.1: Time of flight spectrum of ^{87}Rb atoms ionized by electron-atom scattering. At $t = 0$ the electron beam has been activated for a short duration of 100 ns. A histogram of ion arrival times relative to the beam activation is then recorded. The peaks in this spectrum correspond to the multiply charged states up to Rb^{6+} . About 80% of all detected ions are singly charged.

scanning pattern, each multiply charged state adds an overlaying image, shifted according to its shorter time of flight (Figure 4.2a). The amount of this shift is proportional to the scanning speed, thus it increases as the dwell time per pixel in an image is reduced.

The detected signal can be understood as a convolution of the number of ions $n(t)$ produced at time t and the time of flight spectrum, which acts as a point spread function $h(t)$. A generic approach is the deconvolution of the signal $\tilde{s}(t)$. The effects of the point spread function are formally undone by a multiplication with its inverse in Fourier space. However, measurements usually introduce additional noise which is greatly amplified when applying a direct deconvolution. To overcome this numerical instability, the Wiener filter method [64] includes a dampening factor for frequencies with low signal to noise ratio. A smoothed signal is restored if the point spread function is known, while guessing the noise spectrum of the measurement. Unfortunately, the deconvolution exhibits small oscillations and choosing the dampening factor adds an unwanted degree of freedom to the post-process. We will therefore develop an alternative and more empirical approach that does not inherit the mentioned drawbacks.

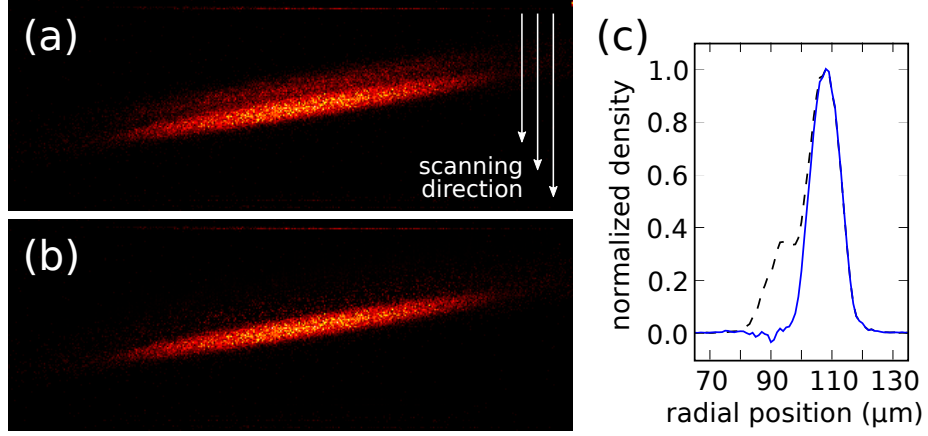


Figure 4.2: Image of a BEC in an optical dipole trap being corrected for time of flight effects. Image (a) clearly suffers from multiply charged ions being attributed to incorrect pixels due to their different time of flight. The dwell time per pixel for this image is $0.5 \mu\text{s}$. A corrected image (b) is obtained by recursively removing intensity from neighboring pixels. Figure (c) shows an integrated linescan along the trap axis of both images for comparison. The dashed line corresponds to the original image (a), whereas the solid line shows the profile of the corrected image (b).

For simplicity the time of flight spectrum seen in Figure 4.1 is treated as a series of infinitesimally narrow peaks

$$h(t) = \sum_i \gamma_i \delta(t - \Delta t_i). \quad (4.1)$$

The probability for producing an ion of charge state i shall be denoted as γ_i and its time of flight as Δt_i . The detected signal $\tilde{s}(t)$ may then be written as

$$\tilde{s}(t) = n(t) \star h(t) = \sum_i \gamma_i n(t - \Delta t_i). \quad (4.2)$$

Based on the information from the time of flight spectrum, the undisturbed signal $n(t)$ can be approximated by recursively removing the fractions of counts that were attributed incorrectly. For convenience, the first $18 \mu\text{s}$ are clipped from the signal so it is shifted by Δt_1

$$s(t) = \tilde{s}(t + \Delta t_1) = \gamma_1 n(t) + \sum_{i=2} \gamma_i n(t + |\Delta t_1 - \Delta t_i|), \quad (4.3)$$

$$n(t) = \frac{1}{\gamma_1} s(t) - \sum_{i=2} \frac{\gamma_i}{\gamma_1} n(t + |\Delta t_1 - \Delta t_i|). \quad (4.4)$$

The unknown function $n(t)$ now depends on the signal $s(t)$ and on contributions of $n(t)$ from later times. If the ion production stops $18\text{ }\mu\text{s}$ prior to a specific moment t_{max} and $n(t)$ becomes zero

$$n(t) = 0 \quad \forall \quad t > t_{\text{max}}, \quad (4.5)$$

the last ions detected must be singly charged, since the Rb^+ ions are the slowest particles to arrive. In this case no multiply charged ions contribute to the signal, and the number of ions produced at this specific time is directly obtained by

$$n(t_{\text{max}}) = \frac{1}{\gamma_1} s(t_{\text{max}}). \quad (4.6)$$

It is now possible to calculate $n(t)$ reversely from t_{max} to $t = 0$ since the recursion ends within $n(t)$. The calculation is implemented as follows.

Beginning at t_{max} , a fraction $\frac{\gamma_i}{\gamma_1}$ from the signal bin $s(t)$ is subtracted from a preceding bin $s(t - |\Delta t_1 - \Delta t_i|)$. This preceding bin is now cleared from the specific charged state i and should be clear of all multiply charged states once the algorithm proceeded to the bin. The result of this post processing method is shown in (Figure 4.2b).

Although some noise has been transferred from the real density-distribution signal to the area where the duplicated image was, the time of flight artifact is considerably reduced. Figure 4.2c shows the axis integrated line densities for comparison. The dashed line corresponds to the original image, whereas the solid line represents the profile of the corrected image.

4.2 BEC Density Profile

After the successful creation of a Bose-Einstein condensate within the electron microscope apparatus, it is a logical step to test the imaging capabilities on a known atomic target in conjunction and comparison with conventional absorption imaging. Optical imaging methods are frequently chosen as simple and reliable way for determining the temperature and the number of particles of a quantum gas. These parameters are usually measured after free expansion, as the length scales of a trapped gas are very small and cannot be resolved easily.

In this section, we will derive these parameters from a distribution that was measured *in situ* by averaging over multiple high resolution scanning electron microscopy images. In a repeated experimental cycle, a BEC

is produced and held inside the CO_2 dipole trap. The electron beam is moved using the standard rectangular scanning pattern over an area of $120\text{ }\mu\text{m} \times 45\text{ }\mu\text{m}$ so the whole extent of the cloud is covered. The ion detection events produced in this process are recorded into 60,000 channels, providing images with $300\text{ nm} \times 300\text{ nm}$ resolution. After a total scanning time of 120 ms the atoms are released from the trap and an absorption image is taken after 18 ms time of flight before the experimental cycle begins anew. Each electron microscopy image contains an average of 350 detected atoms.

The total number of atoms as determined from the absorption images is about 100,000. No significant difference is found in the density distribution when comparing the condensate with and without exposure to the electron beam, apart from a reduction in atom number by about 7%. These losses are composed of primary electron atom collisions and secondary collisions of reaction products. In all these collisions the energy transfer is much larger than the depth of the optical potential and all scattered particles can escape from the trap. Essentially no energy is deposited in the cloud, as an additional heating of merely 5 nK after exposure to the electron beam is observed. Thus, the perturbation of the condensate during the scanning process is negligible.

It is therefore concluded that the measured mean cloud density resembles the true distribution of atoms. However, a post processing of the data is necessary in order to address two effects that are broadening a simple average over all measured densities. First we need to correct positional jitter, mainly caused by focal drifts of the CO_2 laser, by determining the center of mass for each image and re-centering them before the accumulation. The next step is to correct for the different arrival times of multiply charged ions which affect the time resolved ion signal. Since the electron beams fast scanning direction was roughly aligned to the radial axis of the BEC, the clouds width appears broadened. This effect is addressed by applying the correction algorithm described in section 4.1. Furthermore, the image is rotated with bi-linear interpolation to match the atom clouds axes to the coordinate system. Taking the sum of the image along the vertical and horizontal direction now gives us the integrated axial and radial line densities of the BEC, which are most illustrative for examining the density profile.

Usually, when analyzing absorption images after time of flight a bimodal distribution of a Thomas Fermi approximated BEC and a Gaussian ther-

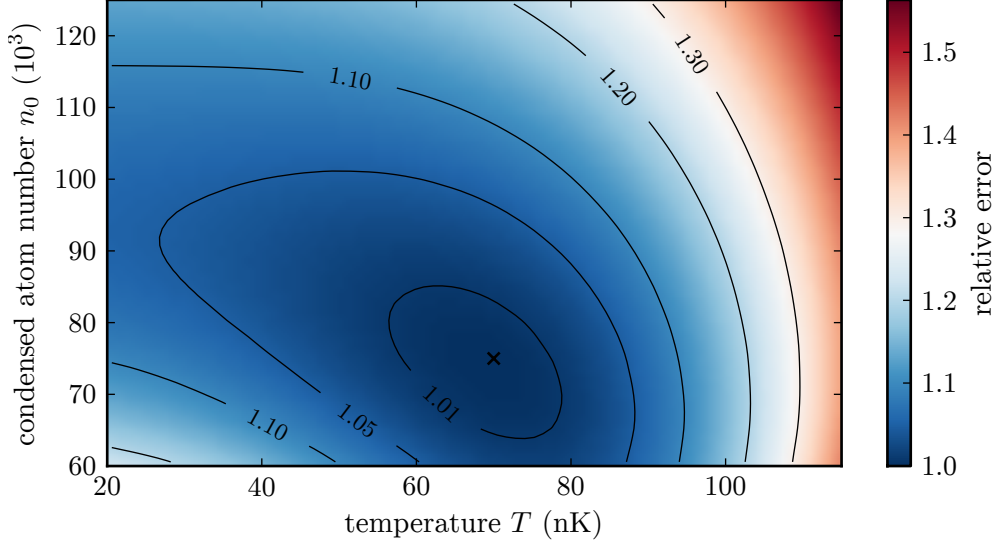


Figure 4.3: Interpolated plot of the squared differences χ^2 between measured density profile and calculated semi-ideal model for different simulation parameters. Best agreement is found for a temperature of $T = 70$ nK and condensed atom number of $n_0 = 75 \times 10^3$. The innermost area limited by the dashed lines contains solutions that differ only by 1% in χ^2 .

mal component is fitted to the retrieved density profile. For the analysis of an in situ measured distribution a different method is required, as the temperature of the cloud cannot be extracted in the same manner. The semi-ideal model introduced in section 2.5 is a bimodal distribution at finite temperature with a thermal component modeled as a non-interacting gas in an effective potential, taking into account the repulsion of the thermal atoms by the condensed atoms. Since the wings of the density distribution contain most of the information regarding the thermal component, these regions must be described as precisely as possible. To this end, the BEC ground state is calculated numerically by imaginary time propagation instead of using the Thomas Fermi approximation, which is inaccurate for regions of low density.

The semi-ideal model has only two free parameters, the number of atoms in the ground state n_0 and the temperature T of the thermal component. The parameters of the external trapping potential were determined experimentally. Numerical computation of the semi-ideal model is very expensive and is therefore not suited for application in standard iterative fitting algorithms. Instead, the density profile is calculated for a reasonable range of parameters n_0 and T , which is done in parallel utilizing

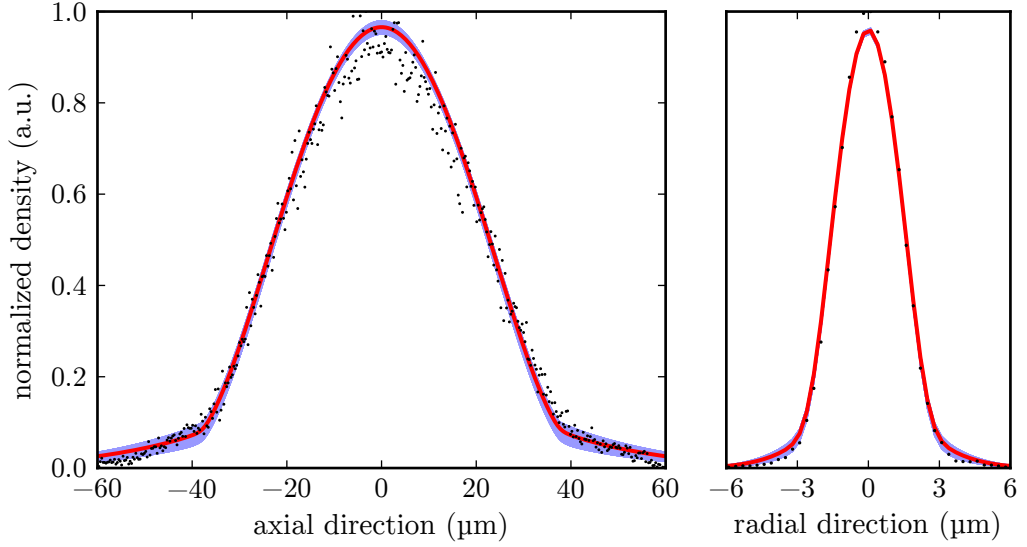


Figure 4.4: Axial and radial line densities of the BEC in comparison with the semi-ideal model (red line) for $n_0 = 75 \times 10^3$ and $T = 70$ nK. The profiles for parameters leading to an increase of χ^2 within 1% of the optimal solution are shown as blue background and illustrate the areas of most influence for the result.

multiple systems. All these simulated density distributions are compared to the imaged profile. Since the absolute area densities from the scanning electron microscope image are unknown, a linear scaling factor for each simulation is found, minimizing the squared pixel differences χ^2 .

In Figure 4.3, the behavior of the minimum χ^2 values with respect to the simulation parameters is shown. The best agreement is found for a temperature of $T = 70$ nK and a condensed atom number of $n_0 = 75,000$. Including a number of 18,000 thermal atoms, the total number of 93,000 atoms predicted by the semi-ideal model for the best fitting parameters is remarkably close to the number of 100,000 atoms seen in the absorption images.

Figure 4.4 shows the integrated line densities in axial and radial directions of the BEC in comparison with the best fitting model. Density profiles for parameters leading to an increase of χ^2 within 1% of the optimal solution are shown in the background. This illustrates the strong influence of the distribution's wings when determining the thermodynamical parameters. A minor mismatch of the model's maximum line density compared to the axially and radially integrated measurement further indicates a slight inaccuracy in the assumed trap aspect ratio.

In conclusion, the semi-ideal model is in very good agreement with the profile measured by scanning electron microscopy, and the parameters are compatible with the temperature and atom number obtained from time of flight absorption imaging. A noteworthy detail is that the parameters were determined merely from the shape of the distribution without knowledge of the absolute scaling, which depends on the ionization cross section and the ion detection efficiency. The good agreement with the semi-ideal model also gives indirect evidence of the repulsion between the condensate fraction and the thermal component in the trap.

4.3 Imaging Optical Lattices

The analysis of the BEC in the optical dipole trap shows that scanning electron microscopy is indeed well suited for measuring density distributions, but it does not yet demonstrate its capability in high resolution imaging. To this end, a system with smaller characteristic length scales is required, which is achieved by means of optical lattices.

Their use soon began after the first realization of Bose-Einstein condensation, when ultracold atoms were transferred into arrays of microscopic traps formed by interfering laser beams [65, 66]. This opened up novel possibilities for strongly correlated many-body physics and the preparation of low-dimensional systems [58, 67, 68]. Although the distribution of atoms within optical lattices was measured for larger lattice spacings [69], imaging the small structure of a lattice with sub-micrometer resolution has been achieved first by scanning electron microscopy [22, 70]. This technique not only allowed the imaging, but also the selective removal of atoms from single sites prior to the scanning process.

Apart from their use in realizing quantum mechanical systems for experimental study, optical lattices also play a vital role in the characterization and adjustment of the electron microscope. The analysis of periodic structures serves as a reliable method for determining and optimizing electron beam parameters, enabling other applications with high demands in precision. One example that greatly benefits from this procedure is the measurement of spatio-temporal correlations which are discussed in a later chapter. In the following, the image formation and analysis of optical lattices shall be explained in detail.

Lattice Orientation and Periodicity

As already seen in the image formation process of a BEC in the optical dipole trap, only a fraction of atoms is ionized and detected during a single typical scan. It is tempting to again accumulate the images from many experimental realizations in order to increase the signal. In the case of optical lattices, the sum of the data usually results in a blurred image due to slow drifts or unpredictable fluctuations of the interference pattern that creates the periodic potential. We can compensate for shot-to-shot movement in a post process similar to digital image stabilization algorithms [71]. This is done by identifying traceable features and their positions within consecutive images and cancel out movement by shifting the images. In our application, these features are the sites of the optical lattice. Their positions are determined by the phases $\phi_{1,2}$ of the two standing waves formed by the counter-propagating lasers. To this end the lattice structure, its orientation and periodicity, must be analyzed and the phases are to be determined for each image.

A two-dimensional lattice structure can be described by two lattice translation vectors $\ell_{1,2}$, pointing from one site to its next neighbors in each direction. These vectors are not necessarily perpendicular. The lattice may also be represented by two plane waves with wave vectors $\mathbf{k}_{1,2}$, which define the reciprocal lattice. The first step is to precisely determine both wave vectors. The discrete two dimensional autocorrelation function $A(\Delta x, \Delta y)$ for a given signal $s(x, y)$

$$A(\Delta x, \Delta y) = \sum_{x,y} s(x, y) s(x - \Delta x, y - \Delta y), \quad (4.7)$$

is an intuitive tool for identifying periodic signals. Since it does not depend on the absolute position of the signal, the results from multiple images can be accumulated regardless of fluctuations. This sum is an image with very low noise from which the wave vectors $\mathbf{k}_{1,2}$ can be obtained by finding the two most prominent peaks in the Fourier spectrum.

An equivalent and computationally faster method is to directly calculate the power spectrum $P(f_x, f_y)$ with the spatial frequencies $f_{x,y}$ for each single image using the fast Fourier transform (FFT) algorithm. Its relation to the autocorrelation function is stated by the Wiener-Khinchin theorem

$$\mathcal{F}[A(\Delta x, \Delta y)] = P(f_x, f_y) = |\mathcal{F}[s(x, y)]|^2, \quad (4.8)$$

where \mathcal{F} denotes the Fourier transform of the functions A and s . Figure 4.5 shows the power spectrum of a simulated image of an optical lattice. The

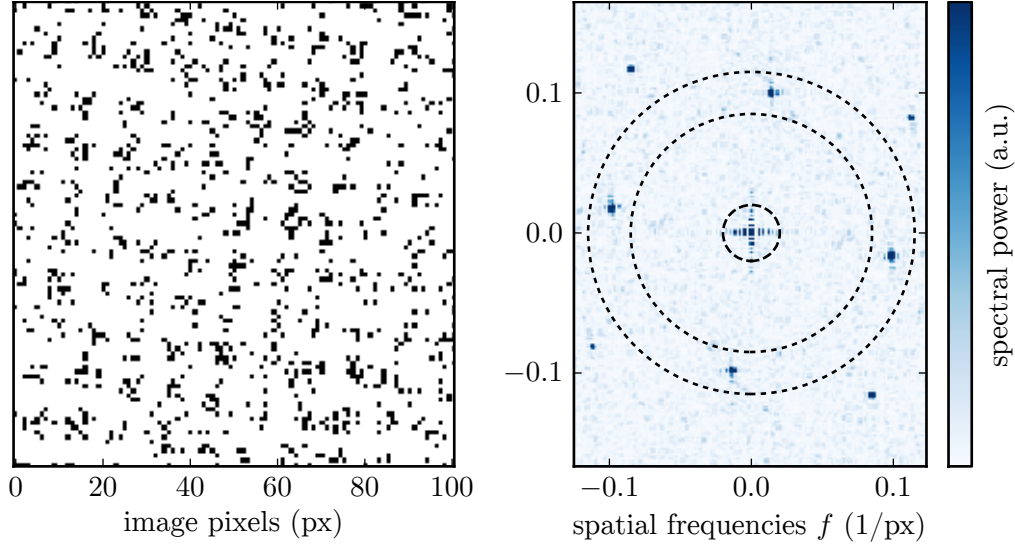


Figure 4.5: Power spectral density of a simulated scanning electron microscopy image. The black dots in the test image on the left are random samples of a two dimensional probability function with a periodicity of 10 pixels. The power spectrum of this data is shown on the right. After masking out the low frequency contributions (innermost dashed line), the spectrum is searched for the highest peak. Once this peak is found, the search for a second peak is restricted to an area of similar periodicity (dotted outer region).

data is created by taking random samples from a periodic test distribution and resembles a typical scanning electron microscopy image. After calculating the power spectrum of the signal, the most prominent frequency within the image is identified by searching for the highest peak. Low frequency contributions which are of no interest must be excluded from this search. When looking for a two dimensional structure, the region of the first peak is masked out and the search is continued for a second peak at similar frequency. Since the data is discrete, the positions of the peaks are of coarse accuracy. An accurate estimate for the peak positions is obtained by parabolic or Gaussian interpolation, taking the surrounding pixel values of the spectrum into account. For typical parameters, the accumulation of about 20-30 images containing an amount of 200 detection events each is enough to provide very accurate estimates of the spatial frequencies $f_{x,y}$ and thus the wave vectors $\mathbf{k}_{1,2}$ of the lattice structure

$$\mathbf{k} = 2\pi \begin{pmatrix} f_x \\ f_y \end{pmatrix}. \quad (4.9)$$

Lattice Phases and Amplitudes

Once the wave vectors are determined they can be regarded as constant throughout a series of measurements. This requires that the scaling and orientation of the scan pattern remain unchanged and that shearing effects due to electron-beam realignment are negligible. With knowledge of \mathbf{k}_1 and \mathbf{k}_2 , the Fourier components $\hat{f}(\mathbf{k}_{1,2})$ of the single images can be calculated

$$\hat{f}(\mathbf{k}_{1,2}) = \sum_{x,y} e^{i(k_x \cdot x) + i(k_y \cdot y)} s(x, y) = \tilde{a}_{1,2} e^{i\tilde{\phi}_{1,2}}. \quad (4.10)$$

The components, when expressed as amplitudes $\tilde{a}_{1,2}$ and phases $\tilde{\phi}_{1,2}$, yield two quantities of great importance. First, we obtain the phases required for correcting lattice drifts that are blurring the accumulated images from multiple measurements. Due to the finite window length of the signal, the calculated phases $\tilde{\phi}_{1,2}$ are generally not equal to the phases $\phi_{1,2}$ of the plane waves forming the structure. However, for typical image sizes, the approximation of $\phi_{1,2}$ by $\tilde{\phi}_{1,2}$ is valid within 1%. Second, the Fourier amplitude $a = \tilde{a}/N$, after being normalized by the number of ions N , can be used to quantify the contrast of the signal and thus the effective diameter of the electron beam.

For a better understanding of these quantities, the analysis is performed on a series of simulated images with randomly generated ion detection events. The detection probability follows a two dimensional periodic distribution of Gaussian functions, mimicking the density profile of an optical lattice. In analogy to typical experimental parameters, the chosen image size is 250×250 pixels, with a spacing of 20 px between the lattice sites (600 nm). For a potential depth of $s = 20$, the FWHM of the single sites is assumed to be 177 nm. In Figure 4.6, the measured Fourier amplitudes and phase determination errors are shown for various widths of an electron beam reducing the perceived contrast ¹. For Fourier amplitudes above 0.1, the wave vectors $\mathbf{k}_{1,2}$ were successfully found with a precision of 1% or higher. As the width of the electron beam decreases, the Fourier amplitude and the certainty in determining both amplitude and phase rises. A second series of simulations investigates the stability in dependence of the signal strength. As also seen in Figure 4.6, the error in determining phase and amplitude drops for higher number of ions N . Both relative errors decrease proportional to $1/\sqrt{N}$ as one might expect.

¹A generalized representation for arbitrary length scales is found in Figure A.1.

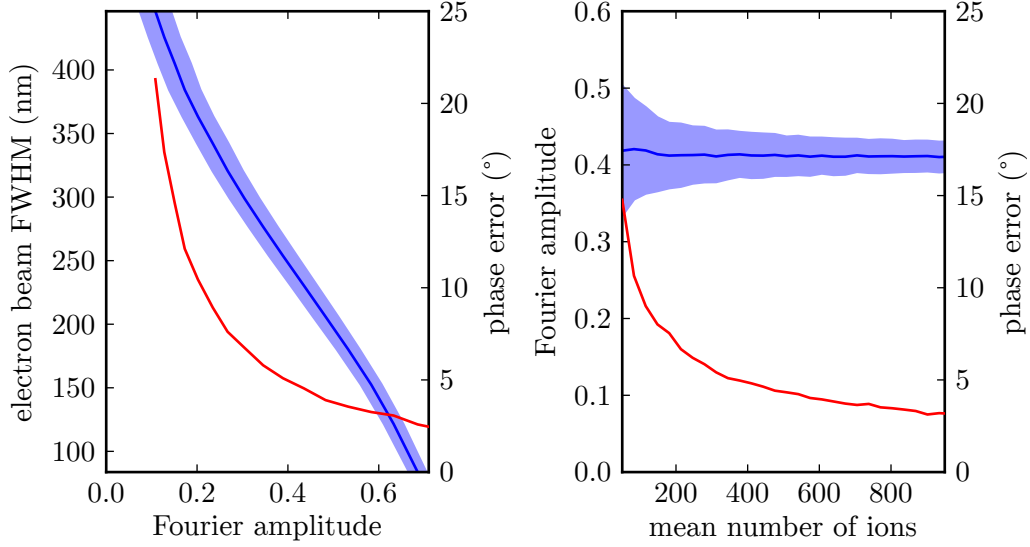


Figure 4.6: Analysis of simulated lattice images for various contrasts and ion numbers. In graph on the left, the Fourier amplitudes for a lattice of 600 nm spacing with a FWHM of 177 nm for the single sites are shown for different electron beam widths (blue, left scale). The error in determining the phases (red, right scale) is given in dependence of the Fourier amplitude. The standard error of the amplitude is depicted by the blue background. The curve diverges for amplitudes close to 0.1 as the analysis fails to extract the correct parameters. In the graph on the right, the stability of the Fourier amplitude (blue background) and phase (red) is shown for different ion numbers. The precision of both quantities increases for higher number of ions contained in the single images, while the absolute amplitude (blue line) remains constant.

There are of course alternative strategies to the described procedure for obtaining a measure of contrast and phase. However, no significant change in accuracy was found when maximizing the Fourier amplitude for each single image by variation of the wave vectors. Similar characteristics in accuracy were also found for sums over the areas covering the power spectrum peaks. Both alternatives will not be pursued further, as they only increase the computational effort without providing much benefit.

Phase Correction

Once the phases $\tilde{\phi}_{1,2}$ are known for each image within a series, the data can be shifted to compensate for the lattice instabilities. The shift occurs in the direction of the the lattice translation vectors $\ell_{1,2}$ that define the reciprocal lattice of the wave vectors $\mathbf{k}_{1,2}$. These translation vectors are

given by [72]

$$\ell_1 = 2\pi \frac{\mathbf{k}_2 \times \mathbf{k}_3}{\mathbf{k}_1 \cdot (\mathbf{k}_2 \times \mathbf{k}_3)}, \quad (4.11)$$

$$\ell_2 = 2\pi \frac{\mathbf{k}_3 \times \mathbf{k}_1}{\mathbf{k}_1 \cdot (\mathbf{k}_2 \times \mathbf{k}_3)}. \quad (4.12)$$

For a two dimensional system, the vector \mathbf{k}_3 is simply replaced by the unit vector in z direction. The spatial translation $\Delta \mathbf{r}$ is then given by

$$\Delta \mathbf{r} = \frac{\tilde{\phi}_1}{2\pi} \ell_1 + \frac{\tilde{\phi}_2}{2\pi} \ell_2. \quad (4.13)$$

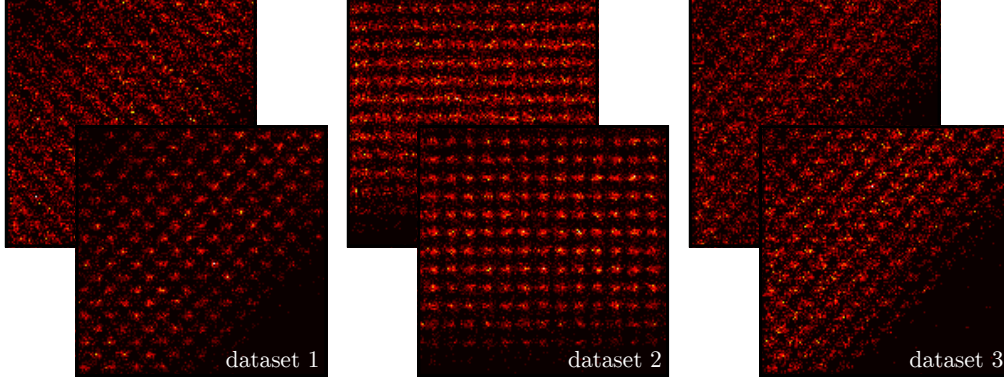
The compensation for the lattice drifts can now be performed by shifting each single image by the translation $\Delta \mathbf{r}$ that has been determined from the phases $\tilde{\phi}_{1,2}$. After this correction all images are correctly aligned and can be accumulated to an image of high signal to noise ratio that is unaffected by motion blur.

For some applications, such as the preparation of single lattice sites using the electron beam, an online correction method might be desired. It eliminates the need of a post process and increases the number of runs with successfully addressed single sites. This can be achieved by imaging and phase-analyzing only a small area of the lattice before proceeding with its preparation. From the simulations, the relative error in determining the position of the lattice is estimated as $\frac{\Delta \phi}{\pi} \approx \frac{1}{\sqrt{N}}$. For a desired accuracy of 5% one would need a signal that consists of at least 400 ions. Such an image could be taken on an outer part of the cloud and would require an imaging time of a few ten milliseconds. If the plane wave vectors are already known, the calculation of the Fourier components $\hat{f}(\mathbf{k}_{1,2})$ can be reduced to a limited amount of products and sums, which digital signal processors can easily handle within milliseconds. An online correction should therefore be feasible within a time window of about 100 ms.

Performance on Experimental Data

The lattice analysis methods derived and discussed in this chapter are put to a test by investigating three exemplary sets of scanning electron microscopy images. In the third example the electron beam was deliberately defocused to determine the reliability of the correction process. Each set consists of 30-50 images from an optical lattice with $d = 600$ nm spacing. A single image contains about 200-300 detected ions. The size of each

Phase correction of SEM imaged optical lattices:



Polar histograms of phases:

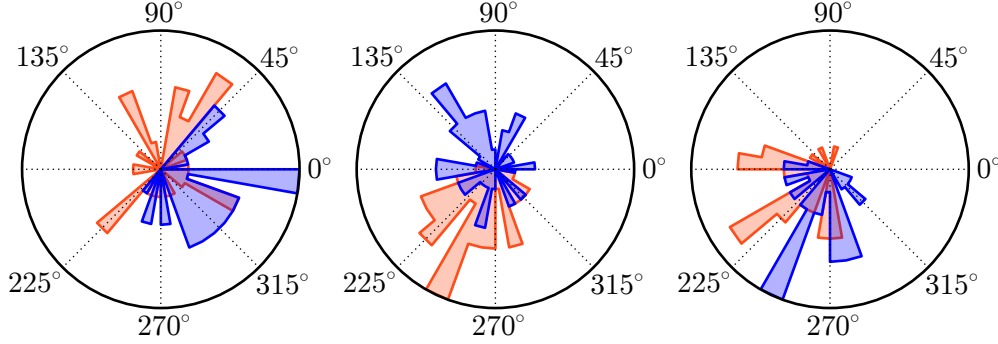


Figure 4.7: Phase correction of optical lattice scans. The exemplary datasets contain 30-50 single images each. In the third example the electron beam has been defocused. In the upper half of the figure the difference between uncorrected and corrected accumulation of the images is shown. The polar histograms in the lower half indicate the phase stability of the two lattice axes (red/blue). Axes that are washed out in the uncorrected image sum show a wider spread of phases, which is best seen in the second dataset.

	$ \hat{f}(\mathbf{k}_{1,2}) $ (mean)	$\max \hat{f}(\mathbf{k}) $ (mean)	$ \hat{f} $ corr. image
dataset 1	0.427, 0.377	0.436, 0.388	0.427, 0.376
dataset 2	0.510, 0.330	0.513, 0.336	0.504, 0.316
dataset 3	0.312, 0.198	0.322, 0.208	0.227, 0.144

Table 4.1: Fourier amplitudes of the datasets for both axes. The first column shows the mean of the single image amplitudes. In the second column the amplitudes were maximized by varying $\mathbf{k}_{1,2}$ for each single image. Periodicity and angle of the lattice structure appear to be stable throughout the measurements, since no significant increase in amplitude is found when using the second method. The last column contains the Fourier amplitude of the phase corrected image.

pixel corresponds to an area of $50 \times 50 \text{ nm}^2$. Since the exact position of the lattice sites varies from shot to shot a simple accumulation of the data results in a blurred image. A comparison of the uncorrected and corrected image sums for the three datasets is shown in Figure 4.7. The phase analysis and correction method reliably restores the visibility of the single lattice sites. In the lower part of the figure the histograms of the phase distributions are shown for each dataset. A wider spread of phases indicates a strong blurring of the uncorrected image along the corresponding axis. This effect is strongly pronounced in the second dataset, where only the vertical lattice is visible without corrections.

Another information that can be extracted from the images is the quality of quantifying the lattice visibility using the Fourier amplitude under experimental conditions. After the successful determination of the wave vectors $\mathbf{k}_{1,2}$ for a dataset the Fourier amplitudes $|f(\mathbf{k}_{(1,2)})|$ can be calculated and compared. Table 4.1 shows the mean of the single images' amplitudes for the two axes, as well as the corresponding amplitude found for the corrected sum of images. In two of the three examples, the correction method was able to restore the full amplitude of the periodic structure when calculating the image sum. Since the error in determining and therefore correcting the phases increases as the visibility decreases, the same performance is not achieved for the defocused images.

The highest Fourier amplitude is found in the second dataset. Since the experimental parameters, in particular the characteristics of the optical lattice, are matching the simulated mapping of Fourier amplitudes shown in Figure 4.6, we can determine an estimate for the electron beam width from the result. An amplitude of $|f| \approx 0.5$ corresponds to an electron beam with a FWHM of 200 nm or better. This is to be interpreted as an upper boundary for the beam width, as the simulation assumes an evenly distributed filling of lattice sites and does not take the blurring due to the ion time of flight into account.

Table 4.1 also includes the results of determining the amplitudes by varying \mathbf{k} and searching for a maximum of $|f(\mathbf{k})|$. No significant improvement is found when comparing these values with the amplitudes calculated for fixed positions $\mathbf{k}_{1,2}$. This implies that the angle and spacing of the lattice axes can be regarded as stable from shot to shot and that it is preferable to give up the computationally expensive optimization step.

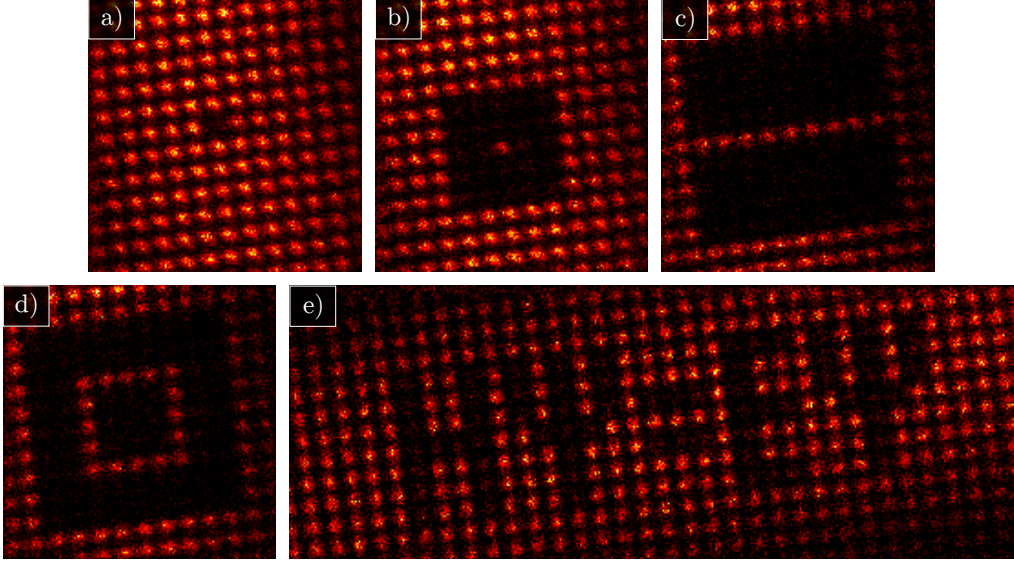


Figure 4.8: Examples of dissipative manipulation in a 2D optical lattice with a spacing of 600 nm. Every emptied site was illuminated with the electron beam for 3 ms (a, b), 2 ms (c, d) and 1.5 ms (e). The beam diameter was focused to 100 nm FWHM while providing a beam current of 7 nA. Between 150 and 250 images with a sampling time of 45 ms were accumulated for each pattern.

4.4 Addressing of Optical Lattices

The electron microscope is not only able to spatially resolve optical lattices at high contrast, it also allows for a selective removal of atoms from single lattice sites without affecting any of the neighboring cells. The ability of determining the exact position of a lattice within single images, which has been demonstrated by phase correcting the images in Figure 4.7, is an important prerequisite for the manipulation of these structures. This is achieved by moving the electron beam along arbitrary patterns prior to the imaging sequence and thus removing trapped atoms in the process. For typical experimental parameters, a dwell time of 1 – 3 ms per site is sufficient for a complete depletion.

Using the same experimental setup as before, the sites of a prepare optical lattice were selectively addressed by the electron beam prior to the imaging sequence [70]. Four elementary examples of this patterning technique are presented in Figure 4.8. A single defect in the lattice structure is shown in Figure 4.8a. The structure resembles a Schottky defect in a solid and is an ideal starting point to study the tunneling dynamics close

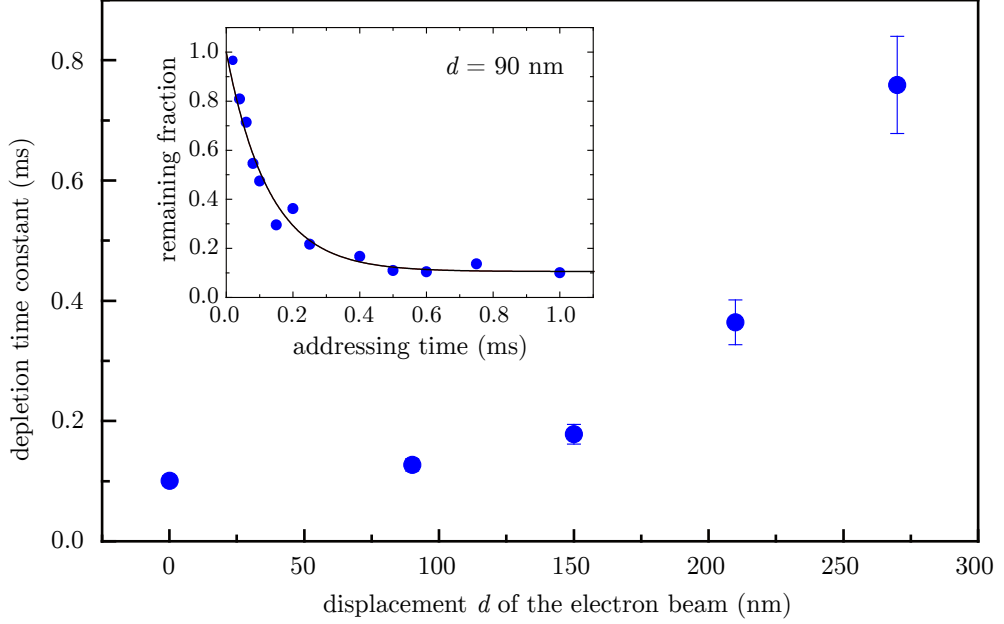


Figure 4.9: Depletion time constant for varying distance of the electron beam and the center of a lattice site. At all distances an exponential decay is observed. For central hits, the population decays with a time constant of $100\mu\text{s}$. The inset shows the depletion at a distance of 90 nm . The solid line is a fit with an exponential decay. The offset of 10% is caused by atoms that are refilling the lattice site between the end of the preparation process and the instant of imaging.

to a defect. The opposite situation corresponds to an isolated lattice site and is shown in Figure 4.8b. Such a mesoscopic ensemble provides, for instance, the possibility to study the transition from few-body systems to the thermodynamic limit. It can also act as a paradigm for Rydberg blockade studies as the spatial extension of the ensemble is very small. In this context, quantum optical applications such as single atom and single photon sources or the creation of Greenberger-Horne-Zeilinger-like states have been proposed [73]. A chain and a ring of lattice sites are shown in Figure 4.8c and Figure 4.8d in order to illustrate the large variety of achievable geometries. Obviously, this approach allows for any arbitrary pattern that fits to the underlying quadratic lattice geometry Figure 4.8e.

As for the plain optical lattice scans shown in Figure 4.7, preparation and imaging of dissipatively manipulated lattice structures are affected by shot to shot or long term drifts of the system. However, with the preparation procedure depending on the exact position of the lattice the situation is

more involved. A motion of the optical lattice leads to an error in the addressing protocol that cannot be corrected in a postprocess. This is the case, for instance, if the electron beam points in between two sites and depletes two instead of a single targeted site. Because of the high spatial resolution, the addressing procedure even works for some error in the relative positioning. For Figure 4.8, the lattice phases ϕ of the single images were determined and only those within an interval of $\pm\pi/2$ were accepted, where $\phi = 0$ corresponds to the optimal alignment of the electron beam and the lattice. A phase of π corresponds to the extreme case where the electron beam is maximally misplaced and points in between two sites. With this acceptance interval, about 65% of the images are typically discarded. With the development of an online correction method the loss of this data could be avoided. In such a procedure, the lattice position must be determined and the beam repositioned in real-time, prior to the manipulation and imaging sequence. Alternatively, the position of a preparation pattern could be adjusted in advance by extrapolating long term drifts based on previous realizations. This solution does not require any modification of the experimental setup, but it clearly cannot eliminate shot to shot fluctuations.

Imperfect addressing also leads to longer depletion times. This is best observed when classifying experimental realizations by the displacement of the electron beam with respect to the actual lattice position [70]. The dependence of the depletion time constant on the displacement is shown in Figure 4.9. Whereas for central hits a time constant of 100 μs is found, the timescale is more than 10 times larger if the electron beam points at the edge of a site. For all distances an exponential decay of the atom number is observed. When correctly addressed and hit in the center, a lattice site can be emptied in about 1 ms. Therefore, a preparation time of 100 ms is required for emptying a total of 100 sites, which is sufficient for tailoring a large part of the gas.

The ability to remove atoms from specific locations is directly applicable for the study of quantum phases in optical lattices. In many cases, the temperature of the gas after loading in the lattice potential is too high to reach the ground state of the system and further cooling in the lattice is necessary. One possible cooling strategy relies on the spatial separation of the gas into regions of high and low entropy which are subsequently decoupled by a potential barrier from each other [74]. In contrast, this technique directly allows for the removal of atoms from regions with high entropy without the need for decoupling from the remaining system.

Theory of Coherence and Correlation

In the previous chapter the high spatial resolution of the scanning electron microscopy technique was demonstrated by imaging the density distribution of atomic samples. As for any other typical imaging application, a lot of effort is spent on the reduction of noise and thus improving the quality and information gained from an image. Noise may originate from various sources, like imperfections in experimental preparation, signal processing electronics or measurement instruments. But also the system being studied itself can contribute additional fluctuations. In this case, valuable information might be hidden within the noise, probably inaccessible for any other kind of measuring procedure.

Statistical analyses, correlation and interferometry experiments allow to expose these characteristics. Probably the most popular observation in this context is the bunching effect of photons. In the experiments of R. Hanbury Brown and R.Q. Twiss [75-77] it was shown that the detection statistics of single photons emitted from a chaotic light source exceed the expected spread of a random Poissonian process. It was the earliest and most representative measurement of second order correlations. By examining the bosonic bunching behavior they furthermore proved that certain characteristics of a light source, like the angular diameter of an observed star, could be derived merely from the detection statistics of spatial correlations.

In the following decades, the measurement of noise correlations became an important tool for experimentalists. Correlation statistics have been

measured in cold atom systems by direct particle detection after time of flight. In such experiments the bunching effect of Bosons [17] and the anti-bunching nature of Fermions [18] were observed. Information about the spatial order of atoms in optical lattices was obtained by examining density correlations in absorption images after time of flight [19].

The scanning electron microscope provides the means for measuring the *temporal* density correlations in cold Bose gases. It allowed the observation of the time dependent bosonic bunching effect in thermal ensembles as well as its absence in Bose-Einstein condensates [78]. In the context of this work, these measurements will be discussed in detail. Strong emphasis will be given on the role of the temporal second order correlation function $g^{(2)}(\tau)$. When investigating the ion counting statistics from continuous electron beam illumination, $g^{(2)}(\tau)$ represents the conditional likelihood of detecting a particle a time τ after a previously detected particle. For a coherent source it is expected that $g^{(2)}(\tau)$ equals one for all times τ . A measurement where $g^{(2)}(\tau)$ is greater than one indicates a bunching of detection events and can be used for characterizing thermal bosonic sources.

Before investigating the measurements, an overview of the theoretical framework of coherence and correlation shall be given by this chapter. We will first recapitulate the role of first and second order coherence in classical wave mechanics and their relation to correlation functions [79]. This introduction is then followed by a quantum mechanical definition of coherence that has been developed by Naraschewski and Glauber [80]. On this basis we derive the spatio-temporal correlation function of trapped Bose gases and discuss typical experimental influences in its measurement. The chapter concludes with an statistical interpretation of the correlation measurement process.

5.1 First Order Correlations

In classical wave mechanics, coherence is a property of light that determines its ability of forming interference pattern. This effect is typically observed in optical interferometers. After splitting a coherent electromagnetic wave into two parts, an interference pattern can be seen when the separated waves are recombined. Typical setups that demonstrate this effect are the Michelson and Mach-Zehnder interferometers. In these experiments an incoming beam of light is equally divided by a beam splitter. Both beams propagate along separate paths before being recombined at

the point of observation. The superposition of the wave amplitudes can be written as $\mathbf{E}(t) + \mathbf{E}(t + \tau)$, where an additional delay of τ accounts for differences in the optical lengths of the paths. For an observer however it is usually easier to measure the intensity $I(t)$, which is the absolute square of the amplitude $\mathbf{E}(t) + \mathbf{E}(t + \tau)$

$$\begin{aligned} I(t) &= (\mathbf{E}^*(t) + \mathbf{E}^*(t + \tau)) \cdot (\mathbf{E}(t) + \mathbf{E}(t + \tau)) \\ &= I(t) + I(t + \tau) + 2 \cdot \text{Re} [\mathbf{E}^*(t) \mathbf{E}(t + \tau)] . \end{aligned} \quad (5.1)$$

The measurement itself is understood as an average of a function $f(t)$ over a fixed interval of time T and can be defined as $\langle f(t) \rangle = \frac{1}{T} \int_t^{t+T} f(t') dt'$. The measured intensity then reads

$$\langle I(t) \rangle = \langle I(t) \rangle + \langle I(t + \tau) \rangle + 2 \cdot \text{Re} [\langle \mathbf{E}^*(t) \mathbf{E}(t + \tau) \rangle] . \quad (5.2)$$

From equation (5.2) it is apparent that the total intensity is not simply the sum of the two individual waves' intensities. The observed intensity is furthermore influenced by an additional interference term that depends on the the phase relation of the light waves. The expectation value $\langle \mathbf{E}^*(t) \mathbf{E}(t + \tau) \rangle$ therein can be interpreted as the correlation of the field's amplitudes at times t and $t + \tau$. While this value is perfectly defined for an ideal monochromatic wave, the expectation value and the interference vanish for an incoherent superposition of chaotic light. The correlation of the field's amplitudes is expressed by the first order correlation function $G^{(1)}$ which thus quantifies the coherence of the light. In a generalized definition, $G^{(1)}$ is a measure of correlation for a field's amplitude at two different positions and two different times [79]

$$G^{(1)}(\mathbf{r}_1, t_1, \mathbf{r}_2, t_2) = \langle \mathbf{E}^*(\mathbf{r}_1, t_1) \mathbf{E}(\mathbf{r}_2, t_2) \rangle . \quad (5.3)$$

The normalized $g^{(1)}$ function is obtained by dividing $G^{(1)}$ by the mean expectation values of the two amplitudes. It is therefore independent from the absolute light intensities and provides a more convenient and comparable measure of coherence

$$g^{(1)}(\mathbf{r}_1, t_1, \mathbf{r}_2, t_2) = \frac{\langle \mathbf{E}^*(\mathbf{r}_1, t_1) \mathbf{E}(\mathbf{r}_2, t_2) \rangle}{\sqrt{\langle |\mathbf{E}(\mathbf{r}_1, t_1)|^2 \rangle \langle |\mathbf{E}(\mathbf{r}_2, t_2)|^2 \rangle}} . \quad (5.4)$$

5.2 Second Order Correlations

In analogy to the amplitude correlation function $g^{(1)}$, a second order correlation function $g^{(2)}$ is defined which serves as a measure of correlation in intensity. The $G^{(2)}$ correlation function and its normalized variant $g^{(2)}$ read

$$G^{(2)}(\mathbf{r}_1, t_1, \mathbf{r}_2, t_2) = \langle I(\mathbf{r}_1, t_1) I(\mathbf{r}_2, t_2) \rangle, \quad (5.5)$$

$$g^{(2)}(\mathbf{r}_1, t_1, \mathbf{r}_2, t_2) = \frac{\langle I(\mathbf{r}_1, t_1) I(\mathbf{r}_2, t_2) \rangle}{\langle I(\mathbf{r}_1, t_1) \rangle \langle I(\mathbf{r}_2, t_2) \rangle}. \quad (5.6)$$

In most cases the emission of light is a stationary process. If the characteristics of an emitter are independent of absolute times, it is reasonable to reduce the temporal $G^{(2)}(t_1, t_2)$ correlation function to a form that depends on the time differences τ only. Averaging over all absolute times is achieved by substituting $t_1 = t$, $t_2 = t + \tau$ and integrating over time

$$G^{(2)}(\tau) = \frac{1}{T} \int_0^T I(t) \cdot I(t + \tau) dt. \quad (5.7)$$

The equation shows that the second order correlation function of time differences $G^{(2)}(\tau)$ is simply the convolution of the signal $I(t)$ with itself, also known as the autocorrelation of $I(t)$. An efficient way of evaluating the autocorrelation function of a signal is to first determine its power spectral density $P(\nu)$. The autocorrelation function can then be obtained from the inverse Fourier transform of $P(\nu)$. The power spectrum is given by the absolute square of the Fourier transformed signal

$$P(\nu) = \left| \mathcal{F}[I(t)] \right|^2 \quad (5.8)$$

$$G^{(2)}(\tau) = \mathcal{F}^{-1}[P(\nu)]. \quad (5.9)$$

This relation is known as the Wiener-Khinchin theorem and illustrates the fact that the temporal correlation function is completely determined by the emission spectrum $P(\nu)$ of the light source. The measurement of $g^{(2)}$ thus includes the information of physical processes that affect how the frequency spectrum of an emitter is distributed. Examples for different types of classical light sources are shown in Figure 5.1. For chaotic sources of light a decrease of the $g^{(2)}$ amplitude from two to one is expected [79]. The emitters can be classified by the behavior of this decay. While the $g^{(2)}(\tau)$ function of a collision broadened emitter follows a Lorentz distribution, a Doppler broadened source shows a Gaussian shaped correlation

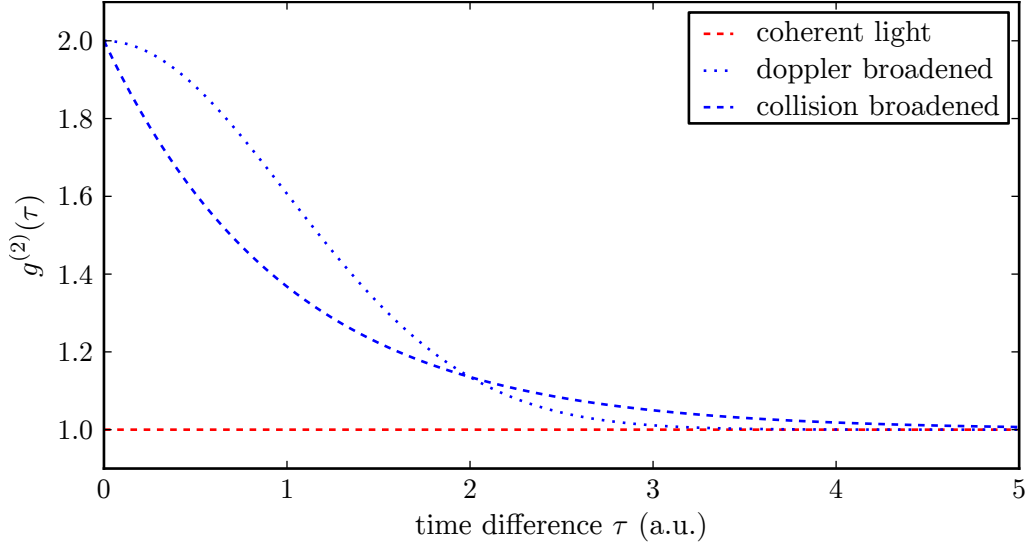


Figure 5.1: Temporal first order correlation function of various classical light sources. In contrast to the chaotic light sources (blue), $g^{(2)}$ equals one for a coherent light waves, regardless of the time distance (dashed red). The $g^{(2)}$ signal for a collision broadened chaotic light source follows the Lorentz distribution (dotted blue). A Doppler broadened source is characterized by a Gaussian correlation function (dashed blue).

function. The timescale of the temporal correlation corresponds to the width of the frequency spectrum. If the power spectral density is peaked at a single frequency only, which is the case for an ideal monochromatic laser, the $g^{(2)}(\tau)$ function in the time domain is simply a constant and equals one for all τ .

5.3 Second Quantization

So far, the theory of optical coherence and intensity correlation could be fully described by classical wave mechanics. With the advent of ultracold atom experiments and the realization of a BEC, the dualism of waves and particles was first made visible on a macroscopic scale. In the context of atom optics, the theory of coherence was extended to a formalism for particle correlations which allowed to create a description specifically for the field of trapped dilute Bose gases [80].

When applying second quantization, a particle can be described by the

field operators $\psi(\mathbf{r}, t)$ which obey the equal-time commutation relations

$$[\psi(\mathbf{r}, t), \psi^\dagger(\mathbf{r}', t)] = \delta(\mathbf{r} - \mathbf{r}'), \quad (5.10)$$

$$[\psi(\mathbf{r}, t), \psi(\mathbf{r}', t)] = 0. \quad (5.11)$$

A successive measurement or removal of n particles from a field at certain positions and times can be interpreted as an application of annihilation operators $\psi(\mathbf{r}, t)$ on an initial state $|\phi_I\rangle$ and leaving the system in the measured state $|\phi_M\rangle$

$$|\phi_M\rangle = \psi(\mathbf{r}_n, t_n) \cdots \psi(\mathbf{r}_2, t_2) \psi(\mathbf{r}_1, t_1) |\phi_I\rangle. \quad (5.12)$$

Correlation can be understood as the likelihood of finding the particles at these exact locations. The probability of this outcome is given by the absolute square of the measured state

$$|\phi_M|^2 = \langle \phi_I | \psi^\dagger(\mathbf{r}_1, t_1) \psi^\dagger(\mathbf{r}_2, t_2) \cdots \psi(\mathbf{r}_2, t_2) \psi(\mathbf{r}_1, t_1) | \phi_I \rangle. \quad (5.13)$$

Equation (5.13) has the form of an expectation value and is already a specific representation of the non-normalized n -th order density correlation function $G^{(n)}$. Dropping the prerequisite of having a system in a single state and allowing the evaluation of the expectation value for statistical mixtures of states, we obtain a more general definition of $G^{(n)}$

$$G^{(n)} = \langle \psi^\dagger(\mathbf{r}_1, t_1) \psi^\dagger(\mathbf{r}_2, t_2) \cdots \psi(\mathbf{r}_2, t_2) \psi(\mathbf{r}_1, t_1) \rangle. \quad (5.14)$$

In analogy to the classical formalism we can define a normalization for the correlation functions in order to provide a more convenient measure of coherence

$$g^{(n)} = \frac{\langle \psi_1^\dagger \psi_2^\dagger \cdots \psi_2 \psi_1 \rangle}{\langle \psi_1^\dagger \psi_1 \rangle \cdots \langle \psi_n^\dagger \psi_n \rangle}, \quad (5.15)$$

where ψ_i is an abbreviation for $\psi(\mathbf{r}_i, t_i)$. The normalized correlation functions $g^{(n)}$ thus do not depend on the mean probabilities $\langle \psi_i^\dagger \psi_i \rangle$ of detecting a particle any more. An exception to this scheme is the first order correlation function $G^{(1)}$, which is not a density correlation function but a correlation of a field's amplitude

$$G^{(1)}(\mathbf{r}_1, \mathbf{r}_2, t_1, t_2) = \langle \psi^\dagger(\mathbf{r}_1, t_1) \psi(\mathbf{r}_2, t_2) \rangle \quad (5.16)$$

$$g^{(1)}(\mathbf{r}_1, \mathbf{r}_2, t_1, t_2) = \frac{\langle \psi^\dagger(\mathbf{r}_1, t_1) \psi(\mathbf{r}_2, t_2) \rangle}{\sqrt{\langle \psi^\dagger(\mathbf{r}_1, t_1) \psi(\mathbf{r}_1, t_1) \rangle} \sqrt{\langle \psi^\dagger(\mathbf{r}_2, t_2) \psi(\mathbf{r}_2, t_2) \rangle}}. \quad (5.17)$$

In contrast to the higher density correlation functions $G^{(n)}$, $G^{(1)}$ is a non hermite expectation value and therefore neither real valued nor measurable directly.

5.4 Thermal First Order Correlation Function

Since the focus of the experiments presented in the next chapter lies on the measurement of temporal correlations in cold Bose gases, we require a spatio-temporal description of the correlation theory introduced by Naraschewski and Glauber [80]. To this end, the first order correlation function presented in their publication is extended by a time dependency. In analogy to their derivation, the system is assumed to reside in a three dimensional harmonic oscillator.

To indicate the approach to the time dependent correlation function, an exemplary ansatz is given for a one dimensional harmonic oscillator. For this system, the wave functions $u_n(x)$ solving the stationary Schrödinger equation [24] are multiplied by the time evolution. Each state oscillates with its corresponding energy of E_n . The functions read

$$\begin{aligned} u_n(x, t) &= u_n(x) \exp\left(-\frac{iE_n}{\hbar}t\right) \\ &= \left(\frac{1}{\sqrt{2^n n!}}\right) \left(\frac{m\omega}{\pi\hbar}\right)^{1/4} \exp\left(-\frac{m\omega x^2}{2\hbar}\right) \\ &\quad \times H_n\left(\sqrt{\frac{m\omega}{\hbar}}x\right) \exp\left(-i\omega\left(n + \frac{1}{2}\right)t\right), \end{aligned} \quad (5.18)$$

with the Hermite polynomials denoted by $H_n(x)$. In the same manner, the solutions for the three dimensional isotropic harmonic oscillator $u_n(\mathbf{r})$ are evolved to $u_n(\mathbf{r}, t)$.

The harmonic oscillator solutions $u_n(\mathbf{r}, t)$ will serve as the basis for the spatially dependent field operators $\psi(\mathbf{r}, t)$ in second quantization

$$\psi(\mathbf{r}, t) = \sum_m u_m(\mathbf{r}, t) \hat{a}_m. \quad (5.19)$$

The operators \hat{a}_m^\dagger and \hat{a}_m respectively create and annihilate a particle in the harmonic oscillator state m . For a system in a thermal equilibrium we evaluate the non-normalized first order correlation function $G^{(1)}$ from equation (5.16)

$$G^{(1)}(\mathbf{r}_1, \mathbf{r}_2, \tau) = \langle \psi^\dagger(\mathbf{r}_1, 0) \psi(\mathbf{r}_2, \tau) \rangle_0, \quad (5.20)$$

where $\langle \dots \rangle_0$ denotes the thermal expectation value. As we will look into stationary systems only, a single relative time parameter τ is used instead

of introducing two absolute times t and t' . Using (5.19) we then obtain

$$\begin{aligned} G^{(1)}(\mathbf{r}_1, \mathbf{r}_2, \tau) &= \sum_{m,n} u_m^*(\mathbf{r}_1, 0) u_n(\mathbf{r}_2, \tau) \langle \hat{a}_m^\dagger \hat{a}_n \rangle_0 \\ &= \sum_m u_m^*(\mathbf{r}_1, 0) u_m(\mathbf{r}_2, \tau) \langle \hat{a}_m^\dagger \hat{a}_m \rangle_0. \end{aligned} \quad (5.21)$$

Due to the lack of coherence between the oscillator states in a thermal system, any non diagonal expectation value vanishes and thus $\langle \hat{a}_m^\dagger \hat{a}_n \rangle_0 = 0$ for $m \neq n$. This fact also follows from the generalized Wick theorem found in appendix A.2. In (5.21), the expectation value $\langle \hat{a}_m^\dagger \hat{a}_m \rangle_0$ describes the probability of a particle being in state m . In an ideal classical gas with a temperature of T all oscillator states are populated independently and the probabilities follow the Maxwell-Boltzmann distribution. Therefore, $G^{(1)}$ can be expressed as

$$\begin{aligned} G^{(1)}(\mathbf{r}_1, \mathbf{r}_2, \tau) &= \sum_m u_m^*(\mathbf{r}_1, 0) u_m(\mathbf{r}_2, \tau) \exp\left(-\frac{E_m}{k_B T}\right) \\ &= \sum_m u_m^*(\mathbf{r}_1, 0) u_m(\mathbf{r}_2, 0) \exp\left(-\frac{iE_m \tau}{\hbar}\right) \exp\left(-\frac{E_m}{k_B T}\right) \\ &= \sum_m u_m^*(\mathbf{r}_1, 0) \exp\left(-\frac{iE_m}{\hbar} \left(\tau - i\frac{\hbar}{k_B T}\right)\right) u_m(\mathbf{r}_2, 0) \\ &= K\left(\mathbf{r}_1, 0; \mathbf{r}_2, t = \tau - i\frac{\hbar}{k_B T}\right). \end{aligned} \quad (5.22)$$

The third expression in equation (5.22) is replaced by the propagator K

$$K(\mathbf{r}_1, 0; \mathbf{r}_2, t) = \langle \Psi(\mathbf{r}_1, 0) | \hat{U}(t) | \Psi(\mathbf{r}_2, 0) \rangle, \quad (5.23)$$

interpreting the exponential function in the center as a time evolution with a partially complex time argument. The analytic form of this propagator is given in [80] and reads

$$\begin{aligned} K(\mathbf{r}_1, 0; \mathbf{r}_2, t) &= \left(\frac{m\omega}{\pi\hbar(1 - e^{-2t\omega})} \right)^{3/2} \\ &\times \exp\left(\frac{-m\omega}{\hbar} \frac{(r_1^2 + r_2^2)(\cosh \omega t - 1) + (\mathbf{r}_1 - \mathbf{r}_2)^2}{2 \sinh \omega t} \right). \end{aligned} \quad (5.24)$$

A considerable simplification can be achieved if the energies of the trap levels are much smaller than the thermal energy, thus $\frac{\hbar\omega}{k_B T} \ll 1$. Also, the observed time differences are considered to be small $\omega\tau \ll 1$. The approximations are justified by quite general experimental conditions of ultracold atom experiments. Using a linear approximation for small t simplifies the equation and eliminates the factor $(\cosh \omega t - 1) \approx 0$ in the process. As a result, the dependence on absolute distances from the trap center vanishes, leaving only the spatial difference $\Delta r^2 = (\mathbf{r}_1 - \mathbf{r}_2)^2$ by which K may be expressed

$$G^{(1)}(\Delta r, \tau) = K(\Delta r, t = \tau - i\tau_c) \\ = \left(\frac{m}{2\pi\hbar(\tau - i\tau_c)} \right)^{3/2} \exp \left(-\frac{m\Delta r^2}{2\hbar} \frac{1}{\tau - i\tau_c} \right). \quad (5.25)$$

For convenience a characteristic correlation time τ_c is introduced and shall be defined as $\tau_c = \hbar/k_B T$. After normalizing the first order correlation function $G^{(1)}$ by the amplitude $G^{(1)}(0, 0)$ the correlation function $g^{(1)}$ is obtained

$$g^{(1)}(\Delta r, \tau) = \left(\frac{1}{1 + i\frac{\tau}{\tau_c}} \right)^{3/2} \exp \left(-\frac{m\Delta r^2}{2\hbar} \frac{\tau_c + i\tau}{\tau^2 + \tau_c^2} \right). \quad (5.26)$$

5.5 Higher Order Correlation Functions

Although the $G^{(1)}$ correlation function that has been derived cannot be measured directly, it fully characterizes the behavior of density correlations in temporal and spatial dependence in an ideal thermal gas. In fact, for systems in thermal equilibrium any higher order correlation function can be expressed as a function of first order correlations.

The n -th order correlation function $G^{(n)}$ is an expectation value of a product of field operators. For a gas of atoms in thermal equilibrium it is evaluated by the thermal average

$$\langle \psi_1^\dagger \psi_2^\dagger \cdots \psi_2 \psi_1 \rangle_0 \equiv \frac{\text{Tr} [\psi_1^\dagger \psi_2^\dagger \cdots \psi_2 \psi_1 \cdot \rho]}{\text{Tr} [\rho]}, \quad (5.27)$$

where ρ is the density matrix of the system. The generalized Wick theorem provides a method of transforming such a thermal average into a series of two-operator expectation values. A description of the theorem is found in appendix A.2.

Consequently, the second order correlation function $G^{(2)}$ for particles detected at positions *one* and *two* can be rewritten to

$$\begin{aligned} G^{(2)} &= \langle \psi_1^\dagger \psi_2^\dagger \psi_2 \psi_1 \rangle_0 = \langle \psi_1^\dagger \psi_2^\dagger \rangle_0 \langle \psi_2 \psi_1 \rangle_0 + \\ &\quad \langle \psi_1^\dagger \psi_2 \rangle_0 \langle \psi_2^\dagger \psi_1 \rangle_0 + \\ &\quad \langle \psi_1^\dagger \psi_1 \rangle_0 \langle \psi_2^\dagger \psi_2 \rangle_0 \end{aligned} \quad (5.28)$$

$$= 0 + |\langle \psi_1^\dagger \psi_2 \rangle_0|^2 + \langle \psi_1^\dagger \psi_1 \rangle_0 \langle \psi_2^\dagger \psi_2 \rangle_0 \quad (5.29)$$

$$= |G^{(1)}(\Delta r, \tau)|^2 + |G^{(1)}(0, 0)|^2. \quad (5.30)$$

As stated in appendix A.2, the thermal averages of two creation or annihilation operators evaluate to zero and the first term in equation (5.28) vanishes. After the normalization of $G^{(2)}$ by $|G^{(1)}(0, 0)|^2$, we obtain the second order correlation function $g^{(2)}$ for a thermal gas

$$g^{(2)}(\Delta r, \tau) = 1 + |g^{(1)}(\Delta r, \tau)|^2. \quad (5.31)$$

This result is well known from classical definition of the intensity correlation function [79]. The evaluation of $g^{(2)}$ for the thermal first order correlation function derived in equation (5.26) yields

$$g^{(2)}(\Delta r, \tau) = 1 + \left(\frac{1}{1 + (\tau/\tau_c)^2} \right)^{3/2} \exp \left(-\frac{m}{2\hbar\tau_c} \frac{\Delta r^2}{1 + (\tau/\tau_c)^2} \right). \quad (5.32)$$

Also the third order correlation function $G^{(3)}$ can be calculated in the same manner. This function now involves the fields of three individual particles ψ_1 , ψ_2 and ψ_3 and is again expressed as a function of first order correlations

$$\begin{aligned} G^{(3)} &= G_{11}^{(1)} G_{22}^{(1)} G_{33}^{(1)} + G_{11}^{(1)} |G_{23}^{(1)}|^2 + G_{22}^{(1)} |G_{13}^{(1)}|^2 \\ &\quad + G_{33}^{(1)} |G_{12}^{(1)}|^2 + 2 \operatorname{Re}[G_{21}^{(1)} G_{32}^{(1)} G_{13}^{(1)}], \end{aligned} \quad (5.33)$$

where $G_{ij}^{(1)}$ is an abbreviation for $G^{(1)}(|\mathbf{r}_i - \mathbf{r}_j|, |t_i - t_j|)$. The normalized $g^{(3)}$ correlation function is obtained after dividing by $G_{11} G_{22} G_{33}$

$$g^{(3)} = 1 + |g_{12}^{(1)}|^2 + |g_{23}^{(1)}|^2 + |g_{13}^{(1)}|^2 + 2 \operatorname{Re}[g_{12}^{(1)} g_{13}^{(1)} g_{23}^{(1)}], \quad (5.34)$$

where $g_{ij}^{(1)}$ is again an abbreviation for the $g^{(1)}(|\mathbf{r}_i - \mathbf{r}_j|, |t_i - t_j|)$ correlation between the particles i and j .

5.6 Spatial Average of Correlations

Up to this point, the theory describes the correlation of particles whose positions are known with infinite accuracy. In real world experiments however this precondition is never fulfilled. Moreover, the experimental setup this work is based on only allows for back-tracing a detected particle onto an xy -plane, leaving no knowledge about its position in the z -direction. A correlation measurement is thus seen as an average over all point-to-point correlations within the volume of possible detection events. It is defined by the extension of the electron beam and the thickness of the atomic sample.

In order to reflect this aspect in the theoretical description of the second order correlation function, which is the main subject of discussion in the next chapter, $g^{(2)}(\Delta r, \tau)$ is spatially integrated over the detection volume. Generally, the measured $\tilde{g}^{(2)}(\tau)$ function is obtained by evaluating the double spatial integral

$$\tilde{g}^{(2)}(\tau) = \iint p(\mathbf{r}_1) \cdot g^{(2)}(|\mathbf{r}_1 - \mathbf{r}_2|, \tau) \cdot p(\mathbf{r}_2) \, d^3r_1 d^3r_2. \quad (5.35)$$

The normalized density function $p(\mathbf{r})$ describes the probability of finding a single particle at position \mathbf{r} . When weighting the correlation amplitude $g^{(2)}(|\mathbf{r}_1 - \mathbf{r}_2|, \tau)$ of two particles at positions $\mathbf{r}_{1,2}$ with their joint detection probability $p(\mathbf{r}_1) \cdot p(\mathbf{r}_2)$, the expected temporal correlation signal $\tilde{g}^{(2)}(\tau)$ can be interpreted as an average over many two-particle detection events. For the purpose of modeling a distribution that approximates the detection volume of the experimental setup this work is based on, a cylindrical symmetric Gaussian probability function shall be assumed

$$p(\mathbf{r}) = \frac{w_{xy}\sqrt{w_z}}{\pi^{3/2}} \cdot \exp\left(-w_{xy}x^2 - w_{xy}y^2 - w_zz^2\right), \quad (5.36)$$

with the two parameters $w_{xy} = \frac{1}{2\sigma_{xy}^2}$ and $w_z = \frac{1}{2\sigma_z^2}$ defining width and height of the distribution. The thermal correlation function $g^{(2)}(\Delta r, \tau)$ from equation (5.32) can be expressed in a simpler form

$$g^{(2)}(\Delta r, \tau) = 1 + A(\tau) \cdot \exp\left(-w_c(\tau) \Delta x^2 - w_c(\tau) \Delta y^2 - w_c(\tau) \Delta z^2\right) \quad (5.37)$$

by introducing the substitutions

$$w_c(\tau) = \frac{m}{\hbar\tau_c} \frac{1}{1 + (\tau/\tau_c)^2} \quad \text{and} \quad A(\tau) = \left(\frac{1}{1 + (\tau/\tau_c)^2}\right)^{3/2}. \quad (5.38)$$

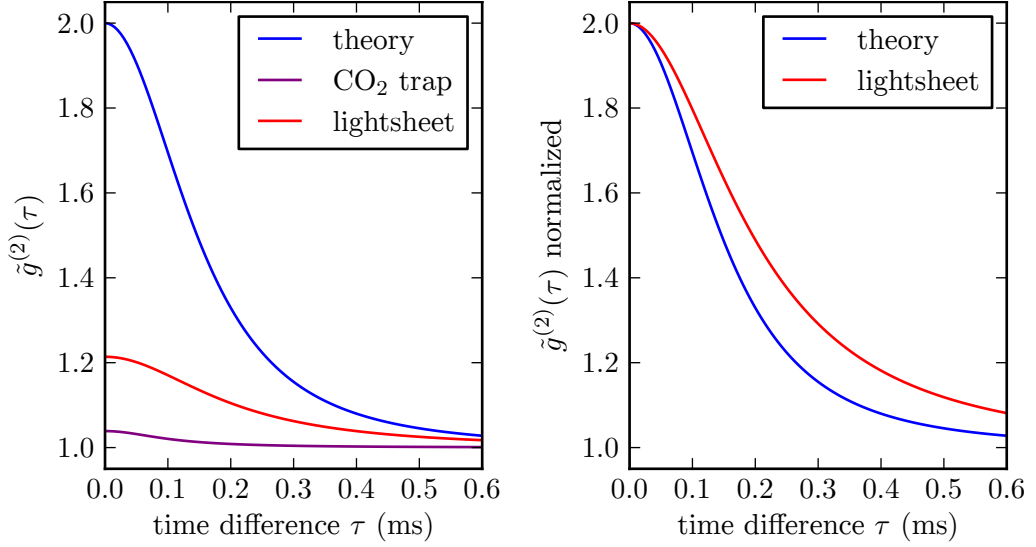


Figure 5.2: Spatial averaging effects when measuring the temporal second order correlation function. The blue curves shows the $g^{(2)}$ function for a temperature of 40 nK without spatial averaging. The purple curve on the left shows the spatially averaged $\tilde{g}^{(2)}$ for the CO_2 dipole trap, which has a vertical trap frequency of $\omega_z = 2\pi \cdot 160\text{ Hz}$ when holding a thermal gas at 80 nK . The red curve on the left simulates the expectation for a thermal gas of 40 nK held in the lightsheet trap with a trap frequency of $\omega_z = 2\pi \cdot 410\text{ Hz}$. On the right, the lightsheet curve has been scaled to the maximum amplitude to demonstrate the influence of the spatial average on the timescale of the signal.

A solution for $\tilde{g}^{(2)}$ is found by solving three Gaussian integrals of the type

$$\iint e^{-w_1 x_1^2 - w_2 x_2^2 - w_2 (x_1 - x_2)^2} dx_1 dx_2 = \frac{\pi}{\sqrt{w_1(w_1 + 2w_2)}} \quad (5.39)$$

for each dimension in equation (5.35). The spatially averaged temporal correlation function then reads

$$\tilde{g}^{(2)}(\tau) = 1 + A(\tau) \cdot \frac{w_{xy}}{w_{xy} + 2w_c(\tau)} \frac{\sqrt{w_z}}{\sqrt{w_z + 2w_c(\tau)}}. \quad (5.40)$$

The free parameters in this model are temperature T and the sigma widths of the detection volume $\sigma_{xy,z}$. From equation (5.40) it is apparent that the full amplitude of $\tilde{g}^{(2)}(0)$ is only achieved for $w_{xy,z} \gg 2w_c(0)$, so that $\sigma_{xy,z} \ll \sqrt{\frac{\hbar^2}{4mk_B T}}$ holds for the sigma widths of the Gaussian volume.

Experimentally, this criterion is quite difficult to reach. For a temperature of 40 nK the widths must be smaller than 186 nm. When probing a system using the scanning electron microscopy technique, the detection volume is defined by the overlap between the electron beam and the atomic sample. The focus of the beam in the xy -plane can be chosen as small as 120 nm (FWHM), which corresponds to $\sigma_{xy} = 51$ nm. Typically, the density of the atomic ensemble does not vary within this range when taking measurements at the center of the cloud. However, since the electron beam ionizes particles all along its path, the extent of the detection volume in the z -direction solely depends on the thickness of the atomic cloud. This size is generally in the order of micrometers and therefore a significant reduction in $\tilde{g}^{(2)}$ amplitude is expected. For a quantitative analysis, the cloud is approximated as a Boltzmann distributed thermal ensemble for which the Gaussian width σ_z is given by

$$\rho(z) \propto \exp\left(-\frac{m\omega_z^2}{2k_B T} z^2\right) \Rightarrow \sigma_z = \sqrt{\frac{k_B T}{m_{\text{Rb}} \omega_z^2}}, \quad (5.41)$$

with ω_z being the vertical harmonic trapping frequency.

Figure 5.2 shows the effects of the spatial averaging for different experimental parameters. In previous experiments the CO₂ dipole trap was able to evaporatively cool down a thermal gas to 80 nK before reaching the critical temperature and ending up with a non-thermal atomic ensemble. With a vertical trap frequency of $\omega_z = 2\pi \cdot 160$ Hz, the expected amplitude for a $g^{(2)}$ measurement is smaller than 4 %. The lightsheet dipole trap was specifically designed to provide a more suitable environment for such measurements. This trap allows for the preparation of a thermal cloud with a temperature of 40 nK in conjunction with a trap frequency of $\omega_z = 2\pi \cdot 410$ Hz. The expected $g^{(2)}$ amplitude for these parameters is 21 %. The second plot in the right half of Figure 5.2 visualizes an additional effect of spatial averaging. The ideal $g^{(2)}(\Delta r = 0, \tau)$ function is compared with an upscaled spatial average $\tilde{g}^{(2)}(\tau)$. An enlargement of the timescale in which the amplitude of the $\tilde{g}^{(2)}$ function drops can be observed. Although the temperature of the thermal cloud is fixed, the timescale grows as the volume of integration increases.

5.7 Statistical Interpretation of a Measurement Process

We introduced the second order correlation function $g^{(2)}$ in second quantization as a measure of coherence and as a way of characterizing an atomic ensemble. In the following we will discuss the measurement of the quantum mechanical expectation values therein in the context of a basic introduction in statistics. Experimentally, the expectation value of an operator expression can be approximated by averaging repeated measurements of the corresponding quantity. We represent such a measurable quantity by a random variable X and define

$$E[X] = \frac{1}{m} \sum_{i=1}^m x_i = \bar{x} \quad (5.42)$$

as the average of a number of m individual measurements x_i . The definition (5.42) is also known as the first statistical moment, which is a special case of the more generally defined k -th moment of a random variable

$$E[X^k] = \frac{1}{m} \sum_{i=1}^m x_i^k. \quad (5.43)$$

The statistics of the values x_i also include information about the fluctuation of the measurement. Although this information can be derived from the statistical moments $E[X^k]$, the spread of a measurement is more conveniently expressed by the *central* statistical moments $\mu_k(X)$. These depend on the distances ΔX from the mean value \bar{x} and are defined as

$$\mu_k(X) = E[\Delta X^k] = E[(X - \bar{x})^k] = \frac{1}{m} \sum_{i=1}^m (x_i - \bar{x})^k. \quad (5.44)$$

The second central moment $\mu_2(X)$ is of particular interest. It is also known as the variance σ^2 of a distribution and reads

$$\sigma^2 = \mu_2(X) = \frac{1}{m} \sum_{i=1}^m (x_i - \bar{x})^2 = E[X^2] - E[X]^2. \quad (5.45)$$

Generally, larger values of σ^2 imply an increased amount of fluctuation in a series of measurements x_i . For a joint measurement of two random variables X and Y we furthermore define the covariance

$$\begin{aligned} \sigma(X, Y) &= E[\Delta X \cdot \Delta Y] \\ &= E[(X - \bar{x})(Y - \bar{y})] = E[XY] - E[X]E[Y], \end{aligned} \quad (5.46)$$

which is a measure of correlation between the fluctuations of X and Y . A positive value of $\sigma(X, Y)$ indicates that if a single measurement x_i is larger (smaller) than its mean \bar{x} , y_i has the tendency to be larger (smaller) than \bar{y} as well. The opposite case where X and Y are anti-correlated is identified by negative values of $\sigma(X, Y)$. Two random variables are statistically independent or uncorrelated if $\sigma(X, Y) = 0$. The definition (5.46) can be rewritten to

$$E[X \cdot Y] = E[X] \cdot E[Y] + \sigma(X, Y) \quad (5.47)$$

and shows that an averaged product of random variables X and Y can be simplified to a product of their expectation values if they are statistically independent and their covariance vanishes.

Statistical Interpretation of $g^{(2)}$

We recall the definition of the density correlation functions $g^{(n)}$ from equation (5.15) and derive the second order correlation function $g^{(2)}$ for two field operators $\hat{\psi}_1$ and $\hat{\psi}_2$ at different times and positions

$$g^{(2)} = \frac{\langle \hat{\psi}_1^\dagger \hat{\psi}_2^\dagger \hat{\psi}_2 \hat{\psi}_1 \rangle}{\langle \hat{\psi}_1^\dagger \hat{\psi}_1 \rangle \langle \hat{\psi}_2^\dagger \hat{\psi}_2 \rangle}. \quad (5.48)$$

It is interpreted as the the expectation value of the joint probability for first finding one particle at position *one* and another particle at position *two* afterwards. If we were to measure the number of particles at these two positions and times in an experiment, the measurement process is represented by statistical random variables which shall be denoted by N_1 and N_2 . The normalized probability for detecting a single particle is then given by N_i/\bar{n}_i . In conclusion, the statistical expectation value of the joint probability for detecting two particles reads

$$g^{(2)} = E \left[\frac{N_1}{\bar{n}_1} \cdot \frac{N_2}{\bar{n}_2} \right] = \frac{E[N_1 N_2]}{\bar{n}_1 \bar{n}_2} = \frac{1}{\bar{n}_1 \bar{n}_2} \frac{1}{m} \sum_{i=1}^m n_{1_i} n_{2_i}. \quad (5.49)$$

Although it is tempting to identify the random variables N_i with the quantum mechanical density operators $\hat{n}_i = \hat{\psi}_i^\dagger \hat{\psi}_i$, a literal replacement of the expression $N_1 \cdot N_2 \rightarrow \hat{\psi}_1^\dagger \hat{\psi}_1 \hat{\psi}_2^\dagger \hat{\psi}_2$ generally does not lead to an observable quantity, as the product of operators on the right is not self-adjoint. It shall be emphasized that equation (5.49), which describes the evaluation of the measured data, is indeed the analogue of the quantum mechanical $g^{(2)}$ definition (5.48) without reordering the field operators in any way.

5. THEORY OF COHERENCE AND CORRELATION

By utilizing the definition from equation (5.47), a more descriptive representation of $g^{(2)}$ is obtained

$$g^{(2)} = \frac{E[N_1 N_2]}{\bar{n}_1 \bar{n}_2} = 1 + \frac{\sigma(N_1, N_2)}{\bar{n}_1 \bar{n}_2}. \quad (5.50)$$

It illustrates that the second order correlation function is simply a normalized expression for the covariance of two measured quantities. An uncorrelated pair of measurements N_1 and N_2 leads to $g^{(2)} = 1$, while larger or smaller values characterize a correlation or anti-correlation. A special case is the interpretation of $g^{(2)}(0)$ where the bosonic operators $\hat{\psi}_i$ are identical. Using the commutator relation $[\psi, \psi^\dagger] = 1$, $g^{(2)}(0)$ can be rewritten to

$$g^{(2)}(0) = \frac{\langle \hat{\psi}^\dagger \hat{\psi}^\dagger \hat{\psi} \hat{\psi} \rangle}{\langle \hat{\psi}^\dagger \hat{\psi} \rangle \langle \hat{\psi}^\dagger \hat{\psi} \rangle} = \frac{\langle \hat{\psi}^\dagger \hat{\psi} \hat{\psi}^\dagger \hat{\psi} \rangle - \langle \hat{\psi}^\dagger \hat{\psi} \rangle}{\langle \hat{\psi}^\dagger \hat{\psi} \rangle \langle \hat{\psi}^\dagger \hat{\psi} \rangle} \quad (5.51)$$

$$= \frac{E[N^2] - E[N]}{E[N]^2} = 1 + \frac{E[\Delta N^2] - n}{n^2} = 1 + \frac{\sigma^2 - n}{n^2}. \quad (5.52)$$

Instead of quantifying the correlation between two measurements N_1 and N_2 , the amplitude in $g^{(2)}(0)$ is a comparison of the variance $E[\Delta N^2]$ and the mean value $E[N]$ of only a single measurement process N . For a coherent state the number fluctuation $E[\Delta N^2]$ follows the Poisson distribution and is equal to $E[N]$, leading to the expected result of $g^{(2)}(0) = 1$. A super- or sub-Poissonian distribution with a variance larger or smaller than $E[N]$ characterizes a bunched or anti-bunched process. This interpretation is fundamentally different from the classical correlation function $g_C^{(2)}(0)$ for single observables

$$g_C^{(2)}(0) = \frac{E[N \cdot N]}{E[N] \cdot E[N]} = 1 + \frac{\sigma^2}{n^2}. \quad (5.53)$$

In classical wave mechanics, the description of a coherent wave does not include fluctuations. Ideally, the variance of an intensity measurement would vanish and thus lead to $g_C^{(2)}(0) = 1$. Equation (5.53) also shows that there is no classical concept of anti-bunching, as the variance σ^2 cannot be negative. We can account for the presence of additive noise by representing the measurement of N by $\tilde{N} = N + \Delta$. For simplicity it shall be assumed that the introduction of the random variable Δ does not affect the mean expectation $E[\tilde{N}] = E[N]$, so $E[\Delta] = 0$ must vanish. In this case, the noise affected $\tilde{g}_C^{(2)}(0)$ measurement reads

$$\tilde{g}_C^{(2)}(0) = \frac{E[\tilde{N}^2]}{E[\tilde{N}]^2} = \frac{E[N^2] + E[\Delta^2]}{E[N]^2} = g_C^{(2)}(0) + \frac{E[\Delta^2]}{n^2}. \quad (5.54)$$

If the characteristics of the detection noise are known, we can calculate the undisturbed $g_C^{(2)}(0)$ value of the observed system

$$g_C^{(2)}(0) = \tilde{g}_C^{(2)}(0) - \frac{E[\Delta^2]}{n^2} = 1 + \frac{\tilde{\sigma}^2 - E[\Delta^2]}{n^2}, \quad (5.55)$$

which equals the quantum mechanical interpretation of $g^{(2)}(0)$ if we assume that the noise of a stochastic measurement process follows the Poisson distribution with a variance of $E[\Delta^2] = n$.

5.8 Influence of Measurement Noise

Under realistic experimental conditions a measurement process is most likely affected by undesired influences, thus being subject to noise. Possible sources of noise in a setup for recording the counting statistics of particles include the presence of dark counts or fluctuations caused by the detection scheme itself. Due to the single atom sensitivity of the presented system however we do not expect a significant contribution from these effects. Nevertheless, it is important to understand how the evaluation of a correlation measurement is affected by noise.

As already shown, the influence of noise can be described by additional random variables. We can model the effects of additive and multiplicative fluctuations by respectively defining $\tilde{N} = N + \Delta$ and $\hat{N} = N \cdot F$. It is further assumed that the processes that are causing the noise are statistically independent from the measured quantity N , which implies that products like $E[N \cdot F] = E[N]E[F]$ are separable. The mean expectation value of a measurement $E[N]$ shall be unaffected by the noise and therefore requires $E[\Delta] = 0$ and $E[F] = 1$. It is thus sufficient to evaluate the non-normalized correlation functions

$$\begin{aligned} \tilde{G}^{(2)} &= E[\tilde{N}_1 \tilde{N}_2] = E[(N_1 + \Delta_1)(N_2 + \Delta_2)] \\ &= E[N_1 N_2] + E[\Delta_1]E[N_2] + E[\Delta_2]E[N_1] + E[\Delta_1]E[\Delta_2] \\ &= E[N_1 N_2] = G^{(2)} \end{aligned} \quad (5.56)$$

$$\begin{aligned} \hat{G}^{(2)} &= E[\hat{N}_1 \hat{N}_2] = E[N_1 F_1 \cdot N_2 F_2] \\ &= E[N_1 N_2]E[F_1]E[F_2] = E[N_1 N_2] = G^{(2)} \end{aligned} \quad (5.57)$$

In equations (5.56) and (5.57) it is assumed that there is no statistical dependence of noise between distinct measurement processes. This implies

that $E[\Delta_1\Delta_2]$ and $E[F_1F_2]$ are separable. A case where this assumption fails will be discussed in the evaluation of the correlation measurement results. However, if the assumption of statistical independence holds, the equations show that neither additive nor multiplicative noise affect the outcome of $g^{(2)}$. An exception to this result is the statistical evaluation of the single measurement process in $g^{(2)}(0)$

$$\begin{aligned}\tilde{G}_C^{(2)}(0) &= E[\tilde{N}^2] = E[N^2] + 2E[N]E[\Delta] + E[\Delta^2] = E[N^2] + E[\Delta^2] \\ &= G_C^{(2)}(0) + E[\Delta^2]\end{aligned}\tag{5.58}$$

$$\begin{aligned}\hat{G}_C^{(2)}(0) &= E[\hat{N}^2] = E[N^2]E[F^2] = E[N^2](1 + E[\Delta F^2]) \\ &= G_C^{(2)}(0) \cdot (1 + E[\Delta F^2]) ,\end{aligned}\tag{5.59}$$

where both noise variances $E[\Delta^2]$ and $E[\Delta F^2]$ contribute to the $g^{(2)}(0)$ amplitude, requiring a normalization of the correction term for a proper interpretation of $g^{(2)}(0)$.

5.9 Influence of Detection Efficiency

As the $g^{(2)}$ correlation function depends on the counting statistics of the system that is being investigated, the question arises if these statistics are influenced by the detection efficiency of the apparatus. The effect of missing single detection events due to limited detection efficiency is called random deletion and in fact does not affect the statistics of a Poisson distributed process. This is an important fact, as this distribution is the reference for all correlation evaluations. In order to show this, we assume a mean number of events $\langle N \rangle = \bar{n}$, with the Poisson distribution for measuring k events within a fixed period of time denoted by $P_{\lambda=\bar{n}}(k)$. Furthermore, we introduce the Binomial probability distribution $B(k|n, p)$ for measuring a number of k out of n events. The chance of success for a single event in the Binomial is given by p . The distributions are defined as follows:

$$P_{\bar{n}}(k) = \frac{\bar{n}^k}{k!} e^{-\bar{n}}\tag{5.60}$$

$$B(k|n, p) = \binom{n}{k} p^k (1-p)^{n-k}.\tag{5.61}$$

We compose the joint probability of detecting k events from a Poissonian source with a mean number of events \bar{n} and a detection efficiency of p :

$$D(k|\bar{n}, p) = \sum_{m=k}^{\infty} P_{\bar{n}}(m) \cdot B(k|m, p). \quad (5.62)$$

As shown in appendix A.1, the composed probability distribution $D(k|\bar{n}, p)$ is just another Poisson distribution with a reduced mean value

$$D(k|\bar{n}, p) = P_{p\bar{n}}(k). \quad (5.63)$$

A random deletion of events therefore does not alter the characteristics of a Poissonian process. This however isn't automatically true for any non-Poissonian distribution. In the context of correlations, our main interest lies in measuring sub- and super-Poissonian distributions. Implicitly, the statistical variance is a criterion for identifying bunching or anti-bunching behavior of a system, as quantities like the amplitude of $g^{(2)}$ or the Fano factor¹ are directly proportional to it. The Burgess' variance theorem [83,84] states that the variance $E[\Delta M^2]$ of a distribution M that is affected by random deletion is given by

$$E[\Delta M^2] = p^2 E[\Delta N^2] + p(1-p)E[N], \quad (5.64)$$

where $E[\Delta N^2]$ denotes the variance of the original distribution N . The theorem shows that the variance of any non-Poissonian distribution is drawn towards the Poisson expectation value of $E[M]$ as the detection efficiency decreases. The amplitude of the quantum mechanically derived $g^{(2)}(0)$ function however is not affected by random deletion. This becomes apparent when inserting equation 5.64 into the expression $g_M^{(2)}(0)$ for a process that is subject to random deletion

$$\begin{aligned} g_M^{(2)}(0) &= 1 + \frac{E[\Delta M^2] - E[M]^2}{E[M]^2} = 1 + \frac{p^2 \langle \Delta N^2 \rangle + p(1-p)E[N] - pE[N]^2}{p^2 E[N]^2} \\ &= 1 + \frac{E[\Delta N^2] - E[N]^2}{E[N]^2} = g_N^{(2)}(0). \end{aligned} \quad (5.65)$$

The $g^{(2)}(0)$ amplitude of a sub- or super-Poissonian process is thus independent from the detection efficiency.

¹The Fano factor $F = \sigma^2/\bar{n}$ has been used to characterize anti-bunched Franck-Hertz light [81]. The effects of noise and random deletion are also discussed in [82].

Temporal Correlations in Cold Bose Gases

This chapter will focus on the measurement of density correlation functions in cold gases by taking advantage of the single atom sensitivity of the detection system. In the following, the acquisition and the statistical analysis of ion detection events for evaluating second order correlations are described. Using the scanning electron microscope it was possible to observe the bunching effect in thermal bose gases and to perform the first measurement of temporal correlations therein. These results are compared to the predictions derived in the previous chapter and are discussed in detail. This chapter concludes with the measurement of temporal correlations in a BEC where, in accordance to theory, no bunching of particles was detected.

6.1 Measurement Setup

Using scanning electron microscopy the probing process for temporal correlations is conceptually simple. During the time in which a prepared atomic sample is held in its trap, the electron beam is pointed at a single fixed position within the cloud and locally ionizes the atoms. The time resolved signal of ion detection events is recorded by the MCB device for evaluation. In an ideal temporal correlation measurement all localization events should originate from a single point in space. As seen in Figure 6.1, the real picture is a little bit more complex. The electron beam's finite size and the possibility of ionizing any atom along its path of propagation define a volume that is given by the beam's spot size and the extent of the

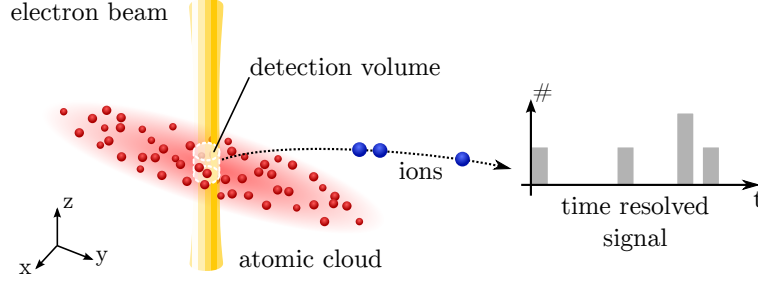


Figure 6.1: Illustration of the electron beam crossing the atomic cloud. For the correlation measurements the electron beam is focused at the center of the optical dipole trap where the atomic sample is held. Any particle being ionized and detected during the continuous electron exposure originates from within the depicted intersection volume of electron beam and atomic cloud.

atomic cloud. Since the detection scheme cannot determine or discriminate the position of an ionization event within this volume, the measured correlation signal is a mixture of spatial and temporal contributions. This generally results in a reduction of the correlation amplitude and additionally changes the behavior of the thermal correlation function.

In order to minimize this effect the ionization volume must be reduced. To this end, the electron beam is calibrated for smallest possible spot sizes before conducting the correlation measurements. This is accomplished by superimposing an optical lattice on the atomic sample and optimizing the contrast of the scanning electron microscopy images thereof. Utilizing the analysis method described in the chapter for imaging atomic density distributions, an approximate FWHM of 130 nm is achieved which estimates the ionization volume in the x and y direction. The cloud's extent in the z direction is given by the trap geometry and thermodynamical properties of the ensemble. When assuming an ideal gas of thermal atoms in a harmonic trap the density distribution is proportional to

$$\rho(z) \propto \exp\left(-\frac{m\omega_z^2}{2k_B T} z^2\right) \Rightarrow \sigma_z = \sqrt{\frac{k_B T}{m_{\text{Rb}} \omega_z^2}}. \quad (6.1)$$

Equation (6.1) shows that the thickness of the cloud is reduced for higher trapping frequencies ω_z and lower temperatures T . As pointed out in the discussion of spatially averaged correlations within the previous chapter, the expected signal strength rises as the vertical extent of the trapped sample decreases. A harmonic trapping geometry with a higher vertical oscillation frequency, such as the lightsheet dipole trap introduced in the

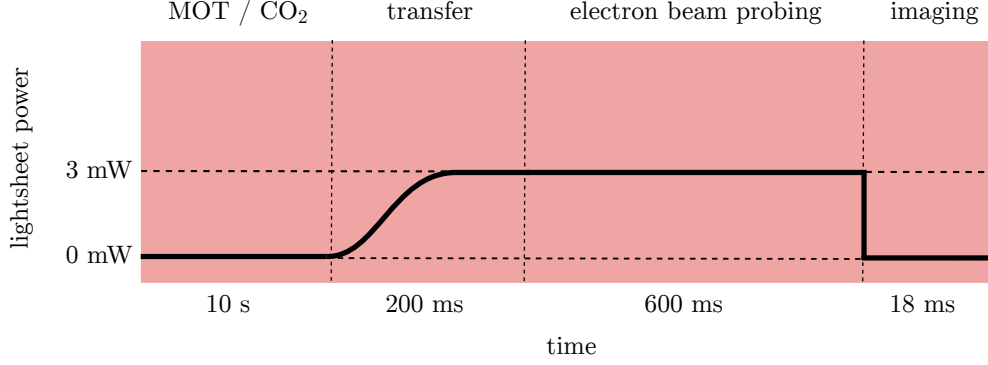


Figure 6.2: *Experimental cycle for the lightsheet trap during correlation measurements. The atoms collected in the MOT and subsequently cooled in the CO₂ trap are transferred to the lightsheet by smoothly increasing its power for 200 ms. The power of the CO₂ trap is simultaneously reduced so that the atoms are solely held by the lightsheet for 600 ms in which the sample is probed with the electron beam. After releasing the atoms from the trap an absorption image is taken after 18 ms time of flight.*

experimental setup, is thus favorable. It allows for the preparation of very thinly confined samples and was specifically designed for the task of measuring correlations in cold quantum gases.

Similar to the experiments presented before, the sequence for a correlation measurement begins with collecting ^{87}Rb atoms in the magneto optical trap and transferring them to the CO₂ optical dipole trap. After this first transfer the atomic gas can be evaporatively cooled down until a predetermined trap depth is reached. The choice in preparation eventually controls the temperature and the residual number of atoms in the sample. This way either a pure BEC, a bimodal distribution or a thermal cloud above the critical temperature for condensation can be realized.

The atomic cloud prepared within the CO₂ trap is then adiabatically transferred to the lightsheet and is thus reshaped to the new trapping geometry. Figure 6.2 depicts this process where the power of the lightsheet is smoothly ramped up within a duration of 200 ms. At the same time the power of the CO₂ trap is simultaneously reduced so that after the completion of the transfer process the atoms are held solely by the lightsheet. For the correlation measurements the sample is kept within the trap for a duration of 600 ms in which the atoms are probed by the electron beam. To maximize the amount of detection events the electron

beam is pointed at the center of the atom distribution. This reduces the number of experiments required for an acceptable signal to noise ratio. After the measurement the atomic cloud is released and an absorption image is taken after 18 ms time of flight. With the completion of this sequence the experimental cycle starts anew.

During the measurement time of 600 ms in each experimental realization the MCB device saves a histogram of time resolved detection events with a resolution of 10 μ s. Although the temporal resolution of the detection system is 100 ns, the limited number of channels in the MCB requires larger bin widths in order to extend the total measurement time. About 1,000 ions are typically detected for each single run. If we are, for example, to determine the mean number of atoms within one of the 60,000 time bins, a minimum of 1,500 measurements is needed for reducing the relative statistical error $1/\sqrt{N}$ to 20 %. This requires a certain degree of reproducibility. The absorption image allows for monitoring the stability of the cloud's temperature and atom number while the experiment is repeated for an extended amount of time. Long term drifts can be countered by small adjustments in the preparation sequence. However, if an experimental realization diverges from the desired parameters the results are discarded.

Another factor to be discussed is the role of the multiply charged ions which had to be taken into account in the imaging of density distributions. About 96 % of all detected ions are either singly, doubly or triply charged [60, 85]. Their difference in time of flight adds an uncertainty of 7 μ s to the exact time of the localization event. This effect however is blurred out by the chosen time resolution of 10 μ s. Also the time scale of the expected correlation signals is much larger than the time of flight differences. We therefore neglect multiply charged ion effects in the evaluation of correlation measurements.

6.2 Evaluation of Temporal Correlations

From the analysis of the time resolved detection events it is possible to derive any order of the temporal density correlation functions $g^{(n)}$. The principles in their evaluation shall be illustrated by $g^{(2)}$. We recall its definition and the statistical interpretation thereof

$$g^{(2)}(t_i, t_j) = \frac{\langle \psi_i^\dagger \psi_j^\dagger \psi_j \psi_i \rangle}{\langle \psi_i^\dagger \psi_i \rangle \langle \psi_j^\dagger \psi_j \rangle} \rightarrow g^{(2)}(t_i, t_j) = \frac{E[N_i N_j]}{E[N_i] E[N_j]}. \quad (6.2)$$

6.2. Evaluation of Temporal Correlations

			10 μ s				measurement time t
measurement 1	1	0	0	0	1	0	2
measurement 2	1	1	0	0	1	1	0
measurement 3	0	0	2	1	0	0	1
...							
number of measurements							
							number of detected ions

Figure 6.3: Tabular arrangement of detection events. Every row represents one of many individual experimental realizations of the measurement. Each cell contains the number of detected particles within a $10\mu\text{s}$ bin at time t of the 600ms electron beam probing period. The size of a typical table is $1,500 \times 60,000$ and contains between two and three million counts.

The measurement of the number of particles in a $10\mu\text{s}$ bin at times t_i of the 600ms electron probing is represented by the random variables N_i . The two dimensional $g^{(2)}$ function is an average over the repeatedly measured detection counts for each combination of the $60,000$ bins N_i . The computational effort can be minimized by conveniently organizing the measured data in a tabular arrangement as depicted in Figure 6.3. Every row represents one of the individual experimental realizations. Within column i , each cell contains the number of detected particles in a bin N_i at time t_i . The size of a typical table is $1,500 \times 60,000$ and contains between two and three million counts.

For two specific times t_i and t_j the correlation function $g^{(2)}(t_i, t_j)$ is calculated by first averaging the row-wise products of column i and column j and then normalizing the result by the individually averaged columns. As shown in Figure 6.4, the evaluation of all pairs t_i and t_j can be represented by a matrix. The main diagonal contains the results for equal times $t_i = t_j$. The correlation values for fixed time differences $g^{(2)}(t_i, t_i + n \cdot 10\mu\text{s})$ are found in the n -th secondary diagonal. Since the $g^{(2)}$ function is symmetric

$$g^{(2)}(t_i, t_j) = g^{(2)}(t_j, t_i), \quad (6.3)$$

it is sufficient to evaluate either the upper or the lower half of the matrix.

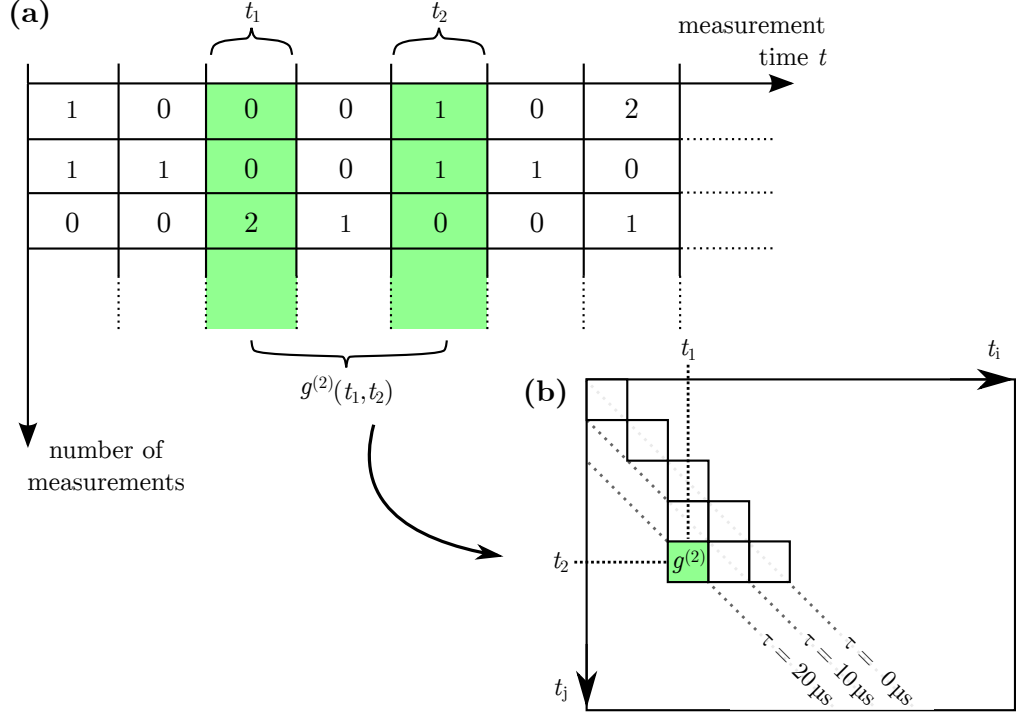


Figure 6.4: Evaluation of the $g^{(2)}(t_i, t_j)$ matrix. (a) For two specific times t_i and t_j the correlation function $g^{(2)}(t_i, t_j)$ is calculated by first averaging the row-wise products of column i and column j and normalizing the result by the individually averaged columns. (b) The main diagonal contains the results for equal times $t_i = t_j$. The correlation values for a fixed time difference $g^{(2)}(t_i, t_i + n \cdot 10 \mu\text{s})$ are found in the n -th secondary diagonal.

6.3 Density Correlation of Time Differences

Ideally, a correlation signal should be independent from the absolute time of measurement. For the interpretation of $g^{(2)}$ it is thus convenient to reduce the measured signal to a function of time differences τ only. This can be done by averaging over the correlation values of fixed time differences $\tau = n \cdot 10 \mu\text{s}$ which are found in the n -th secondary diagonal of the $g^{(2)}(t_i, t_j)$ matrix described in Figure 6.4. To ensure that the condition of absolute time independence is fulfilled, we can observe the fixed time difference signal over the measurement time of 600 ms by examining these secondary diagonals. In Figure 6.5 the signals of two exemplary thermal correlation measurements are shown. In order to reduce the noise an average of

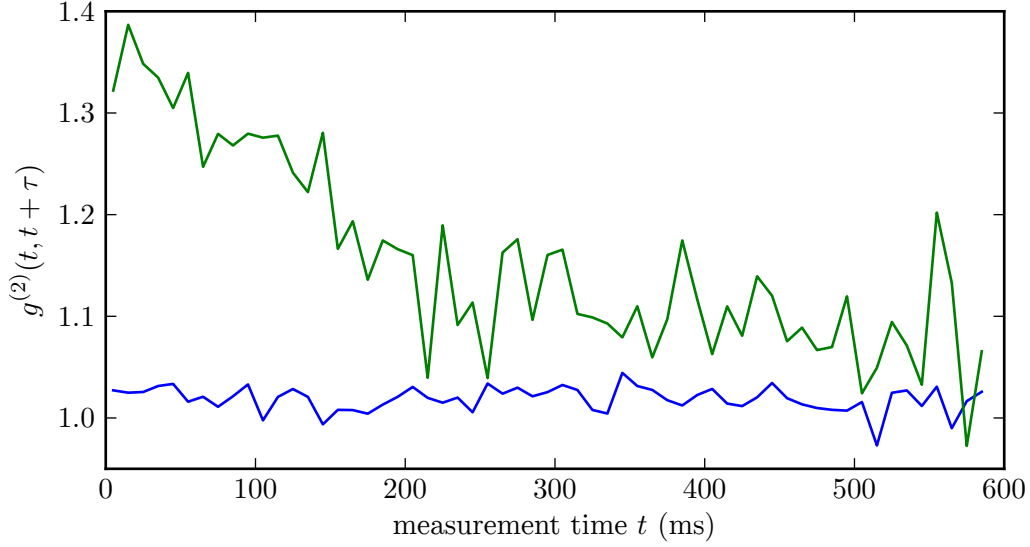


Figure 6.5: Correlation function $g^{(2)}(t, t + \tau)$ for absolute times t_i and a fixed time difference τ . Such data can be obtained from a secondary diagonal of the $g^{(2)}$ matrix described in Figure 6.4. Averaged results with $10\mu\text{s} < \tau < 100\mu\text{s}$ are shown for two exemplary measurements of thermal correlations. In an ideal experiment the correlation function should be independent from the time t within the measurements. One of the examples shows a systematic drift of the amplitude that indicates an instability in the preparation of the atomic sample.

multiple diagonals is used for the graph, where $10\mu\text{s} < \tau < 100\mu\text{s}$. The difference in both measurements is clearly visible. For the blue dataset the correlation amplitude can be regarded as constant throughout the measurement time. Averages over the elements of fixed time differences are thus possible and allow for a reduction of $g^{(2)}(t_1, t_2)$ to the more practical, one dimensional $g^{(2)}(\tau)$ function.

The green dataset however shows a strong dependence of the $g^{(2)}$ amplitude regarding absolute measurement times t . The most probable reason for this is an instability in the preparation of the observed system causing density oscillations or an evolution of the atomic sample's temperature. An average over absolute times would mask this dynamic behavior and lead to an incorrect interpretation of the data. Under certain circumstances the evaluation of such time dependent systems is still possible but requires special care. An example for this is the analysis of density correlations in a BEC to be discussed later in this chapter.

For now it shall be assumed that a system can be regarded as constant

throughout the measurement and a reduction of $g^{(2)}(t_1, t_2)$ to $g^{(2)}(\tau)$ is allowed. In this case the amplitudes for a fixed time difference τ are interpreted as a repeated measurement of $g^{(2)}(\tau)$ that is approximated by an average $E_t[\dots]$ over time

$$g^{(2)}(\tau) = E_t \left[g^{(2)}(t, t + \tau) \right] = E_t \left[\frac{G^{(2)}(t, t + \tau)}{n(t) n(t + \tau)} \right]. \quad (6.4)$$

When identifying $G^{(2)}$ and the norm $\aleph = n(t) n(t + \tau)$ as random variables, equation (6.4) can be understood as an expectation value of the form $E \left[\frac{X}{Y} \right]$ which may be simplified to [86]

$$E \left[\frac{X}{Y} \right] = \frac{E[X]}{E[Y]} \iff \sigma \left(\frac{X}{Y}, Y \right) = 0. \quad (6.5)$$

This means that the correlation function $g^{(2)}(\tau)$ can be written as a quotient of expectation values

$$g^{(2)}(\tau) = \frac{E_t \left[G^{(2)}(t, t + \tau) \right]}{E_t \left[n(t) n(t + \tau) \right]} \iff \sigma \left(g^{(2)}(t, t + \tau), \aleph(t, t + \tau) \right) = 0, \quad (6.6)$$

if there is no statistical correlation between the already normalized $g^{(2)}$ and its normalization \aleph . This assumption is valid for any reasonable measurement where $g^{(2)}$ can be regarded as constant over time and independent from the count rate. Both the nominator and the denominator within equation (6.6) can be interpreted as discrete autocorrelation functions which, according to the Wiener-Khinchin theorem (see equation (5.9)), may be calculated alternatively using Fourier transforms. Utilizing the fast Fourier transform algorithm (FFT) for discrete data, $g^{(2)}(\tau)$ can be evaluated with much less computational effort compared to the full evaluation of the $g^{(2)}(t_i, t_j)$ matrix.

6.4 Thermal Bunching of Bosons

Using the described measurement setup and methods of statistical evaluation, the temporal second order correlation function $g^{(2)}(\tau)$ has been measured for two thermal ensembles with different temperatures. Due to the influence of an artifact that is caused by the ion detector's signal processing, we discard the first two data points for $\tau = 0 \mu\text{s}$ and $\tau = 10 \mu\text{s}$. The remaining data is binned to $50 \mu\text{s}$ for better visual representation. Figure 6.6 shows the results which clearly reveal the expected bunching

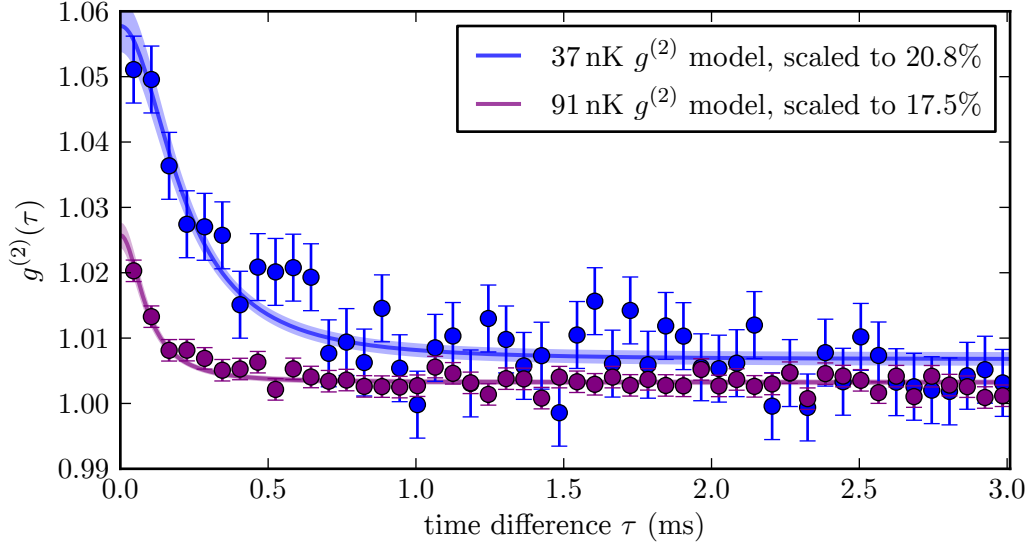


Figure 6.6: Observation of the temporal density correlation effect in thermal clouds at temperatures of 37 nK and 91 nK. The two series of measurements are compared to a spatially averaged $g^{(2)}(\tau, r)$ model by varying amplitude and offset. The optimal solutions are shown as solid curves, the areas behind depict the standard errors of the fit. The theory is in very good agreement with the measurements and reproduces the increase of the correlation time for lower temperatures. The absolute amplitude however is only 20 % of the expected signal strength.

behavior in the detection of thermal bosons. In accordance to theory, the characteristic time scale of the measured temporal correlation grows as the temperature of the atomic sample decreases.

For a direct comparison the spatially averaged $\tilde{g}^{(2)}(\tau)$ function from equation (5.40) is fitted to the experimental data. It accounts for the reduction of the correlation amplitude and the modified correlation time due to the given detection volume. The ensemble temperatures of 37 nK and 91 nK were obtained from the absorption images for controlling the stability of the system. The theoretical models, which are fitted in amplitude and offset, are in good agreement with the measured temporal correlation function and the timescales are matching our predictions. One irregularity is the asymptotic behavior for large time differences τ . Instead of approaching $g^{(2)} = 1$, both signals drop to an offset of about 0.5 % above one. As shown in a discussion later on, this small deviation is fully explained by the total atom number variations encountered throughout the measurement. Another discrepancy to the theoretical model is the amplitude of the data, which only amounts to 20 % of the expected correlation

signal. Possible explanations for this reduction shall be investigated in the following.

Repulsive Interactions

In the derivation of the spatio-temporal correlation function an ideal non-interacting gas of Bosons has been assumed. An interaction between the atoms intuitively affects the probability of finding two atoms being close together. For cold Rb⁸⁷ atoms the repulsive interaction between two particles is characterized by the s-wave scattering length of $a_s = 99 a_0$. A correction of the spatial correlation function that includes the interaction effects is given by [80]

$$g_I^{(2)}(\Delta r, \tau) = 1 + \frac{2a_s^2}{\Delta r^2} + |g^{(1)}(\Delta r, \tau)|^2 \left(1 - \frac{4a_s}{\Delta r}\right). \quad (6.7)$$

For $a_s = 0$ the interacting model $g_I^{(2)}(\Delta r, \tau)$ reduces to the known non-interacting $g^{(2)}$ correlation function for a thermal ensemble. The impact of this correction on the correlation amplitude is very strong and causes an anti-bunching behavior for small distances [80]. Proceeding in the same manner as before, the measurement process of $g_I^{(2)}$ is described as an average $\tilde{g}_I^{(2)}$ over all possible pairs of detection probabilities within the experimental localization volume. Since short distances make up only a small fraction of the averaged $\tilde{g}_I^{(2)}$ function, the influence of interactions becomes less important as the volume of integration grows. For typical experimental parameters the difference of the volume integrated correlation amplitude with and without interactions is only 5 % or less. The effect of repulsive interactions alone does not explain the discrepancy between the expected and the measured correlation function.

Spatial Average

The major cause of reduction in amplitude is the spatial average over the finite localization volume. Since the exact extent of this volume is unknown, several assumptions based on the experimental parameters must be made. For the electron beam's spot size, which has been minimized by optimizing the contrast of an optical lattice, a FWHM of 120 nm was assumed. Even if the real size is widened by a factor of 4, the discrepancy in correlation amplitude would still be 42 %. Such a scenario would also imply a significant flaw in the optimization procedure. A more severe reduction of the amplitude is caused by the thickness of the atomic cloud.

It is determined by the temperature of the sample and the trap geometry. The calculation of the trapping potential takes the Gaussian beam shape of the lightsheet as well as the gravity into account. However, the estimation relies on the beam's power and waist that must be measured outside of the experimental chamber. The real trapping potential and thus the geometry of the thermal cloud might differ from these control measurements. An increase of the cloud's thickness by a factor of 4 would lead to an agreement of 83 %.

Coherent Fraction

Despite the fact that the analyzed absorption images of the released atomic samples indicate a purely thermal distribution of atoms, a small coherent fraction of atoms might have been present since the chosen temperatures for the measurements were close to the critical temperature T_C for condensation. Such a fraction would greatly diminish the correlation amplitude, as it is concentrated at the center of the cloud where the electron beam probing takes place. This possibility may be ruled out by additional measurements with thermal ensembles well above T_C .

Although there are plausible reasons for the discrepancy between the measured and the expected signal amplitude, a decisive explanation cannot be given without further measurements for consolidation. Nevertheless, the most important feature, the temporal correlation in thermal ensembles and the timescale thereof, has been successfully measured. The result demonstrates the versatility of the scanning electron microscopy technique and the possibility for applications other than high resolution imaging.

6.5 Third Order Correlations

The data from which the second order correlation function $g^{(2)}$ was derived also allows for an investigation of three-body-correlations in time. This can be achieved by calculating the third order correlation function $g^{(3)}(t_1, t_2, t_3)$, which is a measure of likelihood for successively detecting three particles at absolute times t_i . The statistical interpretation of this function is derived in the same manner as for $g^{(2)}$ from equation (5.49)

$$g^{(3)}(t_i, t_j, t_k) = \frac{\langle \psi_i^\dagger \psi_j^\dagger \psi_k^\dagger \psi_k \psi_j \psi_i \rangle}{\langle \psi_i^\dagger \psi_i \rangle \langle \psi_j^\dagger \psi_j \rangle \langle \psi_k^\dagger \psi_k \rangle} \rightarrow \frac{E[N_i N_j N_k]}{E[N_i] E[N_j] E[N_k]}. \quad (6.8)$$

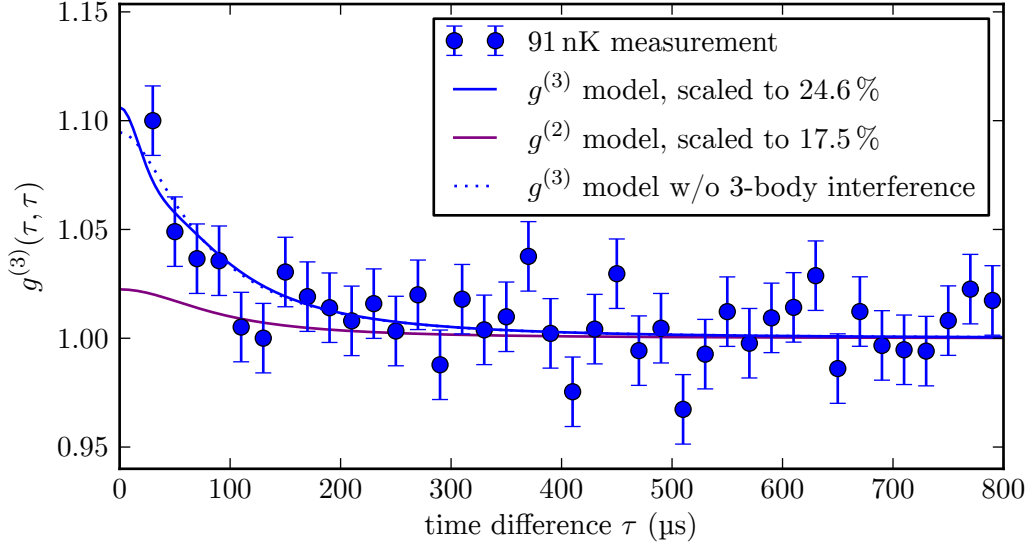


Figure 6.7: Temporal third order correlations in thermal Bose gases at a temperature of 91 nK. The measurement is compared to a spatially averaged $g^{(3)}$ model by fitting its amplitude. The theory is in good agreement with the measured correlations, although it overestimates the amplitude of the signal. The discrepancy in amplitude is similar to the scaling that was also applied during the evaluation of second order correlations.

An evaluation of three-body-correlations for absolute times can thus be conveniently performed using the unmodified tabular arrangement described in the measurement of $g^{(2)}$. However, calculating the full three-dimensional matrix for $g^{(3)}$ would require an immense amount of computational effort and space. The analysis will therefore be restricted to averages of time differences $\tau_{1,2}$ and $\tau_{2,3}$ between the first and the last two particles

$$g^{(3)}(\tau_{1,2}, \tau_{2,3}) = \frac{1}{n} \sum_{\substack{i,j,k \\ |t_i - t_j| = \tau_{1,2} \\ |t_j - t_k| = \tau_{2,3}}} g^{(3)}(t_i, t_j, t_k). \quad (6.9)$$

Since the temporal spacing between the first and the last particle $\tau_{1,3} = \tau_{1,2} + \tau_{2,3}$ is fixed, the average over absolute times reduces $g^{(3)}(t_1, t_2, t_3)$ to a two-dimensional expression.

Figure 6.7 shows the $g^{(3)}(\tau, \tau)$ function of a thermal correlation measurement for identical temporal spacings $\tau_{1,2} = \tau_{2,3} = \tau$. The data clearly shows the presence of the thermal bunching effect which has also been observed within the $g^{(2)}$ signal. The corresponding $g^{(2)}$ model for this mea-

surement is shown for comparison. Particularly noticeable is the increase in amplitude of $g^{(3)}$. This is in accordance to the theoretical expectation, since the maximum amplitude of the ideal n -th order $g^{(n)}$ correlation function for a thermal source follows the factorial $n!$. The signal to noise ratio however suffers from the reduced probability of finding three instead of two particles for a given temporal spacing. A direct comparison to theory is achieved by deriving a spatially averaged $\tilde{g}^{(3)}(\tau, \tau)$ function in analogy to equation (5.35). Using the weighting function $p(\mathbf{r})$, we integrate¹

$$\begin{aligned} \tilde{g}^{(3)}(\tau_{1,2}, \tau_{2,3}) = & \iiint d^3r_1 d^3r_2 d^3r_3 p(\mathbf{r}_1) p(\mathbf{r}_2) p(\mathbf{r}_3) \\ & \cdot g^{(3)}(|\mathbf{r}_1 - \mathbf{r}_2|, |\mathbf{r}_2 - \mathbf{r}_3|, |\mathbf{r}_1 - \mathbf{r}_3|, \tau_{1,2}, \tau_{2,3}, \tau_{1,3}) \end{aligned} \quad (6.10)$$

over the spatio-temporal third order correlation function for a thermal Bose gas from equation (5.34)

$$g^{(3)} = 1 + |g_{12}^{(1)}|^2 + |g_{23}^{(1)}|^2 + |g_{13}^{(1)}|^2 + 2 \operatorname{Re}[g_{12}^{(1)} g_{13}^{(1)} g_{23}^{(1)}], \quad (5.34)$$

where $g_{ij}^{(1)}$ is an abbreviation for the thermal $g^{(1)}(|\mathbf{r}_i - \mathbf{r}_j|, \tau_{i,j})$ correlation function of the particles i and j . The spatially averaged $\tilde{g}^{(3)}$ model is calculated for the estimated experimental parameters and fitted in amplitude. As seen in Figure 6.7, the theory is in good agreement with the measured signal and the scaling resembles the observed reduction of the $g^{(2)}$ correlation amplitudes in Figure 6.6. However, for the given experimental parameters the spatial averaging caused by the finite detection volume does not allow for an exclusive characterization of the three-particle bunching effect. The dotted line in Figure 6.7 visualizes a modified $g^{(3)}$ correlation function for which the three-particle interference term in (5.34) has been omitted. The comparison to the original function illustrates that two-particle correlations are the dominant contribution to the observed $\tilde{g}^{(3)}$ function.

6.6 Uncorrelated Control Measurement

To ensure that the correlations found in the analysis of detection events indeed originate from the thermal bunching effect, an uncorrelated control measurement is performed. By carefully choosing experimental parameters that deny the detection of any real correlation signal, we can

¹Solution of the spatial $g^{(3)}$ average is given in A.5.

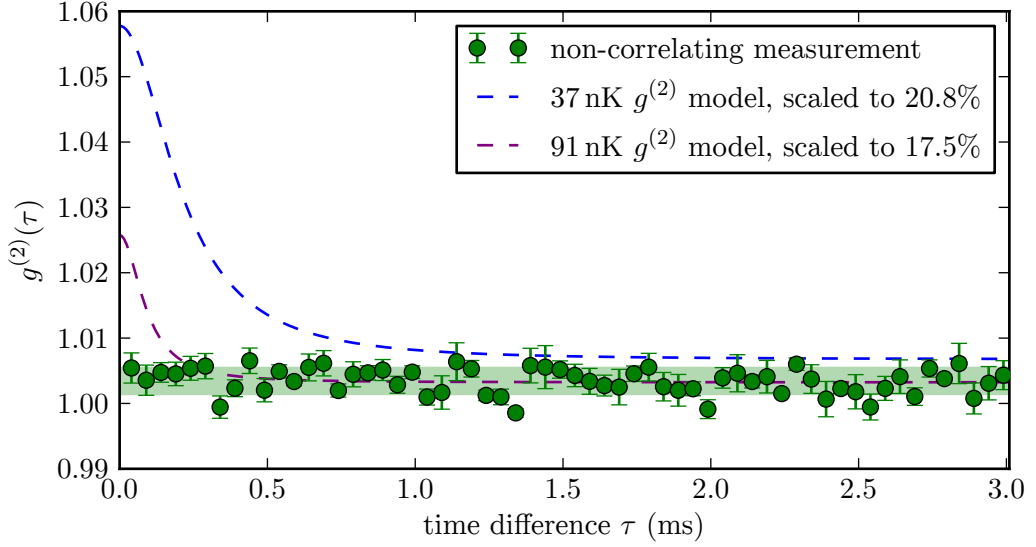


Figure 6.8: Second order correlation function $g^{(2)}(\tau)$ of a control measurement in which no correlation signal is expected. The experiment has been prepared in a way so the correlation time and amplitude are too small to be detected. The data (green points) shows that the measured signal is indeed flat and only 0.3 % above the expected value of $g^{(2)}(\tau) = 1$. Mean and standard deviation of the offset are depicted by the green background. The fitted $g^{(2)}$ model functions from the thermal correlation experiments are shown for comparison.

determine if the results are suspect to systematic errors caused by the measurement procedure.

The chosen strategy is to load a thermal cloud with a temperature of 240 nK into the light sheet. This cloud is probed by an intentionally defocused electron beam. Due to the electron beam's broadening beyond the thermal wavelength of the atoms $\lambda_T = 380$ nm, the correlation effect is strongly mitigated as this length scale cannot be resolved anymore. Also, the higher temperature results in a strong reduction of the correlation amplitude due to the spatial averaging in the propagation direction of the beam. Furthermore, the temporal correlation length for this temperature is only 32 μ s, which means that also the capability of resolving the signal in time is considerably reduced. In conclusion, the expected correlation amplitude should be equal to one for all time intervals $g^{(2)}(\tau) = 1$.

Figure 6.8 shows the measured $g^{(2)}$ function for the described control experiment. The fitted $g^{(2)}$ model functions from the thermal correlation experiments are shown for comparison. As expected, the correlation am-

plitude is flat for all time differences and the mean signal height is only 0.3 % higher than one. This very small offset originates from total atom number fluctuations as will be explained in the following section. As with the results of the thermal correlation measurements, the first two time bins are discarded due to the artifacts caused by the signal processing electronics. The measurement however confirms that the influence of these artifacts is limited to the first two bins only and that the data for larger time differences behaves exactly as expected. This supports the conclusion that the correlation signal found in the previous experiments indeed originates from the thermal bunching effect of Bosons.

6.7 Noise Contribution from Total Atom Number Fluctuations

In an ideal world the measurements for determining the statistical average of a certain quantity are preferably taken under identical experimental prerequisites. For all series of correlation measurements the parameters of the atomic samples were continuously observed and stabilized as best as possible. Nevertheless, the total number of atoms for each experimental realization is subject to fluctuations. This total atom number shall be represented by a random variable N_{total} with a relative fluctuation G around the mean number of atoms \bar{n}_{total}

$$N_{\text{total}} = \bar{n}_{\text{total}} G, \quad (6.11)$$

so that $E[N_{\text{total}}] = \bar{n}_{\text{total}}$ and $E[G] = 1$. An increase or decrease of the total atom number also affects the number of detected particles \hat{N}_i per bin at time t_i on which the evaluation of $g^{(2)}$ is based on. If we assume N_i to be the number of detected particles in a perfectly stabilized environment, \hat{N}_i can be expressed as

$$\hat{N}_i = N_i G. \quad (6.12)$$

In the statistical interpretation of $g^{(2)}(t_1, t_2)$ it was found that the introduction of a multiplicative random variable F does not affect the observed correlation amplitude, as long as the noise is statistically independent from the measured observable N . In equation (5.57) it was further assumed that there is no correlation of this noise between two distinct measurements N_1 and N_2 , and thus $\sigma(F_1, F_2) = 0$. However, this assumption does not hold for a variation of the total atom number as it identically affects each time

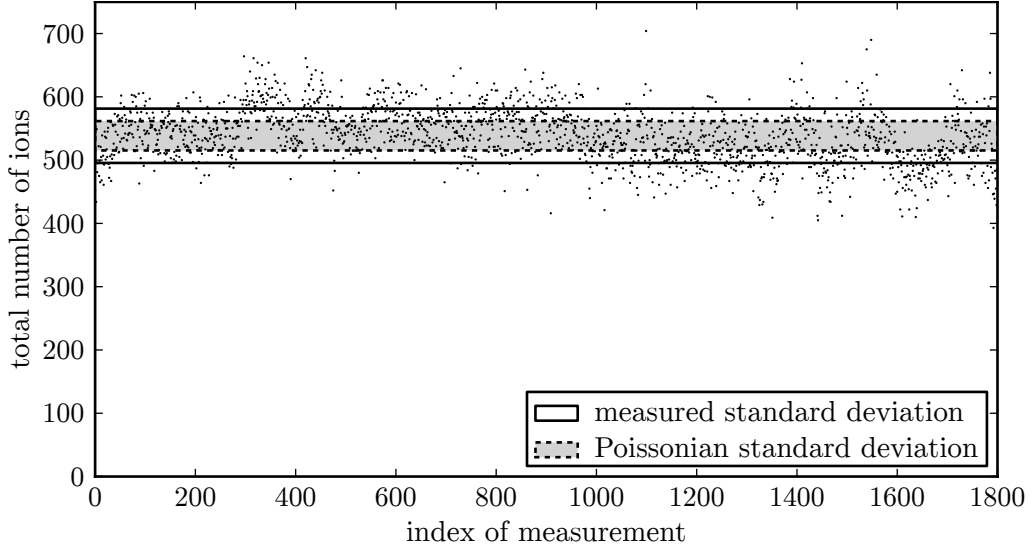


Figure 6.9: Fluctuation of the total number of detected ions in an exemplary series of correlation measurements. The expected Poissonian standard deviation for the probabilistic detection process is depicted by the gray dotted area. The measured standard deviation, which exceeds the estimation, is marked by the solid lines.

bin \hat{N}_i and therefore $G_1 = G_2 = G$. The noise affected $\hat{g}^{(2)}$ thus reads

$$\hat{g}^{(2)}(t_1, t_2) = \frac{E[\hat{N}_1 \hat{N}_2]}{E[\hat{N}_1] E[\hat{N}_2]} = \frac{E[G^2] E[N_1 N_2]}{E[N_1] E[N_2]} = E[G^2] g^{(2)}(t_1, t_2). \quad (6.13)$$

In order to obtain the undisturbed function $g^{(2)}(t_1, t_2)$, the second moment of the fluctuations $E[G^2]$ must be eliminated from the measured $\hat{g}^{(2)}$ values by appropriate normalization.

A graph in Figure 6.9 shows the total number of detected ions from an exemplary series of correlation measurements. Although no long term deviations from the mean number \bar{n}_{total} of 540 detected ions are observed, the measured standard deviation is almost two times as large as the expected Poisson standard deviation of the probabilistic detection process. For quantifying these fluctuations, the process of measuring the total atom number \tilde{N}_{total} is expressed as a product of N_{total} and the normalized noise P_G for measuring N_{total}

$$\tilde{N}_{\text{total}} = N_{\text{total}} P_G = \bar{n}_{\text{total}} G P_G, \quad (6.14)$$

6.7. Noise Contribution from Total Atom Number Fluctuations

	dataset 1	dataset 2	dataset 3	dataset 4
$E[G^2]$	1.0045	1.0025	1.0063	1.0028
$g^{(2)}$ offset measured	1.0045	1.0026	1.0061	1.0030
$g^{(2)}$ offset corrected	1.0000	1.0001	0.9997	1.0002

Table 6.1: Estimated second moment of the relative atom number fluctuation compared to the measured offset of $g^{(2)}$ for various data sets. The correction for atom number instabilities draws the correlation amplitude for large time differences down to the theoretically expected value of one, which means that the fluctuations are indeed the cause for the measured offset.

from which the expectation value of the second moment of G is derived

$$E[G^2] = \frac{1}{\bar{n}_{\text{total}}^2} \frac{E[\tilde{N}_{\text{total}}^2]}{E[P_G^2]}. \quad (6.15)$$

The large integration time of 600 ms for measuring \tilde{N}_{total} excludes the possibility of thermal correlation contributions in the statistics of the total ion numbers. An estimate for $E[G^2]$ is found if the second moment of the relative detection noise $E[P_G^2]$ in equation (6.15) is replaced by its Poissonian expectation value

$$E[P_G^2] = \frac{\bar{n}_{\text{total}} + \bar{n}_{\text{total}}^2}{\bar{n}_{\text{total}}^2}. \quad (6.16)$$

Eventually, the evaluated $g^{(2)}$ amplitudes for a series of measurements can be corrected for total atom number fluctuations by dividing them by

$$E[G^2] = \frac{E[\tilde{N}_{\text{total}}^2]}{\bar{n}_{\text{total}}^2 + \bar{n}_{\text{total}}} = \frac{\bar{n}_{\text{total}}^2 + E[\Delta\tilde{N}_{\text{total}}^2]}{\bar{n}_{\text{total}}^2 + \bar{n}_{\text{total}}}, \quad (6.17)$$

which is simply the ratio between the measured and the expected second moment of \tilde{N}_{total} . The results of applying the statistical correction to real data are shown in Table 6.1. For various thermal correlation measurements, the $g^{(2)}$ offset is determined from the averaged time distances between 10 ms and 50 ms, where no thermal correlation signal is to be expected. The corrected $g^{(2)}$ amplitudes are practically identical to the expected value of $g^{(2)} = 1$ for time differences much larger than the thermal correlation length. The effect of total atom number fluctuations thus perfectly explains the observed offsets in the evaluated measurements.

6.8 Counting Artifacts

A feature seen in all evaluated correlation measurements is the unreasonable high amplitude of $g^{(2)}(\tau)$ for the first two bins. The most probable explanation for this is an artifact introduced by the signal processing electronics. When an incoming ion causes the channeltron detector to build up an electric charge, the charge is measured as a voltage peak. A signal with high amplitude and sharp slope can cause oscillations at the discriminator input, triggering one or more additional detection events depending on the strength of this so called ringing effect. Such effects can be estimated and quantified by taking a closer look at the counting statistics of the measurements.

As a simple approach, it is assumed that there is only a certain probability p_2 for a real incoming ion event to turn into two detection events. For simplicity the case of limited detection efficiency is omitted, as it will not change the interpretation of the result. The probability of finding exactly one event for a real incoming ion event is then $p_1 = 1 - p_2$, since the probability for an incoming event to be detected at all is one

$$\sum_k^{k_{\max}} p_k = 1. \quad (6.18)$$

In this example $k_{\max} = 2$ as we only considered doubly counted events. The probability of measuring two counts $\tilde{P}(2)$ within a fixed period of time T is the sum of the probability for finding two real correctly detected events $p_1^2 \cdot P(2)$ and a single detection event that turned into two counts $P(1) \cdot p_2$. The probability $\tilde{P}(1)$ for a single measured event on the other hand originates from a singly counted real event only

$$\tilde{P}(2) = P(2) \cdot p_1^2 + P(1) \cdot p_2 \quad (6.19)$$

$$\tilde{P}(1) = P(1) \cdot p_1. \quad (6.20)$$

The probabilities p_k should be intrinsic properties of the detection system and are presumed to be equal for each measurement. If the real detection probabilities $P(n)$ are known, the probabilities p_k can be determined by solving the equations. To this end, we restrict the analysis to systems with known characteristics. In a situation where the ion production and detection rate is governed by Poisson statistics, the mean count rate λ fully determines the probability distribution $P(n)$. An estimation for the probability of finding n counts within a fixed time T is then given by

$$P_\lambda(n) = \frac{\lambda^n}{n!} e^{-\lambda}. \quad (6.21)$$

The description only holds for stationary processes, which means that the mean count rate λ must not change. This condition is met by selecting only subsets of measurements, where the ion production rate is almost constant over time. Since the probability for detecting no events $\tilde{P}(0) = P(0)$ does not differ from the original distribution, the mean count rate can be directly obtained from

$$\lambda = -\log \tilde{P}(0). \quad (6.22)$$

Taking triply counted events or even higher multiples into account adds more complexity to the model. With increasing number of measured counts n the number of possible combinations for detection artifacts increases. We will denote these combinations by k_{\max} -dimensional vectors \mathbf{c}_i , where the component $c_i^{(k)}$ denotes the number of k -times counted events. For example, a measured number of $n = 4$ events can be a product of two ions counted twice (denoted as \mathbf{c}_1) or one ion counted correctly plus another being triply counted (denoted as \mathbf{c}_2)

$$\mathbf{c}_1 = \begin{pmatrix} 0 \\ 2 \\ 0 \end{pmatrix}, \quad \mathbf{c}_2 = \begin{pmatrix} 1 \\ 0 \\ 1 \end{pmatrix}, \quad \dots \quad (6.23)$$

or any other possible combination. The measured number of events n for a combination \mathbf{c}_i is given by the equation

$$\sum_{k=1}^{k_{\max}} k \cdot c_i^{(k)} = n, \quad (6.24)$$

which evaluates to $n = 4$ for the examples \mathbf{c}_1 and \mathbf{c}_2 above. When classifying a vector \mathbf{c}_i by equation (6.24), we can define the sets C_n containing every combination that leads to a total amount of n detected events

$$C_n = \left\{ \forall \mathbf{c}_i : \sum_{k=1}^{k_{\max}} k \cdot c_i^{(k)} = n \right\}. \quad (6.25)$$

Finally, the probability $\tilde{P}(n)$ of measuring n counts after the detector, which depends on the incoming probabilities $P(n)$ and artifact probabilities p_k , can be written as

$$\tilde{P}(n) = \sum_{\mathbf{c}_i \in C_n} \binom{m_i}{c_i^{(1)}, c_i^{(2)}, \dots, c_i^{(k_{\max})}} \cdot \left(\prod_k p_k^{c_i^{(k)}} \right) \cdot P_\lambda(m_i), \quad (6.26)$$

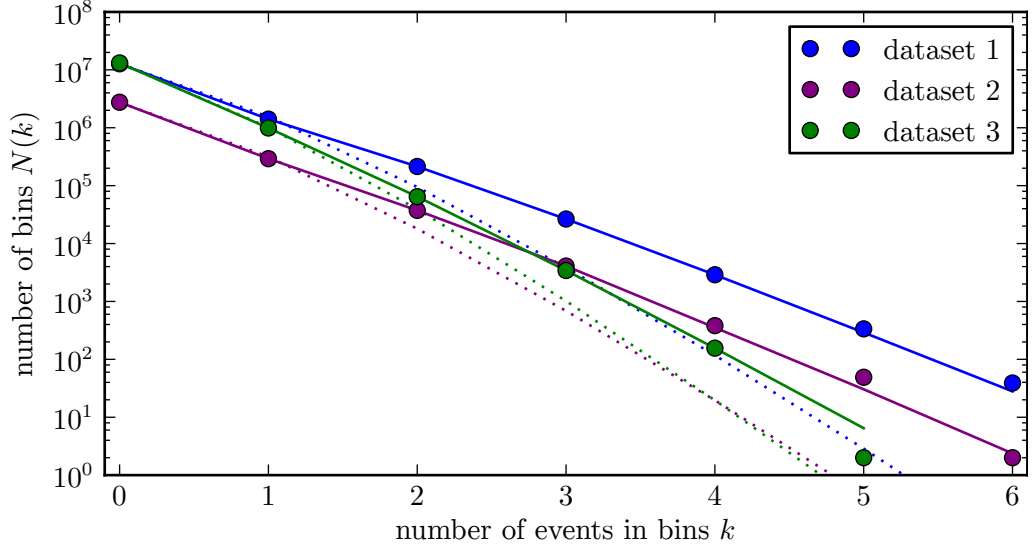


Figure 6.10: Analysis of counting artifacts. The graph shows the mean number $N(k) \propto P_m(k)$ of bins containing k detection events for three series of measurements (solid dots). Their probability distribution is expected to be Poissonian. For higher numbers of k , the measurements $P_m(k)$ exceed the expected distribution $P_\lambda(k)$ (dotted lines). The model $\tilde{P}(k)$ that includes the possibility of multiply counted events is in good agreement with the measurement (solid lines). For the first two datasets the estimated parameters for doubly and triply counted events are about $p_2 = 8\%$ and $p_3 = 0.5\%$. The third dataset however is approximated best using a model with $p_2 = 2.7\%$ and no triply counted events $p_3 = 0\%$.

where $m_i = \sum_k c_i^{(k)}$ is the number of real incoming events. The first expression in parentheses is the multinomial coefficient

$$\binom{m_i}{c_i^{(1)}, c_i^{(2)}, \dots, c_i^{(k_{\max})}} = \frac{m_i!}{c_i^{(1)} c_i^{(2)} \dots c_i^{(k_{\max})}} \quad (6.27)$$

and accounts for all permutations that can occur within the combination. The product in the second parentheses is the probability of the multi-count configuration.

When comparing the multicount model $\tilde{P}(n)$ to an experimental measurement $P_m(n)$, the unknown parameters p_k can be successively determined from $k = 1$ to $k = k_{\max}$. Once the sum of all p_k approaches one, the number of orders k_{\max} can be regarded as sufficient. Ideally, the probability of any higher number of measured counts $P_m(n > k_{\max})$ then matches the expectation $\tilde{P}(n)$.

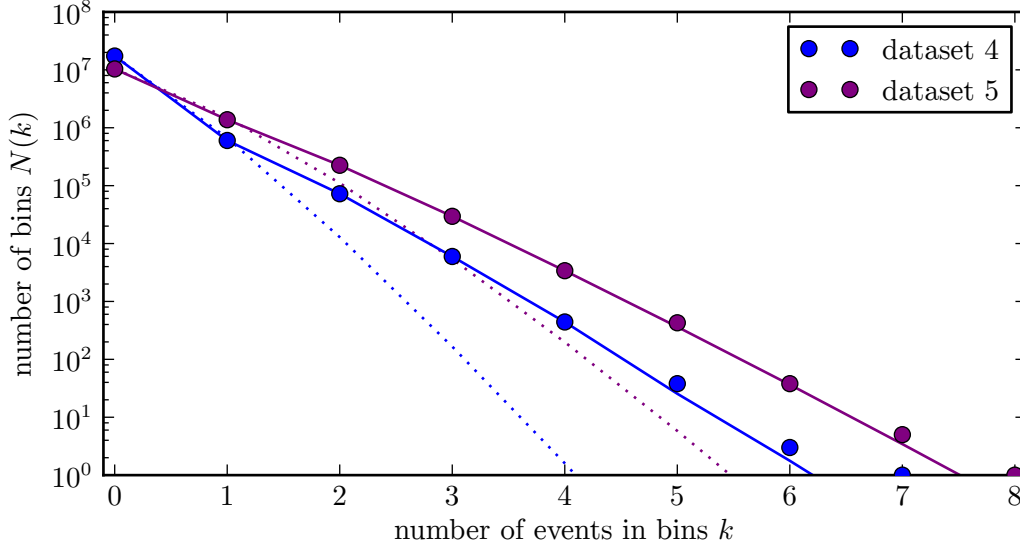


Figure 6.11: Analysis of counting artifacts for correlating measurements. The graph shows the mean number of bins $N(k) \propto P_m(k)$ containing a number of k detection events in each measurement. The multiply counted event model $\tilde{P}(k)$ (solid lines) is applied to the data, the Poissonian distributions $P_\lambda(k)$ (dotted lines) are shown for comparison. Both measurements yield similar results for the estimation of doubly and triply counted event probabilities, respectively $p_2 = 9.4\%$ and $p_3 = 0.57\%$ for the first, and $p_2 = 8.95\%$ and $p_3 = 0.55\%$ for the second set. Interestingly, the first dataset that was taken from the measurement with the strongest bunching effect shows an increased value of p_2 .

The multiply counted event model has been applied to several measurements. A series of experiments has been performed to test the assertion that an a priori uncorrelated signal results in a flat second order correlation function. In these experiments, an unfocused electron beam is held steady in the center of a thermal cloud. The number of incoming events is recorded for 600 ms and stored in 60,000 time bins. A region of the signal has been selected where the deviation of the mean count rate is about 10 % or less. As the spatial resolution is reduced, the amplitude of a thermal correlation signal vanishes. Additionally, a high temperature was chosen for the preparation of the thermal cloud, which results in reduced thermal correlation lengths and times. These parameters exclude the possibility of observing physical bunching effects, thus the ion events are expected to be uncorrelated and to follow Poissonian statistics.

In Figure 6.10, a histogram showing the number of bins containing k counts for different measurements is presented. The model $\tilde{P}(k)$ that

includes the possibility of doubly and triply counted events predicts the number of measured occurrences $P_m(k)$ with higher numbers of events k very well, which obviously deviate from a pure Poisson expectation $P_\lambda(k)$. Particularly notable is the similar behavior of the blue and purple dataset, for which the estimated probabilities of doubly and triply counted events are about $p_2 = 8\%$ and $p_3 = 0.5\%$. In contrast, the result from the green set differs significantly. Here, the best agreement is found for a model with a doubly counted event probability of $p_2 = 2.7\%$ and no triply counted events $p_3 = 0\%$.

When analyzing the experiments in which thermal correlations have been observed, the multiply counted event artifacts are the reason for not being able to evaluate the same-time correlations properly, as they induce a false bunching signal. Figure 6.11 shows the results for two such measurements. The estimated artifact probabilities yield $p_2 = 9.4\%$, $p_3 = 0.57\%$ and $p_2 = 8.95\%$, $p_3 = 0.55\%$, thus compatible with the estimations from two of the non-correlating series. Interestingly, the parameter p_2 estimated from the measurement with the highest correlation signal is also slightly higher compared to the other measurements.

In conclusion, the analysis of the counting statistics provides interesting results from data that might have been presumed to be flawed beyond usefulness, but it also raises additional questions. If the multiply counted event artifact originates solely from the detection system, the reason for a significant change in its behavior is not yet known. A dedicated investigation could provide more information about possible causes, like a recalibration of the ion optics or a change in the systems detection efficiency. If the estimation of the multiple count parameters is proven to be reliable, a statistical correction method is feasible. This in turn allows for additional possibilities in the evaluation of same-time correlation effects which are currently dominated by the artifact.

6.9 Noise Contribution in $g^{(2)}(0)$

Up to this point the counting artifacts, which dominate the statistics of $g^{(2)}(\tau = 0)$, prevented a meaningful interpretation of the density correlation amplitude for zero temporal and spatial differences. This quantity is of particular interest since it yields the maximum amplitude of the thermal correlation function. As already pointed out in equation (5.59), the evaluation of $g^{(2)}(0)$ for single density measurements is directly affected by the noise of a probe. For retrieving the real thermal correlation signal,

	dataset 1	dataset 2	dataset 3	dataset 4
$g^{(2)}(\tau \rightarrow 0)$	1.047	1.021	1.040	1.000
$g^{(2)}(0)$ Poisson corr.	1.175	1.169	1.160	1.173
$g^{(2)}(0)$ multicount corr.	1.008	0.995	0.993	0.999

Table 6.2: Correction of the $g^{(2)}(0)$ correlation amplitudes for two different estimations of the measurement noise. Using a Poisson distribution (2nd row) underestimates the noise, as the corrected values are too high in comparison with the extrapolated amplitudes from the temporal correlation fits (1st row). The multiply counted event model (3rd row) with parameters p_k obtained from the uncorrelated 4th dataset provides more reasonable results. However, the temporal correlation signal present in the datasets 1-3 is not revealed by the corrected $g^{(2)}(0)$ amplitudes.

the measured correlation amplitude $g^{(2)}(\tau = 0)$ must be cleared from the noise contribution.

The noise of the probe shall be described by a normalized multiplicative random variable P . As there is no way of discriminating the noise statistics from thermal correlation fluctuations, an educated guess of the measurement noise contribution $E[P^2]$ is required. Based on the characteristics found in the uncorrelated reference measurements, the statistical analysis of the counting artifacts that dominate the detection noise P allows for an estimation of $E[P^2]$. In order to take the ringing artifact into account, the normalized measurement noise $E[P^2]$ is calculated for the modified Poisson distribution $\tilde{P}(n)$ from equation (6.26)

$$E[P^2] = \frac{1}{E[\tilde{P}]^2} \sum_n n^2 \tilde{P}(n). \quad (6.28)$$

The multiply count parameters p_k used in $\tilde{P}(n)$ are obtained from the uncorrelated reference measurement. The mean rate λ of the Poisson distribution the model is based on is the mean ion detection rate of the bin for which the noise estimation is calculated.

Table 6.2 shows the same-time same-position $g^{(2)}$ correlation amplitude for the two different guesses of measurement noise. As already pointed out, the Poissonian statistics underestimates the measurement noise and therefore the corrected $g^{(2)}(0)$ values are much higher than the extrapolated amplitudes from the fitted temporal correlation functions $g^{(2)}(\tau \rightarrow 0)$. Using the noise estimation from the multiply count model leads to corrected values that are scattering around around $g^{(2)}(0) = 1$. The amplitude of

the uncorrelated measurement reduces to one since this is the reference for the multiply count parameters p_k .

Although the modified noise estimation provides more plausible results, the evaluation of the zero-distance $g^{(2)}$ correlation function does not reveal the thermal correlation effect that was found in three of the measurements. The dataset with the highest correlation amplitude indeed shows a small increase in amplitude by about 1 %, but the biggest impact is the uncertainty of the noise characteristics for each experiment. Even small variations in the estimated probabilities p_k for multiply counted events affect the corrected $g^{(2)}$ amplitudes noticeably. Also, as stated in the analysis of the counting statistics in section 6.8, these probabilities appear to be varying for different series of measurements. Therefore, a systematical and robust estimation of the measurement noise is required if the $g^{(2)}(0)$ amplitude or higher order correlation functions for zero distances are to be evaluated.

6.10 Density Correlations in a BEC

A Bose-Einstein condensate is the realization of a perfect coherent state of matter. The atom laser that can be formed by gradually output coupling atoms from a trapped BEC is perhaps the best demonstration of the analogy to classic coherent waves [7]. Among other experiments highlighting the similarities, the coherence of matter waves has been proven by measuring the second and third order correlation functions of atom lasers using an optical resonator for single particle detection [87].

In contrast to other experiments, we can measure the density correlation function of a BEC within the trap in the same manner we measured the thermal correlations. To this end, the atoms collected in the preparation stage of the experimental cycle are evaporatively cooled in the CO₂ dipole trap until a BEC is formed. The condensate is then transferred to the light sheet trap for measuring density correlations using the electron beam. The beam is again held steady in the center of the trap, and the ion detection events are recorded for 600 ms. The prepared samples show no detectable thermal fraction in the absorption images and are thus considered to be pure Bose-Einstein condensates.

For a perfect coherent state the second order correlation function is equal to one. In contrast to the expectation, the evaluated correlation signal from the BEC measurements exhibits large oscillations as seen in Fig-

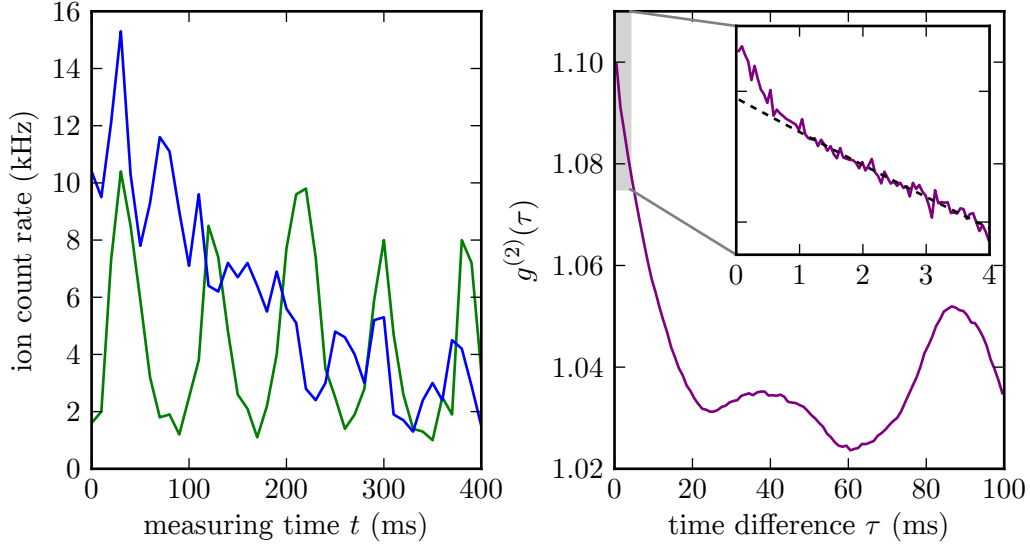


Figure 6.12: The left graph shows two distinct signals from a series of BEC correlation measurements, averaged over bins of 10 ms. During the green measurement the BEC oscillated within its confinement, causing a periodic pattern in the ion signal. This oscillation is random in its appearance and strength as seen in comparison with another identically prepared measurement (blue). It therefore manifests itself also in the density correlation in the right graph. However, a small feature is present on top of the oscillation (inset). Its timescale matches a thermal correlation signal.

ure 6.12 on the right. An explanation for this behavior is found in the analysis of the time dependent ion signals from the individual measurements. Most of the signals clearly show a presence of density oscillations (left graph in Figure 6.12). The two frequencies that can be derived from the correlation signal peaks are 11 Hz and 26 Hz. As these values are close to the estimated horizontal trap frequencies of the light sheet, the most probable cause is an excitation of the BEC during the transfer process. A reproducible oscillation would not affect the $g^{(2)}$ function due to the normalization term, but the excitations happen to be random in appearance and magnitude. The timescale of the oscillation however is large compared to the region of interest for thermal correlations. Investigating the $g^{(2)}$ signal for short time distances τ reveals a feature on top of the correlation artifact induced by the oscillations. If the shape of the slowly varying $g^{(2)}$ signal is extrapolated towards $\tau \rightarrow 0$ as depicted in the inset of Figure 6.12, this feature can be isolated and analyzed separately.

In order to check for any dynamic changes of the system that can be

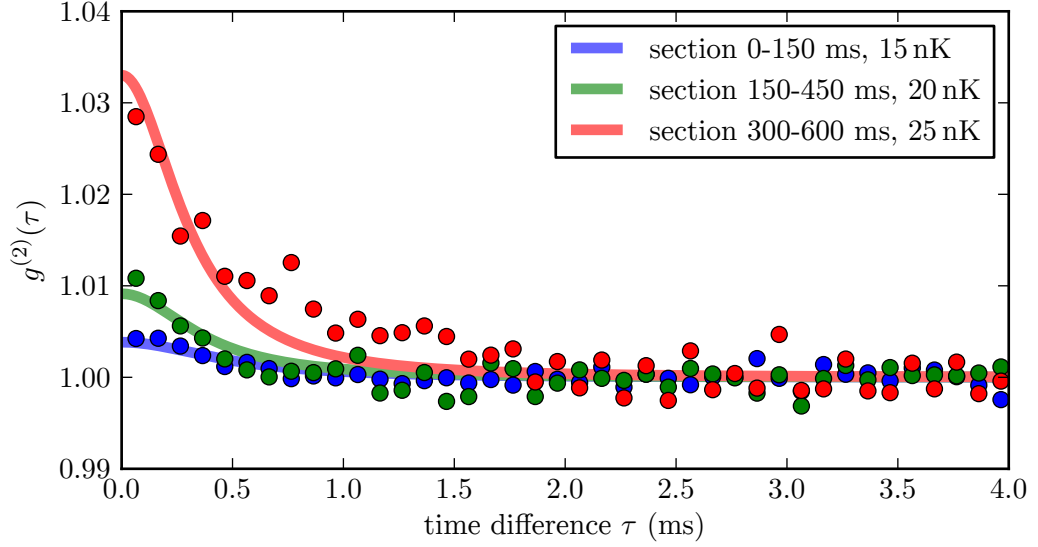


Figure 6.13: Second order correlations measured at different times in a BEC. At the beginning of the measurements the correlation signal is almost flat, showing only a minimal amplitude that is well below 1 %. This proves the coherence of the dominant condensed fraction. As time progresses, the thermal correlation signal becomes larger, which is an evidence of a heating effect being observed right within the measurement. Since the signal to noise ratio does not allow a conclusive determination of the correlation length, temporal $g^{(2)}$ functions for the three estimated temperatures below T_C are fitted in amplitude.

identified by the analysis of the correlation function, the total duration of 600 ms in which the BEC was probed in each experimental run is split into three sections. The $g^{(2)}$ signal is independently evaluated for each selection and the large timescale oscillation is removed as described. The results are shown in Figure 6.13. Each of the three evaluated measurement sections shows a very small correlation signal with a characteristic timescale that is compatible with a thermal bunching effect. The most probable reason for this is a small remaining thermal fraction in the atomic sample. Especially in the first measured section the observed bunching effect is strongly reduced by the large condensate fraction and almost vanishes, yielding an amplitude of only 0.4 %. This excellently verifies the theoretical expectation as the second order correlation amplitude of the BEC is found to be almost completely flat and equal to one. However, within the second and third section of the measurement the signal increases in strength. This might indicate an evolution of the temperature or the ratio of the condensed fraction over time.

For a quantitative analysis a description of second order correlations in Bose gases at finite temperatures below T_C is required [80]:

$$g_f^{(2)}(\mathbf{r}_1, \mathbf{r}_2) = 1 + \frac{|G_f^{(1)}(\mathbf{r}_1, \mathbf{r}_2)|^2}{G_f^{(1)}(\mathbf{r}_1, \mathbf{r}_1)G_f^{(1)}(\mathbf{r}_2, \mathbf{r}_2)} - \frac{|\Psi(\mathbf{r}_1)|^2 |\Psi(\mathbf{r}_2)|^2}{G_f^{(1)}(\mathbf{r}_1, \mathbf{r}_1)G_f^{(1)}(\mathbf{r}_2, \mathbf{r}_2)}. \quad (6.29)$$

$G_f^{(1)}$ denotes the first order correlation function for finite temperatures

$$G_f^{(1)}(\mathbf{r}_1, \mathbf{r}_2) = \Psi^*(\mathbf{r}_1)\Psi(\mathbf{r}_2) + G_T^{(1)}(\mathbf{r}_1, \mathbf{r}_2), \quad (6.30)$$

where $G_T^{(1)}(\mathbf{r}_1, \mathbf{r}_2)$ is the known first order correlation function for a thermal gas of bosons and $\Psi(\mathbf{r})$ is the wave function of the condensed fraction. The last term in equation (6.29) illustrates that the amplitude of $g_f^{(2)}$ is reduced if the amount of condensed atoms $|\Psi(\mathbf{r})|^2$ increases in relation to the total density $G_f^{(1)}(\mathbf{r}, \mathbf{r})$.

By estimating the density distribution of the measured atomic sample we can calculate the expected amplitude of a spatially averaged $\tilde{g}_f^{(2)}$ function. It is also assumed that the reduction in amplitude by a factor of 20 %, which was found in the evaluation of thermal correlations, also applies to this measurement. Within these assumptions, the behavior of the correlation signal can be explained by an increase of the temperature from 15 nK to 20 nK and 25 nK, where the condensate fraction drops from 90 % to 74 % and finally 50 %. Due to the uncertainty in the experimental parameters the estimated amplitudes of $\tilde{g}_{f,15 \text{ nK}}^{(2)} = 1.008$, $\tilde{g}_{f,20 \text{ nK}}^{(2)} = 1.012$ and $\tilde{g}_{f,25 \text{ nK}}^{(2)} = 1.018$ are of coarse accuracy, but they are in agreement with the experimentally observed amplitudes within one order of magnitude. As shown by the amplitude fitted thermal correlation functions for the assumed temperatures in Figure 6.13, the timescales of the temporal correlations are also compatible with the estimations.

In conclusion, the measurement of second order correlations in a BEC clearly confirms the expected reduction of $g^{(2)}$ to unity for a coherent particle source. Moreover, the data shows direct evidence of a heating effect that changes the characteristics of the observed correlation signal during the time of measurement. The slow increase in amplitude of the $g^{(2)}$ function is well explained by the theory of second order correlations for finite temperatures below T_C [80]. Therefore, the scanning electron microscopy technique not only enabled the first *in situ* measurement of temporal correlations within trapped atomic samples, it also demonstrates the feasibility of a minimally invasive *in vivo* observation and the characterization of quantum systems over time. Possible applications of this

method include the localized measurement of temperatures, which could prove particularly interesting for systems of reduced dimensionality.

Conclusion and Outlook

Scanning electron microscopy has proven to be a capable technique for the study of microscopic structures in ultracold quantum systems. Within the scope of this work, its performance in imaging atomic density distributions has been tested by examining Bose-Einstein condensates in harmonic trapping potentials and atomic ensembles in two dimensional optical lattices. Furthermore, the selective removal of atoms from the single sites of an optical lattice highlights the versatility of electron microscopy. In this, the presented methods for characterizing and optimizing the imaging system are of crucial importance and provide a foundation for future applications. Additionally, this thesis demonstrated the possibility of performing correlation measurements, which benefit from the high spatial resolution and the single atom sensitivity of the detection scheme. Scanning electron microscopy thereby enabled the first *in-situ* measurement of temporal correlations in thermal Bose gases and the partial coherence of Bose-Einstein condensates at finite temperatures. The potential for *in-vivo* observations, shown by the evaluation of heating effects within atomic samples, extends the scope for novel studies of correlation effects.

The imaging capabilities and the possibility of aiding in the preparation of yet unexplored quantum systems makes scanning electron microscopy an appealing instrument for future research. Highly resolved *in-situ* measurements of density distributions allow for the determination of a system's equation of state, which in turn enables the derivation of local thermodynamical quantities for characterizing quantum systems [88]. With the preparation of arbitrary mesoscopic ensembles in two-dimensional lattices, the transition from few-body systems to the thermodynamic limit could be studied. Also, the system could be used to observe the tunneling

7. CONCLUSION AND OUTLOOK

dynamics of single defects in optical lattices, which resemble Schottky defects in solids. Especially for the investigation of phenomena in low dimensional systems like the Tonks-Girardeau regime [89] scanning electron microscopy has proven its usefulness in subsequent work [90]. In the limit where particles are “fermionized” by strong repulsive interactions, their expected anti-bunching behavior could be shown by two-particle correlation measurements. Follow-up research might explore more complex dynamics that result from the quenching of one-dimensional Bose gases [91] and the thermalization processes in low dimensional systems [92]. Another yet unexplored field is the study of non-local pair correlations in 1D [93]. Since the electron beam can be moved to any position within small time steps, it is possible to measure spatial or spatio-temporal correlation functions without additional effort.

Supplementary Information

A.1 Poisson and Binomial Deletion

A Poisson source is measured with a detection efficiency of $0 < p \leq 1$. This process is also known as Binomial deletion of events. The probability of detecting k counts from a Poisson distribution with mean $\lambda = N$ is then given by:

$$\begin{aligned}
 D(k|N, p) &= \sum_{m=k}^{\infty} P_{\lambda=N}(m) B(k|m, p) = \sum_{m=k}^{\infty} \frac{N^m}{m!} e^{-N} \binom{m}{k} p^k (1-p)^{m-k} \\
 &= e^{-N} p^k \sum_{m=k}^{\infty} \frac{N^m}{m!} \frac{m!}{k!(m-k)!} (1-p)^{m-k} \\
 &= e^{-N} p^k N^k \frac{1}{k!} \sum_{m=k}^{\infty} \frac{N^{m-k}}{(m-k)!} (1-p)^{m-k} \quad \Big| \quad m' = m - k \\
 &= e^{-N} p^k N^k \frac{1}{k!} \sum_{m'=0}^{\infty} \frac{N^{m'}}{m'!} (1-p)^{m'} = e^{-N} p^k N^k \frac{1}{k!} e^{N(1-p)} \\
 &= \frac{(pN)^k}{k!} e^{-pN} = P_{\lambda=pN}(k).
 \end{aligned}$$

The probability distribution after Binomial deletion is identical to a Poisson distribution with its mean reduced by the detection probability $\lambda = pN$. Therefore, the detection efficiency does not affect the statistical behavior of a Poisson distribution. In particular, a coherent state is still seen as coherent state, regardless of the detection efficiency.

A.2 Generalized Wick Theorem

The full derivation of the *generalized Wick theorem for Boson operators* is found in [94]. It is a method of evaluating averages of Boson operators for thermal ensembles of atoms in equilibrium. For such systems, the density operator follows the Boltzmann distribution

$$\rho = \frac{e^{-\beta \hat{H}_0}}{\text{Tr} [e^{-\beta \hat{H}_0}]}, \quad (\text{A.1})$$

with the Hamiltonian $H_0 = \sum_j \hbar \omega_j a_j^\dagger a_j$ for a series of independent harmonic oscillators and $\beta = 1/k_B T$. The density matrix is strictly diagonal since there is no coherence between the various energy states for a statistical ensemble.

When evaluating the correlation functions in second quantization, thermal averages of creation and annihilation operators are to be solved. Such averages shall be defined as

$$\langle \psi_1 \psi_2 \cdots \psi_{2n} \rangle_0 \equiv \frac{\text{Tr} [\psi_1 \psi_2 \cdots \psi_{2n} e^{-\beta \hat{H}_0}]}{\text{Tr} [e^{-\beta \hat{H}_0}]}, \quad (\text{A.2})$$

with an even number operators ψ_i , which can be either creation or annihilation operators. In [94] it is shown that the expectation value of two operators may be expressed by their commutator

$$\langle \psi_1 \psi_2 \rangle_0 = \frac{[\psi_1, \psi_2]}{1 - e^{\pm \hbar \omega_i \beta}}, \quad (\text{A.3})$$

which means that the expectation value vanishes for two annihilation or two creation operators, as well as for operators of different energy levels. A contribution is only found for operators a_i and a_i^\dagger .

According to the generalized Wick theorem, any thermal average of the form (A.2) can be expressed as a series of pair expectation values

$$\begin{aligned} \langle \psi_1 \psi_2 \cdots \psi_{2n} \rangle_0 = & \langle \psi_1 \psi_2 \rangle_0 \langle \psi_3 \psi_4 \cdots \psi_{2n} \rangle_0 + \langle \psi_1 \psi_3 \rangle_0 \langle \psi_2 \psi_4 \cdots \psi_{2n} \rangle_0 + \cdots \\ & + \langle \psi_1 \psi_{2n} \rangle_0 \langle \psi_2 \psi_3 \cdots \psi_{2n-1} \rangle_0. \end{aligned} \quad (\text{A.4})$$

By repeated application, this reduces to sums of products of all pairs of thermal averages. The benefit in applying this theorem to thermal correlation functions is the ability to evaluate any higher order correlation function as a function of first order correlations, which must only be derived once.

A.3 Lattice Site Width Simulations

In Figure 4.6 the results from the analysis of simulated lattice images were shown in the context of typical experimental parameters. The lattice analysis method however does not depend on absolute length scales. By providing a generalized mapping of Fourier amplitudes and lattice site widths the simulation results can be adapted to other experimental parameters. This data is shown in Figure A.1. The simulated lattice site width ($\text{FWHM}_{\text{total}}$) is given as a fraction of the lattice spacing d . The width of the imaging point spread function (FWHM_{psf}) can therefore be determined by

$$\text{FWHM}_{\text{total}}^2 = \text{FWHM}_{\text{site}}^2 + \text{FWHM}_{\text{psf}}^2 \quad (\text{A.5})$$

if the real on-site width ($\text{FWHM}_{\text{site}}$) is known.

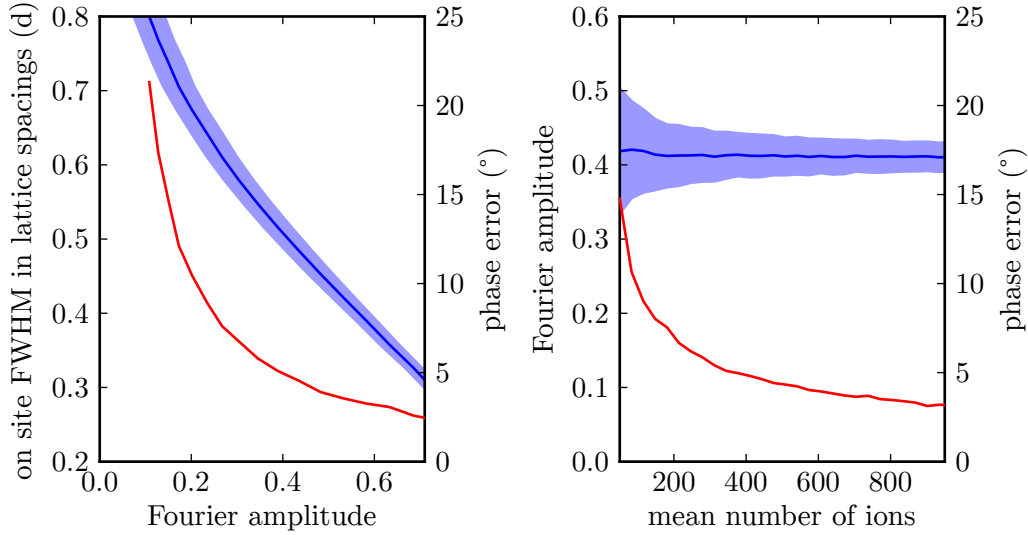


Figure A.1: Analysis of simulated lattice scans for various contrasts and ion numbers. In graph on the left, the Fourier amplitudes (blue) for various widths of the lattice sites are shown. The shape the sites is modeled with a Gaussian and their FWHM is given in units of the lattice spacing d . The error in determining the phases (red, right scale) is given in dependance of the Fourier amplitude. The standard error of the amplitude is depicted by the blue background.

A.4 Electron Column

In section 3.6 only a simplified illustration of the electron column was shown. This appendix provides the technical schematic of the electron column and labels the electron optics that were discussed in the experimental setup chapter.

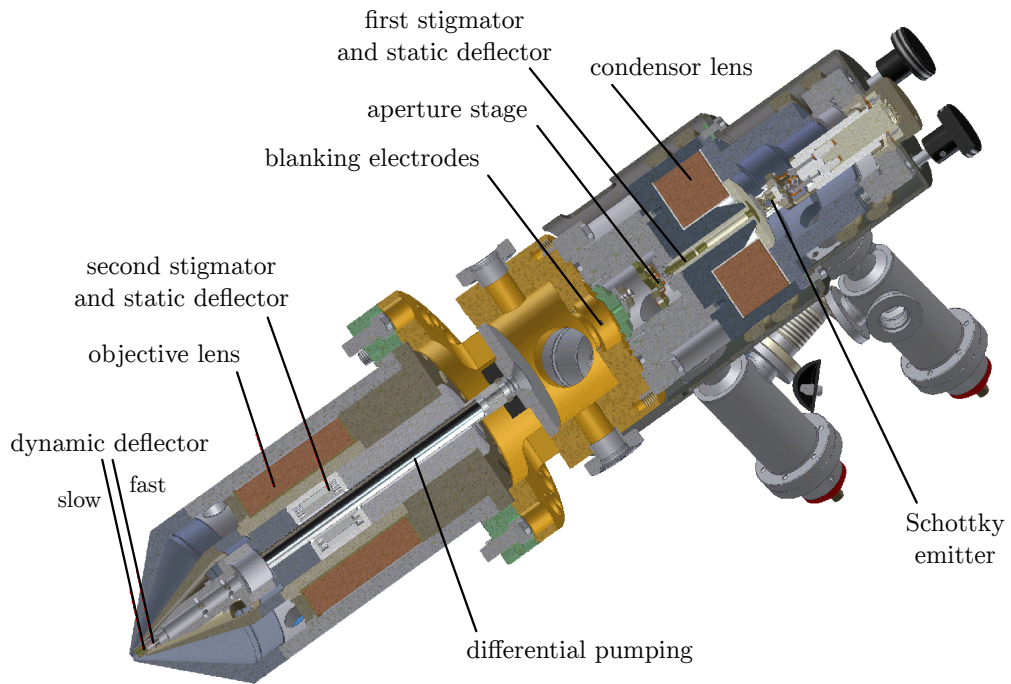


Figure A.2: Model of the scanning electron microscope. A thermal Schottky emitter is the source of the electron beam. The electron optics includes two stages where each stage consists of stigmators, deflectors and collimation lenses for shaping the electron beam. A variable aperture stage in between corrects for spherical aberrations and can be used to limit the beam current. A fast switch for enabling and disabling the electron beam is realized by the blanking electrodes. The bottommost deflector unit can be controlled externally and is responsible for scanning the electron beam.

A.5 Spatial Average Integrands

For estimating the spatial average of the $g^{(2)}$ and the $g^{(3)}$ spatio-temporal correlation functions we assume a Gaussian weighting distribution

$$p(\mathbf{r}) \propto e^{-w_x x^2 - w_y y^2 - w_z z^2}. \quad (\text{A.6})$$

Also the spatial component of the correlation function is Gaussian. The choice of the weighting function $p(\mathbf{r})$ allows for a separation of the integration axes in x , y and z . For each axis an integrand of Gaussian type is encountered that can be solved by successively completing a square and integrating the corresponding dimension. After a simplification of the final result, the fundamental integrals for evaluating the spatial average of $g^{(2)}(\Delta r, \tau)$ and $g^{(3)}(\Delta r_1, \Delta r_2, \Delta r_3, \tau_1, \tau_2, \tau_3)$ yield

$$\iint e^{-wx_1^2 - wx_2^2 - w_{12}(x_1 - x_2)^2} dx_1 dx_2 = \frac{\pi}{\sqrt{w^2 + 2ww_{12}}} \quad (\text{A.7})$$

and

$$\begin{aligned} & \iiint e^{-wx_1^2 - wx_2^2 - wx_3^2 - w_{12}(x_1 - x_2)^2 - w_{23}(x_2 - x_3)^2 - w_{13}(x_1 - x_3)^2} dx_1 dx_2 dx_3 \\ &= \frac{\pi^{3/2}}{\sqrt{w^3 + 2w^2(w_{12} + w_{23} + w_{13}) + 3w(w_{12}w_{13} + w_{12}w_{23} + w_{13}w_{23})}}. \end{aligned} \quad (\text{A.8})$$

List of Figures

2.1	Plane wave scattering approximation	15
2.2	Numerical BEC density profile	22
2.3	Semi-ideal model density profile	23
3.1	Overview of the experimental setup	26
3.2	Reference and cooling laser setup	28
3.3	CO ₂ laser trapping potential	31
3.4	Lattice density profiles	33
3.5	Atom distribution before and after light sheet transfer	35
3.6	Working principle of the electron microscope	36
3.7	Electron beam adjustment	38
3.8	Electron beam depth of focus	39
4.1	Ion time of flight spectrum	43
4.2	Correcting images for time of flight effects	44
4.3	BEC chisquare map	47
4.4	BEC linescans	48
4.5	Lattice image power spectrum	51
4.6	Stability in lattice simulation	53
4.7	Lattice correction examples	55
4.8	Examples of dissipative manipulation	57
4.9	Depletion of single sites	58
5.1	First order correlation for light sources	65
5.2	Simulation of spatially averaged correlation functions	72
6.1	Electron beam intersecting the atomic cloud	82
6.2	Experimental cycle for the lightsheet trap	83

6.3	Tabular arrangement of detection events	85
6.4	Evaluation of the $g^{(2)}$ matrix	86
6.5	Diagonals of the $g^{(2)}$ matrix	87
6.6	Temporal correlations in thermal gases	89
6.7	Third order correlation in a thermal gas	92
6.8	Uncorrelated control measurement	94
6.9	Total atom number fluctuation example	96
6.10	Counting artifact analysis, uncorrelated measurements	100
6.11	Counting artifact analysis, thermal correlation measurements	101
6.12	Oscillations in BEC measurement	105
6.13	Temporal correlations in a BEC	106
A.1	Generalized Lattice Simulation	113
A.2	Technical illustration of the scanning electron microscope	114

List of Tables

4.1	Comparison of the lattice visibility using Fourier amplitudes	55
6.1	Correction of the $g^{(2)}$ offset	97
6.2	Correction of the $g^{(2)}(0)$ correlation amplitudes	103

Bibliography

- [1] C. Davisson and L.H. Germer. The scattering of electrons by a single crystal of nickel. *Nature*, 119(2998):558--560, 1927.
- [2] RW Gurney and EU Condon. Quantum mechanics and radioactive disintegration. *Physical Review*, 33(2):127, 1929.
- [3] M.H. Anderson, J.R. Ensher, M.R. Matthews, C.E. Wieman, and E.A. Cornell. Observation of Bose-Einstein condensation in a dilute atomic vapor. *Science*, 269(5221):198--201, 1995.
- [4] C.C. Bradley, C.A. Sackett, J.J. Tollett, and R.G. Hulet. Evidence of Bose-Einstein condensation in an atomic gas with attractive interactions. *Physical Review Letters*, 75(9):1687--1690, 1995.
- [5] K.B. Davis, M.O. Mewes, M.R. Andrews, N.J. Van Druten, D.S. Durfee, D.M. Kurn, and W. Ketterle. Bose-Einstein condensation in a gas of sodium atoms. *Physical Review Letters*, 75(22):3969--3973, 1995.
- [6] EA Cornell and CE Wieman. Nobel lecture: Bose-einstein condensation in a dilute gas, the first 70 years and some recent experiments. *Reviews of Modern Physics*, 74(3):875, 2002.
- [7] W. Ketterle. Nobel lecture: When atoms behave as waves: Bose-Einstein condensation and the atom laser. *Reviews of Modern Physics*, 74(4):1131--1151, 2002.
- [8] A. Einstein. *Quantentheorie des einatomigen idealen Gases*. Akademie der Wissenschaften, 1924.

- [9] S. N. Bose. Plancks Gesetz und Lichtquantenhypothese. *Zeitung für Physik*, 26(3):178, 1924.
- [10] F. Dalfovo, S. Giorgini, L.P. Pitaevskii, and S. Stringari. Theory of Bose-Einstein condensation in trapped gases. *Reviews of Modern Physics*, 71(3):463, 1999.
- [11] W. Ketterle, DS Durfee, and DM Stamper-Kurn. Making, probing and understanding bose-einstein condensates. *arXiv preprint cond-mat/9904034*, 5, 1999.
- [12] W. Ketterle and M.W. Zwierlein. Making, probing and understanding ultracold fermi gases. *arXiv preprint arXiv:0801.2500*, 2008.
- [13] N.S. Ginsberg, S.R. Garner, and L.V. Hau. Coherent control of optical information with matter wave dynamics. *Nature*, 445(7128):623-626, 2007.
- [14] I. Bloch, J. Dalibard, and W. Zwerger. Many-body physics with ultracold gases. *Reviews of Modern Physics*, 80(3):885, 2008.
- [15] G.K. Brennen, C.M. Caves, P.S. Jessen, and I.H. Deutsch. Quantum logic gates in optical lattices. *Physical Review Letters*, 82(5):1060--1063, 1999.
- [16] R. Raussendorf and H.J. Briegel. A one-way quantum computer. *Physical Review Letters*, 86(22):5188--5191, 2001.
- [17] M. Schellekens, R. Hoppeler, A. Perrin, J.V. Gomes, D. Boiron, A. Aspect, and C.I. Westbrook. Hanbury Brown Twiss effect for ultracold quantum gases. *Science*, 310(5748):648--651, 2005.
- [18] T. Jelte, J.M. McNamara, W. Hogervorst, W. Vassen, V. Krachmalnicoff, M. Schellekens, A. Perrin, H. Chang, D. Boiron, A. Aspect, and C. I. Westbrook. Comparison of the Hanbury Brown-Twiss effect for bosons and fermions. *Nature*, 445(7126):402--405, 2007.
- [19] Simon Fölling, Fabrice Gerbier, Artur Widera, Olaf Mandel, Tatjana Gericke, and Immanuel Bloch. Spatial quantum noise interferometry in expanding ultracold atom clouds. *Nature*, 434(7032):481--484, mar 2005.
- [20] T. Gericke, C. Utfeld, N. Hommerstad, and H. Ott. A scanning electron microscope for ultracold atoms. *Laser Physics Letters*, 3(8):415-419, 2006.

-
- [21] P. Würtz, T. Gericke, T. Langen, A. Koglbauer, and H. Ott. Probing bose-einstein condensates by electron impact ionization. In *Journal of Physics: Conference Series*, volume 141, page 012020. IOP Publishing, 2008.
- [22] T. Gericke, P. Würtz, D. Reitz, T. Langen, and H. Ott. High-resolution scanning electron microscopy of an ultracold quantum gas. *Nature Physics*, 4(12):949--953, 2008.
- [23] E. Fermi. Zur Quantelung des idealen einatomigen Gases. *Zeitschrift für Physik A Hadrons and Nuclei*, 36:902--912, 1926. 10.1007/BF01400221.
- [24] J.J. Sakurai and J. Napolitano. *Modern Quantum Mechanics*. Addison-Wesley, 2010.
- [25] F. Scheck. *Theoretische Physik 2, Nichtrelativistische Quantentheorie*. Springer, 2000.
- [26] C. Cohen-Tannoudji, B. Diu, and F. Laloë. *Quantum Mechanics*, volume 2. John Wiley & Sons, 1991.
- [27] A. Marte. *Feshbach-Resonanzen bei Stößen ultrakalter Rubidiumatome*. PhD thesis, Technische Universität München, 2003.
- [28] N. Bogoliubov. On the theory of superfluidity. *Journal of Physics*, 11, 23, 1947.
- [29] E. P. Gross. Structure of a quantized vortex in boson systems. *Il Nuovo Cimento*, 20(3):454--457, 1961.
- [30] L. P. Pitaevskii. Vortex lines in an imperfect Bose gas. *Soviet Physics JETP*, 13(2):451--454, 1961.
- [31] L. Lehtovaara, J. Toivanen, and J. Eloranta. Solution of time-independent Schrödinger equation by the imaginary time propagation method. *Journal of Computational Physics*, 221(1):148--157, 2007.
- [32] C.M. Dion and E. Cancès. Ground state of the time-independent Gross-Pitaevskii equation. *Computer physics communications*, 177(10):787--798, 2007.
- [33] P. Muruganandam and S.K. Adhikari. Fortran programs for the time-dependent Gross-Pitaevskii equation in a fully anisotropic trap. *Computer Physics Communications*, 180(10):1888--1912, 2009.

BIBLIOGRAPHY

- [34] A. Minguzzi, S. Conti, and M.P. Tosi. The internal energy and condensate fraction of a trapped interacting Bose gas. *Journal of Physics: Condensed Matter*, 9:L33, 1997.
- [35] D.A.W. Hutchinson, E. Zaremba, and A. Griffin. Finite temperature excitations of a trapped Bose gas. *Physical Review Letters*, 78(10):1842--1845, 1997.
- [36] C. Utfeld. Aufbau einer Hochleistungsquelle für ultrakalte Atome. Diplomarbeit, Johannes Gutenberg-Universität Mainz, 2006.
- [37] N. Hommerstad. Eine CO₂-Dipolfalle für ultrakalte Quantengase. Diplomarbeit, Johannes Gutenberg-Universität Mainz, 2007.
- [38] T. Gericke. *A scanning electron microscope for ultracold quantum gases*. PhD thesis, Johannes Gutenberg-Universität Mainz, 2010.
- [39] K. Dieckmann, RJC Spreeuw, M. Weidemuller, and JTM Walraven. The two-dimensional magneto-optical trap as a source of slow atoms. *Physical Review A*, 58:3891, 1998.
- [40] D.A. Steck. Rubidium 87 d line data. *Los Alamos National Laboratory*, 2001.
- [41] H.J. Metcalf and P. Van der Straten. *Laser cooling and trapping*. Springer Verlag, 1999.
- [42] EL Raab, M. Prentiss, A. Cable, S. Chu, and D.E. Pritchard. Trapping of neutral sodium atoms with radiation pressure. *Physical Review Letters*, 59(23):2631--2634, 1987.
- [43] C.S. Adams, H.J. Lee, N. Davidson, M. Kasevich, and S. Chu. Evaporative cooling in a crossed dipole trap. *Physical review letters*, 74(18):3577--3580, 1995.
- [44] H.F. Hess. Evaporative cooling of magnetically trapped and compressed spin-polarized hydrogen. *Physical Review B*, 34(5), 1986.
- [45] N. Masuhara, J.M. Doyle, J.C. Sandberg, D. Kleppner, T.J. Greytak, H.F. Hess, and G.P. Kochanski. Evaporative cooling of spin-polarized atomic hydrogen. *Physical Review Letters*, 61(8):935--938, 1988.
- [46] MD Barrett, JA Sauer, and MS Chapman. All-optical formation of an atomic Bose-Einstein condensate. *Physical Review Letters*, 87(1):10404, 2001.

-
- [47] G. Cennini, G. Ritt, C. Geckeler, and M. Weitz. Bose-Einstein condensation in a CO₂-laser optical dipole trap. *Applied Physics B*, 77(8):773--779, 2003.
 - [48] G. Cennini, G. Ritt, C. Geckeler, and M. Weitz. All-optical realization of an atom laser. *Physical Review Letters*, 91(24):240408, 2003.
 - [49] R. Grimm, M. Weidemüller, and Y.B. Ovchinnikov. Optical dipole traps for neutral atoms. *Advances in atomic, molecular, and optical physics*, 42:95--170, 2000.
 - [50] DC McKay and B. DeMarco. Cooling in strongly correlated optical lattices: prospects and challenges. *Reports on Progress in Physics*, 74:054401, 2011.
 - [51] B. Frohlich, T. Lahaye, B. Kaltenhauser, H. Kubler, S. Muller, T. Koch, M. Fattori, and T. Pfau. Two-frequency acousto-optic modulator driver to improve the beam pointing stability during intensity ramps. *Review of Scientific Instruments*, 78(4):043101--043101, 2007.
 - [52] I. Bloch. Ultracold quantum gases in optical lattices. *Nature Physics*, 1(1):23--30, 2005.
 - [53] D. Reitz. Ortsaufgelöster Nachweis ultraklater Atome in optischen Gittern. Diplomarbeit, Johannes Gutenberg-Universität Mainz, 2007.
 - [54] T. Langen. Addressing of ultracold atoms in optical lattices. Diplomarbeit, Johannes Gutenberg-Universität Mainz, 2008.
 - [55] M.P.A. Fisher, P.B. Weichman, G. Grinstein, and D.S. Fisher. Boson localization and the superfluid-insulator transition. *Physical Review B*, 40(1):546, 1989.
 - [56] D. Jaksch, C. Bruder, J.I. Cirac, C.W. Gardiner, and P. Zoller. Cold bosonic atoms in optical lattices. *Physical Review Letters*, 81(15):3108--3111, 1998.
 - [57] W. Zwerger. Mott--hubbard transition of cold atoms in optical lattices. *Journal of Optics B: Quantum and Semiclassical Optics*, 5(2):S9, 2003.
 - [58] M. Greiner, O. Mandel, T. Esslinger, T.W. Hänsch, and I. Bloch. Quantum phase transition from a superfluid to a Mott insulator in a gas of ultracold atoms. *Nature*, 415(6867):39--44, 2002.

- [59] Arne Ewerbeck. Messung zeitlich aufgelöster Paarkorrelationen in ultrakalten Quantengasen. Diplomarbeit, Technische Universität Kaiserslautern, 2011.
- [60] P. Würtz. Detection of ultracold atoms using electron-impact-ionization. Diplomarbeit, Johannes Gutenberg-Universität Mainz, 2007.
- [61] P. Würtz, T. Gericke, A. Vogler, and H. Ott. Ultracold atoms as a target: absolute scattering cross-section measurements. *New Journal of Physics*, 12:065033, 2010.
- [62] Jon Orloff. *Handbook of charged particle optics*. CRC Press, 1997.
- [63] N. Navon, S. Piatecki, K. Günter, B. Rem, T.C. Nguyen, F. Chevy, W. Krauth, and C. Salomon. Dynamics and thermodynamics of the low-temperature strongly interacting Bose gas. *Physical Review Letters*, 107(13):135301, 2011.
- [64] R.C. González, R.E. Woods, and S.L. Eddins. *Digital Image Processing Using Matlab*. Pearson Prentice Hall, 2004.
- [65] BP Anderson and M.A. Kasevich. Macroscopic quantum interference from atomic tunnel arrays. *Science*, 282(5394):1686--1689, 1998.
- [66] M. Greiner, I. Bloch, O. Mandel, TW Hänsch, and T. Esslinger. Bose-Einstein condensates in 1d-and 2d optical lattices. *Applied Physics B: Lasers and Optics*, 73(8):769--772, 2001.
- [67] Thilo Stöferle, Henning Moritz, Christian Schori, Michael Köhl, and Tilman Esslinger. Transition from a strongly interacting 1d superfluid to a Mott insulator. *Physical Review Letters*, 92:130403, Mar 2004.
- [68] T. Kinoshita, T. Wenger, and D.S. Weiss. Observation of a one-dimensional Tonks-Girardeau gas. *Science*, 305(5687):1125--1128, 2004.
- [69] K.D. Nelson, X. Li, and D.S. Weiss. Imaging single atoms in a three-dimensional array. *Nature Physics*, 3(8):556--560, 2007.
- [70] P. Würtz, T. Langen, T. Gericke, A. Koglbauer, and H. Ott. Experimental demonstration of single-site addressability in a two-dimensional optical lattice. *Physical Review Letters*, 103(8):80404, 2009.

- [71] M. Tico and M. Vehvilainen. Robust method of digital image stabilization. In *Communications, Control and Signal Processing, 2008. ISCCSP 2008. 3rd International Symposium on*, pages 316–321. IEEE, 2008.
- [72] Neil W. Ashcroft and David N. Mermin. *Solid State Physics*. Thomson Learning EMEA, 1 edition, January 1976.
- [73] M. D. Lukin, M. Fleischhauer, R. Cote, L. M. Duan, D. Jaksch, J. I. Cirac, and P. Zoller. Dipole blockade and quantum information processing in mesoscopic atomic ensembles. *Physical Review Letters*, 87:037901, Jun 2001.
- [74] Jean-Sébastien Bernier, Corinna Kollath, Antoine Georges, Lorenzo De Leo, Fabrice Gerbier, Christophe Salomon, and Michael Köhl. Cooling fermionic atoms in optical lattices by shaping the confinement. *Physical Review A*, 79:061601, Jun 2009.
- [75] R. Hanbury Brown and R.Q. Twiss. A new type of interferometer for use in radio astronomy. *Philosophical Magazine Series 7*, 45(366):663–682, 1954.
- [76] R.H. Brown and RQ Twiss. Correlation between photons in two coherent beams of light. *Nature*, 177(4497):27–29, 1956.
- [77] R. Hanbury Brown and R.Q. Twiss. A test of a new type of stellar interferometer on Sirius. *Nature*, 178(4541):1046, 1956.
- [78] Vera Guarrera, Peter Würtz, Arne Ewerbeck, Andreas Vogler, Giovanni Barontini, and Herwig Ott. Observation of local temporal correlations in trapped quantum gases. *Physical Review Letters*, 107:160403, Oct 2011.
- [79] R. Loudon. *The quantum theory of light*. Oxford science publications. Oxford University Press, 2000.
- [80] M. Naraschewski and RJ Glauber. Spatial coherence and density correlations of trapped Bose gases. *Physical Review A*, 59(6):4595, 1999.
- [81] M.C. Teich and B.E.A. Saleh. Observation of sub-Poisson Franck-Hertz light at 253.7 nm. *JOSA B*, 2(2):275–282, 1985.

- [82] M.C. Teich and B.E.A. Saleh. Effects of random deletion and additive noise on bunched and antibunched photon-counting statistics. *Optics Letters*, 7(8):365--367, 1982.
- [83] K.M. Van Vliet and L.M. Rucker. Noise associated with reduction, multiplication and branching processes. *Physica A: Statistical and Theoretical Physics*, 95(1):117--140, 1979.
- [84] B.E.A. Saleh and M.C. Teich. Multiplied-poisson noise in pulse, particle, and photon detection. *Proceedings of the IEEE*, 70(3):229--245, 1982.
- [85] P. Würtz, T. Gericke, A. Vogler, F. Etzold, and H. Ott. Image formation in scanning electron microscopy of ultracold atoms. *Applied Physics B: Lasers and Optics*, 98(4):641--645, 2010.
- [86] R. Heijmans. When does the expectation of a ratio equal the ratio of expectations? *Statistical Papers*, 40(1):107--115, 1999.
- [87] Anton Öttl, Stephan Ritter, Michael Köhl, and Tilman Esslinger. Correlations and counting statistics of an atom laser. *Physical Review Letters*, 95:090404, Aug 2005.
- [88] S. Nascimbène, N. Navon, F. Chevy, and C. Salomon. The equation of state of ultracold bose and fermi gases: a few examples. *New Journal of Physics*, 12(10):103026, 2010.
- [89] M. Girardeau. Relationship between systems of impenetrable bosons and fermions in one dimension. *Journal of Mathematical Physics*, 1:516, 1960.
- [90] Vera Guarrera, Dominik Muth, Ralf Labouvie, Andreas Vogler, Giovanni Barontini, Michael Fleischhauer, and Herwig Ott. Spatiotemporal fermionization of strongly interacting one-dimensional bosons. *Physical Review A*, 86:021601, Aug 2012.
- [91] J.S. Bernier, G. Roux, and C. Kollath. Slow quench dynamics of a one-dimensional bose gas confined to an optical lattice. *Physical Review Letters*, 106(20):200601, 2011.
- [92] M. Rigol. Breakdown of thermalization in finite one-dimensional systems. *Physical review letters*, 103(10):100403, 2009.

- [93] AG Sykes, DM Gangardt, MJ Davis, K. Viering, MG Raizen, and KV Kheruntsyan. Spatial nonlocal pair correlations in a repulsive 1d bose gas. *Physical review letters*, 100(16):160406, 2008.
- [94] W.H. Louisell. *Quantum statistical properties of radiation*. Wiley series in pure and applied optics. Wiley, 1973.

Curriculum Vitae

Persönliche Daten

Name	Peter Christian Würtz
Geboren	01.01.1983, Worms
E-Mail	pwuertz@gmail.com

Studium und Diplom

2002	Physikstudium, Johannes Gutenberg-Universität Mainz
2004	Vordiplom, Note: sehr gut
2007	Abschluss: Diplom-Physiker, Note: sehr gut Diplomarbeit mit dem Titel „ <i>Detection of ultracold atoms using electron impact-ionization</i> “ in der Arbeitsgruppe von Prof. Dr. Herwig Ott an der Johannes Gutenberg-Universität Mainz

Promotion

2007	Promotionsstudium zum Thema „ <i>Imaging the microscopic structure of ultracold quantum gases</i> “ in der Arbeitsgruppe von Prof. Dr. Herwig Ott, Johannes Gutenberg-Universität Mainz
2010	Umzug der Arbeitsgruppe und Fortsetzung der Promotion an der Technischen Universität Kaiserslautern

21. Dezember 2012